Atomic scale structural modifications in irradiated nuclear fuels

Cyprian Mieszczynski

UNIVERSITÉ PARIS SUD

Comprendre le monde, construire l'avenir®

PAUL SCHERRER INSTITUT

UNIVERSITE PARIS-SUD

ÉCOLE DOCTORALE : MIPEGE 534
Laboratory for Nuclear Materials

***DISCIPLINE** Chimie*

THÈSE DE DOCTORAT
THÈSE DE DOCTORAT SUR TRAVAUX

soutenue le 11/04/2014

par

Cyprian MIESZCZYNSKI

Atomic scale structural modifications in irradiated nuclear fuels

Directeur de thèse :	Eric SIMONI	Professeur, Université Paris-Sud 11
Tuteur de thèse :	Goutam KURI	Chercheur, Paul Scherrer Institut
Composition du jury :		
Président du jury :	Frédérico GARRIDO	Professeur, Université Paris-Sud 11
Rapporteurs :	Nicolas DACHEUX	Professeur, Université Montpellier 2
	Jean-Louis HAZEMANN	Directeur de recherche, CNRS
Examinateurs :	Claude DEGUELDRE	Chercheur, Paul Scherrer Institut
	Philippe MARTIN	Chercheur, CEA
Membres invités :	Christine DELAFOY	Ingénieur, AREVA NP

Thesis contents

List of abbreviations

BWR	Boiling Water Reactor
CCD	Charge-Coupled Device
EPMA	Electron Probe Micro Analysis/-er
EXAFS	Extended X-ray Absorption Fine Structure
FT	Fourier Transform
KKB	Kernkraftwerk Beznau
KKG	Kernkraftwerk Gösgen
KKL	Kernkraftwerk Leibstadt
LHGR	Linear Heat Generation Rate
LNM	Laboratory for Nuclear Materials
LWR	Light Water Reactor
NEXAFS	Near Edge X-ray Absorption Fine Structure
NPP	Nuclear Power Plant
PSI	Paul Scherrer Institut
PWR	Pressurized Water Reactor
RT	Room Temperature
SEM	Scanning Electron Microscope
SLS	Swiss Light Source
XAFS	X-ray Absorption Fine Structure
XANES	X-ray Absorption Near Edge Spectroscopy
XAS	X-ray Absorption Spectroscopy
XRD	X-ray Diffraction
XRF	X-ray Fluorescence

List of figures

List of tables

For my family

Acknowledgements

This thesis contains both unpublished results and materials from published manuscripts of the author. This research was carried out in the Laboratory for Nuclear Materials at the Paul Scherrer Institut (PSI), in the framework of collaboration among PSI, Université Paris-Sud 11 and AREVA NP, France. I sincerely thank all my collaborators for giving me the opportunity to work with them.

First and the foremost acknowledgements go to Prof. Eric Simoni (Université Paris-Sud 11, France), the director of my PhD thesis and to Dr. Goutam Kuri (Paul Scherrer Institute, Switzerland), the supervisor of my thesis for giving me the opportunity to carry out this research and for advices and guidance throughout this doctoral work.

I am very grateful also to Pr. Doc. Dr. Claude Degueldre and Dr. Johannes Bertsch at the Paul Scherrer Institute as well as Christine Delafoy (AREVA NP, France) for all their input, help and discussions. I need to thank them for the time they have always found for me and for this project to optimize efforts and results.

During my doctoral work I had the possibility to interact with many people at PSI. I would like to thank: Dr. Annick Froideval, Dr. Sousan Abolhassani, Dr. Manuel Pouchon, Matthias Martin, Robert Zubler, and Andrej Bullemer. It was a pleasure for me to always receive a positive feedback from all of them.

I would like to show my gratitude also to Dr. Daniel Grolimund and Dr. Camelia Borca, the beamline scientists for precious help during all my SLS experimental campaigns.

I have many friends and colleges whom I would like to thank for making these three years at PSI more enjoyable (i.e. Andrey, Cedric, Christian, Goran, Hygreeva, Henar, Jakub, Jan, Loic, Lyubomira, Marc, Maria, Melanie, Nazar, Sebastian, Slava, Wenwang and many others).

Finally, I would like to express my deepest gratitude and affection to my dear Kasia and all my family for supporting me during the entire PhD period.

Special thanks go to AREVA and swissnuclear for supporting this doctoral research and providing valuable suggestions during our meetings.

Aims and scope

Both experimental tests and computational modeling are required to understand the structural evolution of irradiated nuclear fuels at the atomic scale. The main goal of this thesis work is the experimental investigation of irradiation-induced atomic scale micro-structural changes occurring in relatively larger grain chromia-doped UO_2 fuels. The role of chromium as dopant is analyzed and the fuel behavior is compared to that of standard UO_2.

Another goal is to determine the impact of a few selective fission products (both, soluble and insoluble gas atoms) on the structural evolution of the irradiated fuel matrix.

A part of the thesis work concerns irradiated $(U,Pu)O_2$ MOX fuels to understand the atomic scale structural changes at very high burn-up.

Both neutron irradiation and fission products influence the crystallographic lattice structure of UO_2. In order to predict the fuel behavior at a macroscopic level, it is important to understand structural variations and the behavior of fission products at microscopic and atomic levels. Modern synchrotron-radiation based microprobes, X-ray absorption spectroscopy (μXAS) and X-ray diffraction (μXRD) techniques, as applied in this thesis, have the ability to experimentally reveal the atom specific environment and lattice structures.

Chapter 1: General Introduction

1.1 Introduction

Low enriched (with fissile ^{235}U) nuclear fuel that is used in commercial light water reactors is made of uranium dioxide, UO_2 [1,2]. Fission of ^{235}U generates light and heavy fission fragments which disturb the cation-cation and cation-anion network in the fuel matrix. The behavior of all safety relevant fission products is of outmost importance in any nuclear reactor operation and of fuel rod performance. Nevertheless, with a long history and well-established manufacturing base, uranium dioxide fuel pellets are the standard fuel for most of the light water reactors in-service worldwide. In the Figure 1.1 the schematic view of a fuel a rod and rod assembly for AREVA PWR fuel rods is provided.

The performance of standard UO_2 is, however, mostly limited today by the phenomenon of pellet-cladding interaction (PCI), fuel swelling and fission gas release; the impact of those phenomena increases with increasing burn-up (whereas the PCI problematic is most prominent at mid burn-up). Therefore, the actual tendency is to manufacture advanced UO_2 fuels capable to resist the listed effects. A way to amend the fuel behavior is to diminish the fuel rods internal pressure by an adequate large grain UO_2 fuel pellet structure. In the large grain size UO_2 pellets, fission gas (e.g., Kr and Xe) release rate decreases. It has been shown by the studies carried out in fuel research [3,4] that one of the possible options to increase pellets grain size without increasing sintering temperature and time is the addition of small quantities of additives. By the addition of certain dopants in the UO_2 powder (e.g., TiO_2, Nb_2O_5, Cr_2O_3, V_2O_5 etc.) the grain size, the porosity and the mean free diffusion path are increased, whereas the grain boundary area is reduced. The addition of a dopant oxide powder during sintering is the economically most viable one. One of the most frequently used and currently investigated dopants in nuclear R&D is Cr_2O_3 for the grain enlargement of uranium dioxide fuels. In particular, doping of UO_2 with Cr_2O_3 has been the topic of numerous studies [5,6] in the last decade that has yielded products today available on the fuel market.

In the operating nuclear reactors, there is also formation of heavier isotopes, such as plutonium due to neutron capture, primarily by ^{238}U. ^{239}Pu and ^{241}Pu are fissile, and indeed, fissioning of plutonium as a constituent in mixed uranium-plutonium dioxide (MOX) fuels is an option to reduce excess plutonium. MOX fuels contain a mixture of approximately 95-85 percent uranium oxide and remaining 5-15 percent plutonium oxide. The present thesis work presents some exemplary results on the atomic scale structural modifications in three different type fuel materials, namely standard UO_2, Cr_2O_3-doped UO_2 and a MOX fuel, aiming to have a better knowledge of the local structure of these systems.

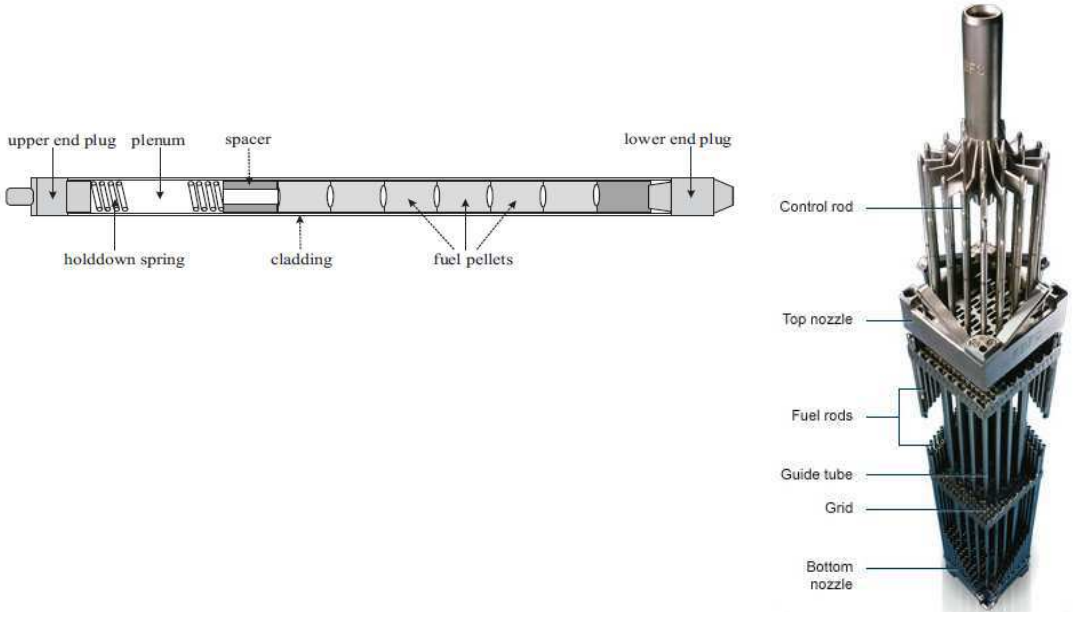

Figure 1.1: Schematic view of fuel rod and fuel rod assembly for Areva PWR fuel rods [1,7].

While significant experimental work has been done in the past in studying operation induced changes in the UO_2 or MOX fuel matrix using EPMA, SEM, TEM etc., the application of synchrotron based micro-beam XRF, XRD and XAS to investigate irradiated oxide fuel has been very limited. These synchrotron radiation based techniques have the ability to probe local very locally lattice properties and the environment of specific atoms including speciation and electronic structure. Since highly active irradiated materials represent regulatory based radiation protection issues for research at synchrotron beam lines, for the first time, methods have been developed in specimen

preparation as well as experimental measurements overcoming those problems, especially for spent fuels.

This thesis work reports in depth analyses of measured μ-XRD and μ-XAS data from standard UO_2, chromia (Cr_2O_3) doped UO_2 and MOX fuels, and interpretation of the results considering the role of chromium as a dopant as well as several fission product elements. The lattice parameters of UO_2 in fresh and irradiated samples and elastic strain energy densities in the irradiated UO_2 samples have been measured and quantified. The μ-XRD patterns have further allowed the evaluation of the crystalline domain size and sub-grain formation at different locations of the irradiated fuel pellets. Attempts have been made to determine lattice parameter and next neighbor atomic environment in chromia-precipitates found in fresh chromia-doped fuel pellets. The local structure around Cr in as-fabricated chromia-doped UO_2 matrix and the influence of irradiation (for the given burn-up range) on the state of chromium in irradiated fuel matrix have been addressed. Finally, for a comparative understanding of fission gases behavior and irradiation induced re-solution phenomenon in standard and chromia-doped UO_2, the last part of the present work tries to clarify the fission gas Kr atomic environment in these irradiated fuels. The work performed on Kr, by micro-beam XAS, comprises the determination of Kr next neighbor distances, an estimation of gas atom densities in the aggregates, and apparent (rather theoretical) internal pressures in the gas bubbles.

1.2 Structure of the thesis

Chapter one provides a general introduction on the investigations performed during the PhD project. In the second part of the first chapter the state of research on nuclear fuel materials, emphasizing chromia-doped fuels, is described based on the literature survey.

The second chapter provides a detailed description of the used methodology. This experimental section contains a description of the investigated materials, sample preparation methods used, experimental set-up, and as a subsection the theoretical approach to the analytical methods applied.

The third chapter provides measurements results. It comprises the outcome of the micro-X-rays Laue diffraction measurements. The focus is on the UO_2 matrix material. The changes in the matrix of all the investigated types of fuel occurring after irradiation are highlighted. A sensitivity analysis for the revealed lattice parameters of standard (non-doped), Cr_2O_3-doped UO_2 and for MOX fuels are presented and compared. The chapter also provides analyses regarding strain energy density and sub-grain formation in irradiated fuel.

The fourth chapter focuses on the analysis of the dopant element chromium in chromia-doped fuels. The microstructure of remnant chromia precipitates, occasionally found in the chromia-doped fresh fuel pellet, is analyzed employing the micro-XRD technique. The oxidation state and local atomic environment of chromium atoms dissolved in the UO_2 matrix are studied using micro-beam X-ray absorption spectroscopy. The analyses were made for both, fresh and irradiated fuels.

The fifth chapter reports the investigations of one of the fission gases, krypton. This part of the work comprises the successful XAS measurements of this fission gas atom in the used fuel, the determination of the neighbour atomic environment of Kr and an estimation of the apparent gas-bubble-pressure.

The sixth chapter comprises the conclusions and an outlook with suggestions for future studies.

1.3 Literature review

At room temperature uranium dioxide has a cubic fluorite structure (space group $Fm\bar{3}m$, no. 225). The unit-cell is shown in Figure 1.2. In the fluorite structure uranium atoms form a face-centred cubic lattice with oxygen atoms occupying the tetrahedral sites. From the figure it is clear that there exists unoccupied space that may be available to accommodate dissolvable fission products (FPs). This, in turn can help in part to reduce the problematic of fuel swelling.

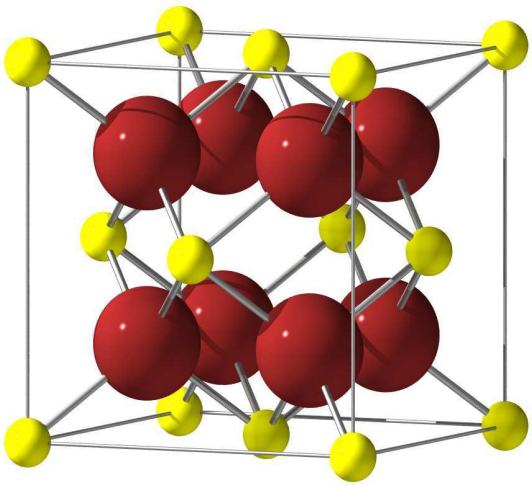

Figure 1.2: Uranium dioxide crystal unit cell. Yellow and red spheres stand for uranium and oxygen atoms, respectively. (Courtesy: PhD thesis, C.R. Stanek, Imperial College of Science, August 2003).

The temperature distribution and the concomitant intense radiation field during burn-up affect and alter the crystallographic UO_2 fuel matrix. Although fresh fuel is prepared as closely as possible to stoichiometric UO_2, during in-reactor irradiation the fuel pellets are oxidized. The oxidation of UO_2, i.e. the increase in the oxygen/metal (O/M) ratio accelerates not only FPs release due to their enhanced diffusivity, but also fuel operating temperature due to the decreased thermal conductivity. The higher fuel temperature leads to a larger thermal expansion and fission gas bubble swelling in the pellet, potentially causing more pellet-cladding interaction. Although there are many investigations on UO_2 oxidation and fission products distribution in used fuel [8,9] from post irradiation examination (PIE), quantitative information on the stoichiometric composition and

crystallographic structure along the fuel pellet diameter and rod axial directions is very limited. The understanding of UO_2 lattice structures in irradiated fuels is also incomplete. It is common sense that the irradiated UO_2 is mostly affected by the build-up of solid fission products (both in solution and as precipitates), formation and diffusion of fission gas atoms and formation of bubbles, deviation from perfect stoichiometry of the base UO_2 material, and radiation damage. With increasing burn-up, the microstructural changes in the fuel become more and more pronounced.

FG diffusion. The investigations of the diffusion of fission products in UO_2 began practically with the use of uranium dioxide as a fuel in commercial nuclear power plants [10,11]. The first studies were focused mainly on heavy elements and their behaviour, only later the importance of fission gas diffusion was noted [12,13].

First models describing diffusion of fission gases under irradiation appeared in the late Fifties. The first known relation for fission gases diffusion was proposed by A.H Booth. In 1957 he suggested formula (1.1) that quantified fractional release of fission gases under irradiation conditions. This model describes the diffusion of fission-product atoms in a spherical fuel grain [14,15].

$$F = 1 - \frac{6a^2}{\pi^4 Dt} \sum_{n=1}^{\infty} \frac{1}{n^4} \left[1 - \exp\left(\frac{-n^2 \pi^2 Dt}{a^2} \right) \right] \tag{1.1}$$

where:
D- diffusion coefficient;
t- time;
a- radius of hypothetical spherical volume;

The Booth diffusion model is a simplification of the physical processes involved in the release of fission products, and as such, it cannot correctly calculate the release for all fuel scenarios.

The release of the fission products can be referred also to the release-to-birth ratio [16]. This ratio can be calculated using equation (1.2). This modified model includes additional parameters as e.g. gas-resolution. However, this model works only for equilibrium conditions.

$$\frac{R}{B} = 3\left[\frac{1}{\sqrt{\mu}}\coth\left(\sqrt{\mu}\right) - \frac{1}{\sqrt{\mu}}\right] \quad (1.2)$$

where:

$\mu = \lambda a^2 / D$

λ- decay constant;
a- sphere radius;
D- diffusion coefficient;
R- number of atoms released per unit time (accounting for decay and temperature at a point in time);
B- number of atoms produced per unit time at the same point in time;

The release-to-birth ratio has an inverse relation with respect to the grain sphere radius. It means that increasing the grain size would reduce the fraction of fission gases released from the fuel matrix in a given volume of UO_2. Because of this fact, the fuel grain enlargement investigations were launched in research worldwide and it was considered as an important issue for fuel improvement.

It needs to be added that the model represented by equation 1.2 assumes a constant diffusion coefficient. However, the effect of stoichiometry and the effect of fission gas sites occupancy on the diffusion coefficient were studied by several authors [17,18].

Turnbull *et al.* [19] proposed the following relation for the diffusion coefficient to include irradiation effect:

$$D = D_1 + D_2 + D_3 \quad (1.3)$$

Where:

D_1 -thermally activated diffusion, D_2 -effect of the uranium vacancies, D_3 -radiation enhanced diffusion.

As can be seen the diffusion coefficient is driven by three constituents. However, some effects from the grain size and grain microstructure affecting the coefficient can also be observed. In respect to that an additional part could be added to the diffusion coefficient.

Burn-up. Thermal energy that is produced during reactor operation is represented by the fuel burn-up. The burn-up is defined as amount of thermal energy produced per unit of heavy metal in the fuel. The typically used unit is GW d t^{-1} or MW d kg^{-1} (1 MW d kg^{-1} is equivalent to 86.4 x 10^9 J kg^{-1} in SI units). The burn-up can be defined also as percentage of fissions per heavy metal atom present in the fuel initially (%FIMA, fissions per initial

metal atom). There is no official definition for low, medium and high burn-up and the differentiation is arbitrary. However, in current nuclear R&D usually it is assumed that the low burn-up is below 30 MW d kg^{-1}, medium from 30 MWdkg^{-1} to 60 MW d kg^{-1} and high above 60 MW d kg^{-1}. Sometimes in the literature it is possible to find also the concept of ultra-high burn-up above 90 MW d kg^{-1}.

High burn-up structure (HBS). The fuel defects become more prominent with increasing burn-up leading to a restructuring of the fuel. As the formation of the HBS starts at the outer part of the pellet, this type of structure is also called rim structure. Main reasons for the fuel restructuring are: the high amount of fissions, the irradiation damage by neutrons and recoil fission products and the thermo-mechanical conditions in the fuel pellet. The following effects accompany the formation of high burn-up or rim structure.

- Fuel grain polygonization: this effect consists in change of the initial grain size. The original grains are subdivided into new small grains with a diameter of ~0.1-0.5 μm. The new sub-grains exhibit – if they stem from the same 'mother-grain' – low angle boundaries.
- Increase of fuel grain porosity and formation of large faceted pores (~1μm size).
- Accumulation of fission products in the fuel. The fission products that occur in the fuel matrix are in solid, liquid or gas phase. Gaseous fission products can be dissolved in the fuel matrix or can be bound in precipitates. In particular fission gases (FG) can form highly pressurized nano intra-granular or micro inter-granular bubbles. In the post irradiation characterization, especially the latter have to be differentiated from large pores coming from the fabrication process.

In Figure 1.3 the SEM images of a HBS structure as a function of temperature and burn-up are shown.

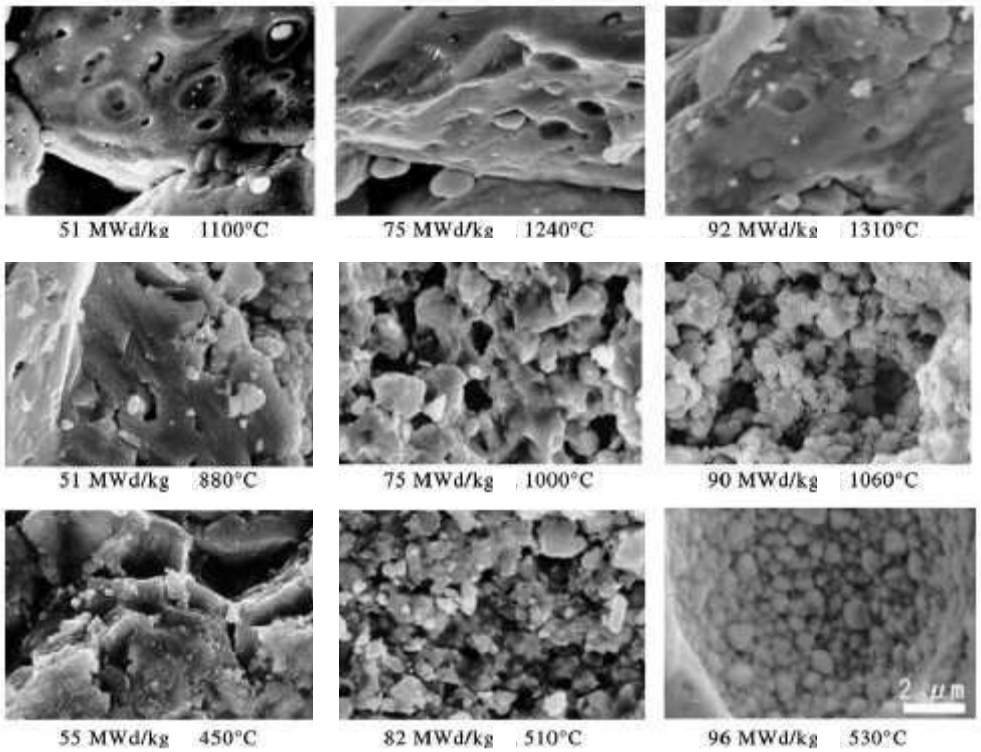

Figure 1.3: SEM images of a HBS for different temperatures and burn-ups. All pictures are same magnification [20,21].

HBS models. In the literature is a general consensus that the bubble formation coming from fission gases and HBS formation are correlated. There are several existing models developed to explain how these are connected. From the existing explanations two main trends can be distinguished.

- The first one assumes that the sub-grain formation is caused by radiation damage and the large numbers of new, much smaller grains enhance FG diffusion. According to this model moving grain boundaries sweep nano-bubbles and contribute to formation of large pores [22,23].
- According to the second model [24,25], the polygonization of the fuel occurs due to the over-pressurization of the small nm-sized FG bubbles. This model explains also the formation of larger bubbles as a consequence of an athermal, fission and irradiation induced diffusion of FG.

Both proposed models, even though being different, share the same denominator, which is the size of the fuel grain.

Larger grains extend the diffusion path for volatile fission products and thus increase fission products retention. The retention is important for noble gases coming from the fission as well as isotope built-up and decay processes. Low chemical reactivity of these noble gases results in extremely small solubility, mobile and immobile bubble formation within the grains and consequently swelling of the fuel. However, the migration, accumulation (bubbles) and re-dissolution of fission gases in the fuel lattice is complicated and depends not only on simple diffusion, but also on the respective fission element involved, the irradiation enhanced diffusion, the lattice damage, the microstructure, thermal conditions and irradiation induced resolution.

Grain enlargement options. There are several methods to increase the size of UO_2 fuel grains reported in the literature [15]. The simplest way to obtain enlarged fuel grains is to change the sintering conditions leading to continued grain growth [26]. However, this method is not economically viable for commercial fuel fabrication and also very time consuming. Another possibility is to add UO_2 or U_3O_8 seeds during the sintering process for the enhancement of the fuel grains size [27,28].

A more efficient and cost-effective option is to use another oxide powder as a dopant mixed with uranium dioxide for fuel production. Several oxide powders are mentioned in the literature and have been successfully used to increase the grain size of fuel material (e.g. MgO, Al_2O_3, Cr_2O_3, Gd_2O_3, Sc_2O_3, Y_2O_3, TiO_2, SiO_2, Nb_2O_5, V_2O_5 etc.) [15,29,30].

Chromia (Cr_2O_3) doping. The grain enlarging effect due to the addition of Cr_2O_3 is well known. Chromium sesquioxide was investigated in nuclear industry for many years. It was already described by several authors, that doping with chromium(III) oxide creates large grain microstructure as well as improves material visco-plastic characteristics [31].

A comparative analysis of most of the possible oxides that can be used as dopants for UO_2 to enlarge the fuel grain size including the sintering conditions and with respect to the final results of doping, was done by B.J. Dooies [15]. In an earlier work of Ohai *et al*. [32], the authors have studied the role of chromia doping as a function of the dopant concentration in UO_2. It has been reported that the grain growth occurs and saturates above a concentration of 0.5 wt% for Cr_2O_3 powder when mixed with UO_2. In the last

years (Aybers *et al*. [33] and Cardinaels *et al*. [34]) have described the grain growth behavior and detailed microstructure evolution during sintering process.

There are several parameters which determine the final sintered pellet characteristics of chromia doped UO_2: dopant concentration, the sintering temperature and time, the oxygen potential of the sintering environment, and heat treatments after sintering. Distribution of chromium in fresh fuel pellets, the theoretical density of chromia doped UO_2 and dopant apparent solubility have also been reported [35,36]. The excess of insoluble Cr_2O_3 always precipitates from solid solution to create second phase inclusions in sintered pellets [37,38]. Chromium precipitates were first reported by Killen *et al*. [39] who investigated higher chromia doping levels (in the range of 0.3 to 0.5 wt% Cr_2O_3) in UO_2. However, Cr-rich particles as undissolved products can be also found even in case of very low amount of doping level (~ 0.05 wt% Cr_2O_3) as published recently [36]. In Table 1.1, some of the important results on the fabrication conditions of Cr_2O_3-doped UO_2 fuel, are provided.

The solubility of the additive in UO_2 is the key to any grain size effect. There is a substantial interest also in the development of doped fuels using a mixture of different additives. For example, Arborelius *et al*. [42] have examined the UO_2 fuels containing additions of chromium and aluminium oxides. Further, in the literature [40] it is reported that doping UO_2 fuel with mixtures of chromium and other metal oxides may produce better results and improves fuel parameters in a more efficient way than doping with chromium (III) oxide alone. The physical properties and characteristics of chromia-doped UO_2 pellets from manufactured state to in-reactor performance have been investigated in the past. It has been reported that the larger grain size affects the creep properties of the fuel.

Table 1.1: Previous studies of Cr_2O_3-doped UO_2 fuels with reported grain sizes as a function of chromia concentration and sintering conditions [15].

Reference	Dopant concentration	Sintering Atmosphere	Temp. (^oC)	Time (h)	Grain size (μm)
Ainscough *et al.* (1978)[41]	0.3 wt%	-	-	-	80
Killeen *et al*. (1980)[39]	0.5 wt%	-	-	-	50-55
Kashibe *et al.* (1998)[30]	0.065 wt%	H_2	1750	2	15
Bourgeois *et al.* (2001)[37]	0.05-0.7 wt%	H_2+1vol%H_2O	1525	4	15-28
	0.05-0.7 wt%	H_2+1vol%H_2O	1625	4	29-50
	0.05-0.7 wt%	H_2+1vol%H_2O	1700	4	15-87
Ohai *et al*. (2003)[32]	0.1 wt%	H_2	1700	4	45-60
	0.3 wt%	H_2	1700	4	65-110
	0.5 wt%	H_2	1700	4	80-126
	1.0 wt%	H_2	1700	4	80-126
Aybers *et al*. (2004)[33]	100 ppm	10%H_2+90%Ar	1700	4	12-20
	1000 ppm	10%H_2+90%Ar	1700	4	13-23
	2000 ppm	10%H_2+90%Ar	1700	4	13-25
	3000 ppm	10%H_2+90%Ar	1700	4	15-27
Arborelius *et al*. (2006)[42]	<1000 ppm	H_2/CO_2	1800	14	40-55
Delafoy *et al*. (2007)[31]	0.16 wt%	-	-	-	50-60
Cardinaels *et al*. (2012)[34]	500 ppm	-	-	-	49
	1000 ppm	-	-	-	59
	1600 ppm	-	-	-	71

The addition of dopant increases the creep rate of UO_2 [43]. The thermo-gravimetric and autoclave leaching investigations done for fresh fuel revealed that chromia doping enhances the resistance of fuel pellets against oxidation as well as improves washout behaviour [29]. It should be noted, however, that due to the proprietary nature of R&D, adequate information concerning irradiated chromia doped UO_2 is not always available in the open literature. In the last several years, good experience has been gained and datasets of experimental results with subsequent PIE from irradiated Cr_2O_3-doped fuel have been produced [31,44,45]. Studies that have investigated irradiated large grain UO_2 fuels have approved in most cases the predicted decrease of fission gas release and fuel swelling. Such results can be found in Refs. [29], [46] and [47]. Today, this entire database is serving for validation of nuclear fuel performance codes.

Fuel reprocessing (MOX fuel). Although mixed oxide fuel (MOX) is topically not directly connected with chromia doped UO_2, this type of fuel has been analysed in the frame of this PhD project. There were a couple of reasons to do so: first, the analysed MOX was a very well characterized and very interesting type of experimental fuel, having been fabricated at PSI via a sol-gel route. The fuel rod filling was made in form of so-called sphere-pac. Further, the grain size of fresh and irradiated MOX fuel is barely same as for the Cr_2O_3-doped fuel [in contrast to MIMAS (Micronized Master blending) MOX fuel (~10 μm)]. Another point was that the fuel had been irradiated up to a relatively high burn-up. Eventually, this fuel was an interesting example for testing micro-XRD measurements at the synchrotron beam line. By consequence, a literature review for MOX fuel has also been made.

Principally and due to reprocessing, MOX fuel is of interest from an economic point of view. In this regard plutonium mixed UO_2 fuels are used in commercial power plants worldwide [48].

Reuse of plutonium in regular UO_2 fuel is one of the disposition options of reactor grade plutonium derived from uranium oxide spent fuels. It also plays an important role in nuclear nonproliferation (also use of Pu from military stockpiles). For commercial application the Pu-based MOX may contain around 5% PuO_2 blended with natural or depleted uranium dioxide. In order to enhance the burn-up of MOX fuel, key issue for the respective production and management (i.e., fuel fabrication, intermediate storage and reprocessing etc.) is to understand the fuel micro-structural changes [49].

The manufacturing process used to produce $(Pu,U)O_2$ fuels depends on the form of Pu supplied (PuO_2 or Pu-nitrate). One of the advanced possible – however, not industrially applied – ways of how to produce fresh plutonium-uranium MOX fuel from PuO_2 and UO_2 powder can be an internal gelation process [50]. Produced in this way fuel spheres are calcined and sintered in a reducing atmosphere (H_2+Ar) at ~1700 K.

In case of the MOX fuel fabricated at PSI, various techniques used to probe the fresh plutonium-uranium MOX fuel rod cross-section show that plutonium is homogenously distributed within the fuel pellet. The gas immersion analyses done for pristine Pu-based MOX fuels prepared by internal gelation depict slightly lower fuel density compared to

typical uranium dioxide. Also smaller lattice parameter compared to UO_2 can be noted [51].

The fission gas release determined by puncture, the luminosity of the β-γ auto-radiographies, and the volatile fission products content found by EPMA indicated a high fission gas release in the case of the Sphere-pac fuel. After base irradiation, fission gas release of 5% was determined in pelletized fuel and 29% for the Sphere-pac segment. These amounts are comparable to those found after ramp test in pelletized segments. The Sphere-pac segment presents a complete restructuring of its center after ramp. The rim effect seems to be spread over a larger distance in Sphere-pac fuel. In most of the MOX fuels tests results of PIE proved the integrity of the fuel rods up to a medium burn-up. Both, the non-destructive and destructive investigations done by several authors revealed the similar irradiation behavior and dimensional change compared to standard UO_2 fuel.

Finally, theory-based models and high performance simulations can also be found in the literature. Of particular interest for fuel modelers are experimental data on fuel temperature, diffusion of FPs and fission gas release, fuel swelling, structural changes on the macroscopic, microscopic and atomic scale. Starting with atomistic methods, such as electronic structure calculations, molecular dynamics, and Monte-Carlo, continuing with meso-scale methods, such as dislocation dynamics and phase field, and ending with continuum methods that include finite elements and finite volumes, several publications have emerged in the literature [52,53,54]. By inserting atomistic models of point defects into continuum thermo-chemical calculations, a model of oxygen diffusivity in UO_{2+x} is developed and used to predict point defect concentrations, oxygen diffusivity, and fuel stoichiometry at various temperatures and oxygen pressures [55]. In order to establish the mechanism of solubility for a range of trivalent oxides in doped uranium dioxide fuels, atomic scale simulations have been carried out by Middleburgh *et al.* [56,57]. A review of advanced nuclear fuel performance codes reveals that many codes are dedicated to specific fuel forms and make excessive use of empirical correlations in describing properties of materials. Although important, the diffusion of fission products not well understood due to the lack of in-situ characterization methods. Also, the role of diffusion at the grain boundaries is still unclear. This phenomenon is strongly related to microstructure evolution and must be further studied using advanced experimental

techniques. The present thesis work presents experimental investigation of irradiation-induced atomic scale micro-structural changes occurring in irradiated nuclear fuels providing new results to this subject.

1.4 References

1 J.S. Tulenko, *Nuclear reactor materials and fuels*, Encyclopedia of Sustainability Science and Technology (2013).

2 S.G Prussin, *Release of Fission Products (Xe, I, Te, Cs, MO and Tc) from polycrystalline UO_2,* J. Nucl. Mater., 154 (1988) 25-37.

3 Ainscough *et al*., *The effect of titania on grain growth and densification of sintered UO_2,* J. Nucl. Mater. 52 (1974) 191-203.

4 K.C. Radford and J.M. Pope, *UO_2 Fuel Pellet Microstructure Modification through Impurity Additions*, J. Nucl. Mater. 116 (1983) 305-313.

5 Ch. Riglet-Martial *et al., Thermodynamics of Chromium in UO_2 Fuel: a Solubility Model*, J. Nucl. Mater. 447 (2014) 63-72.

6 S. Kim *et al., Sintering beviour of Cr_2O_3-doped UO_2 pellets,* J. Kor. Nucl. Soc. 35 (2003) 14-24.

7 http://www.areva.com

8 K. Une *et al., Fuel oxidation and irradiation behavior of defective BWR fuel rods,* J. Nucl. Mater. 223 (1995) 40-50.

9 L. E. Herranz and F. Feria, *Spent fuel rod splitting due to UO_2 oxidation during dry storage:Assessment of the database,* Prog. Nucl. Ene. 51 (2009) 201-206.

10 J.M Warde and J.R Johnson, *Recent developments in the technology of ceramic materials for nuclear energy service,* J. Franklin Inst. 260 (1955) 455-466.

11 F.S. Martin and E.W. Hooper, *The distribution of plutonium and fission products between molten uranium and molten uranium trifluoride-barium halide mixtures,* J. Inorg. Nucl. Chem. 4 (1957) 93-99.

12 F. Schmitz and R. Lindner, *Diffusion of heavy elements in nuclear fuels: actinides in UO_2,* J. Nucl. Mater. 17 (1965) 259-269.

13 R.M. Cornell *et al., The role of bubbles in fission gas release from uranium dioxide,* J. Nucl. Mater. 30 (1969) 170-178.

14 A.H. Booth, *A method of calculating fission gas diffusion from UO_2 fuel and its application to the X-2-f loop,* CRDC-721, Atomic Energy of Canada (1957).

15 B.J. Dooies, Master Thesis, *Enhancement of Uranium Dioxide Thermal and Mechanical Properties by Oxide Dopants,* University of Florida (2008).

16 *Method for Calculating the Fractional Release of Volatile Fission Products from Oxide Fuel,* American Nuclear Society ANSI/ANS-5.4-2011.

17 R. Lindner and Hj. Matzke, *Diffusion von Xe^{-133} in Uranoxyd verschiedenen Sauerstoffgehaltes,* Z. Naturforsch. Pt. A, 14 (1959) 582-584.

18 S. Nicoll *et al., A computational study of the effect of Xe concentration on the behaviour of single Xe atoms in UO_2,* J. Nucl. Mater. 226 (1995) 51-57.

19 J. A. Turnbull *et al., The diffusion coefficients of gaseous and volatile species during the irradiation of uranium dioxide,* J. Nucl. Mater. 107 (1982) 168-184.

20 D. Baron *et al., Discussion about HBS transformation in high burn-up fuels,* Nucl. Engin. and Tech. 41 (2009) 199-214.

21 T. Sonoda *et al., Transmission electron microscopy observation on irradiation induced* microstructural evolution in high burn-up UO_2 disk fuel. Nucl. Instrum. Meth. B., 191 (2002) 622-628.

22 K. Nogita *et al., Effect of grain size on recrystallization in high burnup fuel pellets,* J. Nucl. Mater. 248 (1997) 196–203.

23 K. Une *et al., Rim structure formation and high burnup fuel behaviour of large-grained UO_2 fuels,* J. Nucl. Mater. 278 (2000) 54–63.

24 J. Spino *et al., High burn-up rim structure: evidences that xenon-depletion pore formation and grain subdivision start at different local burnups,* J. Nucl. Mater. 256 (1998) 189–196.

25 H. Matzke and J. Spino, *Formation on the rim structure in high burnup fuel,* J. Nucl. Mater. 248 (1997) 170–179.

26 Y. Harada and S. Doi, *Irradiation Behaviour of Large Grain UO_2 Fuel Rod by Active Powder,* J. Nucl. Sci. Technol., 35 (1998) 411-418.

27 K.W. Song *et al., High burnup fuel technology in Korea,* Nucl. Engin. and Tech. 40 (2008) 21.

28 J.W. Rhee *et al., Effect of U3O8-seed on the grain growth of uranium dioxide,* J. Kor. Cryst. Growth and Cryst. Tech. 17 (2007) 75-81.

29 *Advanced Fuel Pellet Materials and Fuel Rod Design for Water Cooled Reactors,* IAEA (2010).

30 S. Kashibe and K. Une, *Effect of additives (Cr_2O_3, Al_2O_3, SiO_2, MgO) on diffusional release of ^{133}Xe from UO_2 fuels*, J. Nucl. Mater., 254 (1998) 234-242.

31 C. Delafoy *et al., Cr_2O_3-doped fuel development and qualification*, Annual Meeting on Nuclear Technology (2007).

32 D. Ohai *et al., Large grain size UO_2 sintered pellets obtaining used for burnup extension*, International Conference on Structural Mechanics in Reactor Technology, Prague (2003).

33 Aybers *et al., Grain growth in corundum-oxides doped uranium dioxide and effects of grain growth to the mechanical properties of uranium dioxide such as elasticity determined by ultrasonic methods*, Key Eng. Mater. 264-268 (2004) 985-988.

34 T. Cardinaels *et al., Chromia doped UO_2 fuel: Investigation of the lattice parameter*. Nucl. Mater. 424 (2012) 252.

35 A. Leenaers *et al., On the solubility of chromium sesquioxide in uranium dioxide fuel*, J. Nucl. Mater., 423 (2012) 93-101.

36 T. Cardinaels *et al., Dopant solubility and lattice contraction in gadolinia and gadolinia-chromia doped UO_2 fuels*, J. Nucl. Mater., 424 (2012) 289-300.

37 L. Bourgeois *et al., Factors governing microstructure development of Cr_2O_3-doped UO_2 during sintering*, J. Nucl. Mater., 297 (2001) 313-326.

38 S. Kim *et al., Sintering beviour of Cr_2O_3-doped UO_2 pellets*, J. Kor. Nucl. Soc. 35 (2003) 14-24.

39 J. C. Killeen *et al., Fission gas release and swelling in UO_2 doped with Cr_2O_3*, J. Nucl. Mater., 88 (1980) 177-184.

40 H. Assmann *et al., Doping UO_2 with niobia- beneficiary or not?*, J. Nucl. Mater. 98 (1981) 216.

41 Ainscough *et al., Int. Symp. on water reactor fuel fabrication with special emphasis on its effect on fuel performance*, IAEA (1978).

42 Arborelius *et al., Advanced doped UO_2 pellets in LWR applications*. J. Nucl. Sci. Tech. 43 (2006) 967-976.

43 C. Nonon *et al., PCI Behaviour of Chromium Oxide-Doped Fuel*, OECD, Nuclear Energy Agency (2005).

44 J. Noirot *et al.*, *Detailed characterisations of high burn-up structures in oxide fuels*, J. Nucl. Mater. 372 (2008) 318-339.

45 N. Marchal *et al.*, *Finite element simulation of Pellet-Cladding Interaction (PCI) in nuclear fuel rods*, Comp. Mater. Sci. 45 (2009) 821-826.

46 Y. Harada, *Sintering behaviour of niobia-doped large grain UO_2 pellet*, J. Nucl. Mater. 238 (1996) 237-243.

47 R. Yuda *et al.*, *Effects of pellet microstructure on irradiation behavior of UO_2 fuel*, J. Nucl. Mater. 248 (1997) 262-267.

48 D. Hass and D.J Hamilton, *Fuel cycle strategies and plutonium management in Europe*, Prog. Nucl. Energy 49 (2007) 574-582.

49 J.L. Francois *et al.*, Study *of the radiotoxicity of actinides recycling in boiling water reactors fuel*, Nucl. Eng. Des. 239 (2009) 1911-1915.

50 C. Degueldre *et al.*, *Curium analysis in plutonium uranium mixed oxide by x-ray – fluorescence and -absorption fine structure spectroscopy*, Talanta, in press 2013.

51 M.A. Pouchon *et al.*, *Fabrication and Characterization of MOX Microspheres for the FUJI Project*, (2003).

52 W. M. Stacey, *Nuclear Reactor Physics*, John Wiley & Sons. Inc. New York (2001).

53 M. Abramowski, *Atomistic Simulations of the Uranium-Oxygen System*, PhD Thesis, Imperial College (2001).

54 A. Romano *et al.*, *Fuel performance analysis for PWR cores*, Nuclear Engineering and Design 239 (2009) 1481-1488.

55 M. Stan, *Multi-scale models and simulations of nuclear fuels*, Nuclear Engineering and Technology 41 (2009) 39-52.

56 S.C. Middleburgh *et al.*, *Solution of trivalent cations into uranium dioxide*, J. Nucl. Mater. 420 (2012) 258.

57 S.C. Middleburgh *et al.*, *Swelling due to fission products and additives dissolved within the uranium dioxide lattice*, J. Nucl. Mater. 427 (2012) 359-363.

Chapter 2: Experimental Method and Background

2.1 Material

In this work the following fuel samples were investigated:

- Fresh and irradiated standard UO_2.
- Fresh and irradiated Cr_2O_3-doped UO_2. It may be noted that the standard and Cr_2O_3-doped irradiated fuel samples stem from the same fuel assembly used in the reactor.
- Fresh and irradiated $(U,Pu)O_2$ MOX fuel (produced at PSI with internal gelation)

The average grain size of the uranium-plutonium mixed oxide fuel is between that of the standard UO_2 and chromia-doped UO_2. However, the average burn-up of irradiated MOX fuel is much higher. Details of all three types of fuels are mentioned below:

Chromia-doped UO_2. Fresh doped fuel material containing 1600 ppm of Cr_2O_3 was sintered with standard uranium dioxide powder, which was enriched up to ~4.8% ^{235}U. The UO_2 powder used for sintering was obtained from the dry-conversion process. In Figure 2.1a microscopic view of powder morphology is presented. The doped fuel material also contains a trace amount of aluminium (due to the use of Al-base lubricant at manufacturing step). Average grain size of the fresh fuel, enlarged by doping with Cr_2O_3, is about ~40 μm. The fuel was irradiated in the Swiss commercial light water reactor of KKG, a PWR, for two cycles with an average burn-up of ~39.3 MW d kg^{-1}.

AREVA has conducted many research programs in order to improve UO_2 fuel [1,2]. To be able to study the role of the Cr concentrations and effect of different sintering conditions, UO_2 fuel pellets with different Cr contents sintered under different conditions were produced [2,3,4]. Additional data regarding sintering for different fuel samples are detailed in Chapter 1.3. In Figure 2.1b sintering conditions of investigated chromia-doped fuel that is used for this study are presented.

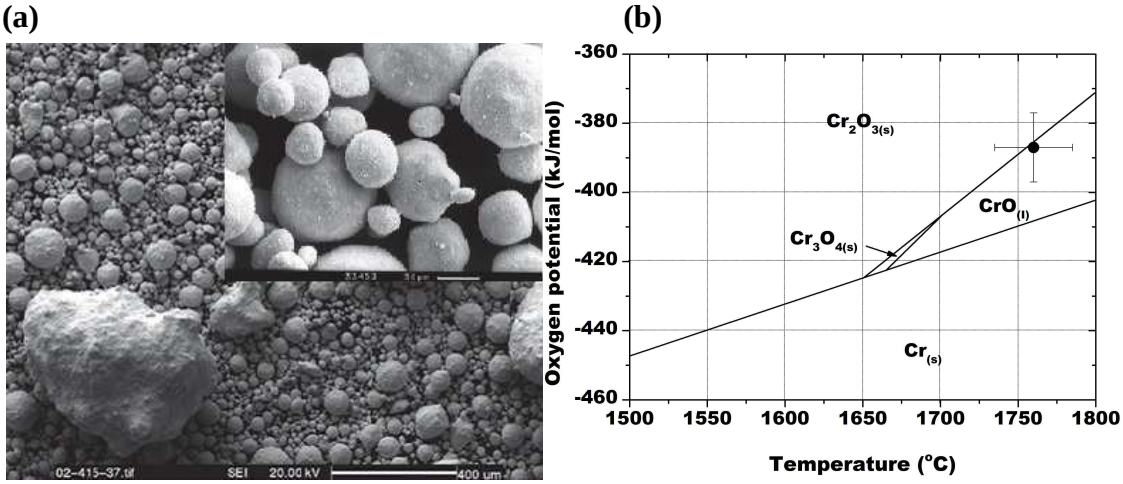

Figure 2.1: (a) Morphology and size distribution of UO_2 powder particles used for fuel manufacturing; (b) Cr-O phase diagram with given sintering conditions (the marked point) of the Cr_2O_3-doped UO_2 fuel analyzed in this work [2,3,4,5].

Standard UO_2. Standard UO_2, having an average grain size of about 10 μm, was used for the comparative study with Cr_2O_3-doped UO_2. The standard fuel was irradiated in the same assembly as the chromia-doped fuel, under the same reactor conditions, and also for two cycles. The average burn-up in the pellets of the irradiated standard fuel is very comparable to that of the chromia-doped ones.

(U,Pu)O_2 fuel. The studied (U,Pu)O_2 MOX originally contained 4.7 wt% Pu. The fuel was prepared in 1989 at the PSI Hot-Laboratory using the internal gelation process producing small fuel micro-spheres. The average size of the fuel grains was about ~40 μm. The microspheres were filled into segments forming the so-called MOX sphere-pac fuel. After fabrication the segments were transferred to the Swiss pressurized water reactor Beznau-1 for irradiation. The irradiated fuel was discharged after 6 reactor cycles, having reached an average burn-up of about 60 MW d kg^{-1}. The spent fuel was transferred back to PSI where post irradiation examinations (PIE) were completed in the year 2000.

The SEM and ceramographic pictures taken for all fresh analyzed samples are shown in Figure 2.2.

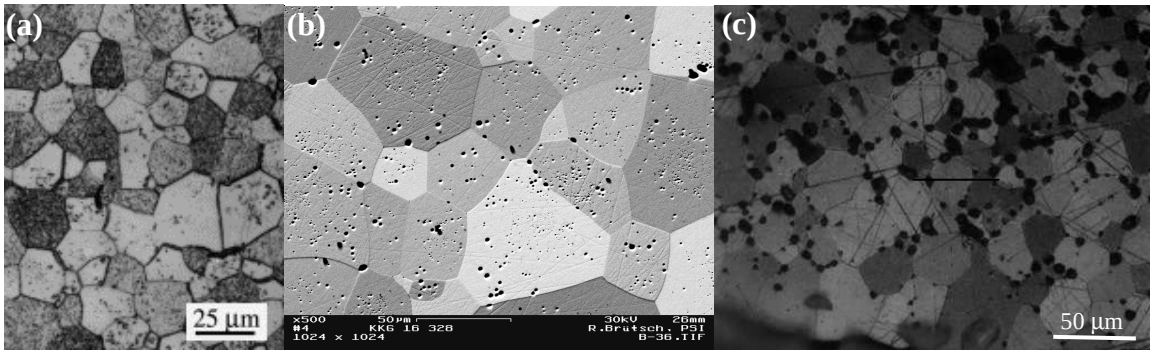

Figure 2.2: SEM and ceramographic pictures of fresh (a) standard UO_2, (b) Cr_2O_3-doped UO_2, (c) $(Pu,U)O_2$ MOX fuel. The image (a) of the standard fuel is taken from Ref. [6].

2.2 Sample preparation method

In contrast to spent fuel, the fresh fuel sample preparation was very straight forward: the fresh fuel specimens were taken from a section of an UO_2 pellet. Wedge shaped specimens were prepared by the pre-thinned near-apex method. It was essential to produce thinner areas at the sample edge for micro-beam XRD analysis in transmission mode.

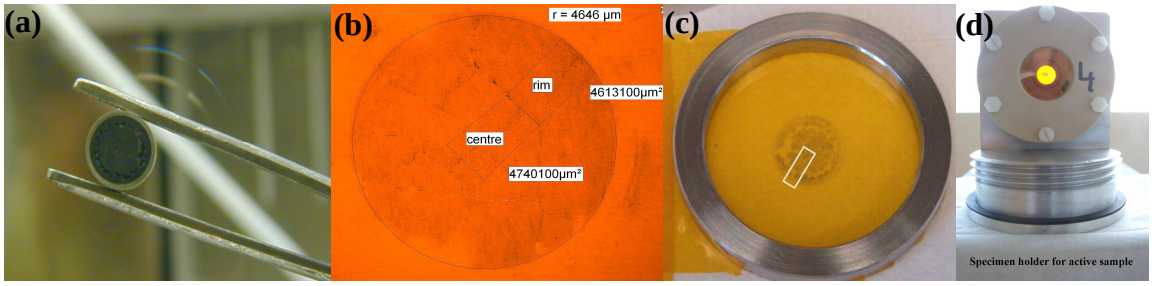

Figure 2.3: (a) Cross-section of the irradiated MOX fuel rod (b) Replicated sub-samples (with given areas) obtained from the irradiated pellet. (c) Fuel particles on adhesive Kapton foil. The white rectangle shows the strip prepared for mounting in the XAS sample holder. (d) The specimen holder for the measurements at the synchrotron facility.

Due to the very high radioactivity as well as the dose-rate of the irradiated pellets, small sub-samples were required to stay below the dose-rate limit allowed at the synchrotron facility. A newly developed peeling procedure was adopted to prepare irradiated fuel specimens. For that purpose, a section of the fuel segment was ground using a silicon carbide disc and sand paper; small fuel particles were generated.

A replica print of the ground surface of the pellet cross section was made on an adhesive Kapton tape and fuel particles were collected. Thereafter, thin strips of the sub-samples

were cut out and mounted on a specifically designed radioactive sample carrier. The first part of the work was performed remotely in a hot-cell (fuel rod cutting, grinding and replicate), the second in a fume hood (cutting thin strips).

Sub-samples were prepared taking fuel particles from the centre (IC) and rim (IR) regions of the irradiated fuel pellets. Here, IC and IR represents irradiated centre and irradiated rim, respectively. Since the irradiation effects are expected to be different at different locations along the radial distance of a spent fuel pellet, we have selected two regions for preparing the sub-samples. Total activity of sub-samples prepared from the centre region and/or rim area of the irradiated pellets were in the range $0.6 - 1.4 \times 10^4$ Bq. Note that these abbreviations IR and IC will be used in the subsequent chapters to distinguish samples analyzed in this work for a given type of irradiated fuel material.

In Figure 2.3, the cross-sectional view of the irradiated MOX fuel pellet, an optical micrograph of the replicated sample and a photograph of the active sample carrier containing a sub-sample are shown. Further details for the preparation of irradiated fuel specimens including the experimental arrangement are described in Refs. [7,8].

Table 2.1: Properties of analyzed fuel samples.

Specimen identification	Fuel type	Average burn up (MW d kg^{-1})	Average grain size (µm)	^{235}U content (wt%)	Cr content (µg/g)
Sample-1	Fresh pellet	–	48	4.8	1080
Sample-2	Fresh pellet	–	10	4.9	< 5
Sample-3	Irradiated pellet	39.3	10	4.9[b]	< 5
Sample-4	Irradiated pellet	39.6	38[a]	4.8[b]	1080
Sample-5	Fresh MOX	–	40	0.8	–
Sample-6	Irradiated MOX	60	30	0.8[b]	–

[a]Averaged, indicative value measured in PSI hotlab according to procedure ASTM-E-112, not reflecting the grain size distribution as function of pellet radius.
[b] Initial content.

2.3 Beamline setup and experimental conditions

The synchrotron-based μ-XRF, μ-XRD and μ-XAFS microscopic techniques were used for investigations at the X05LA Micro-XAS beam line of the Swiss Light Source (SLS). This beam line provides high brilliance X-rays in the energy range of 5–20 keV with dynamic micro-focusing capabilities. A photograph of the end-station at the micro-XAS beam line showing the available experimental facilities is given in Figure 2.4.

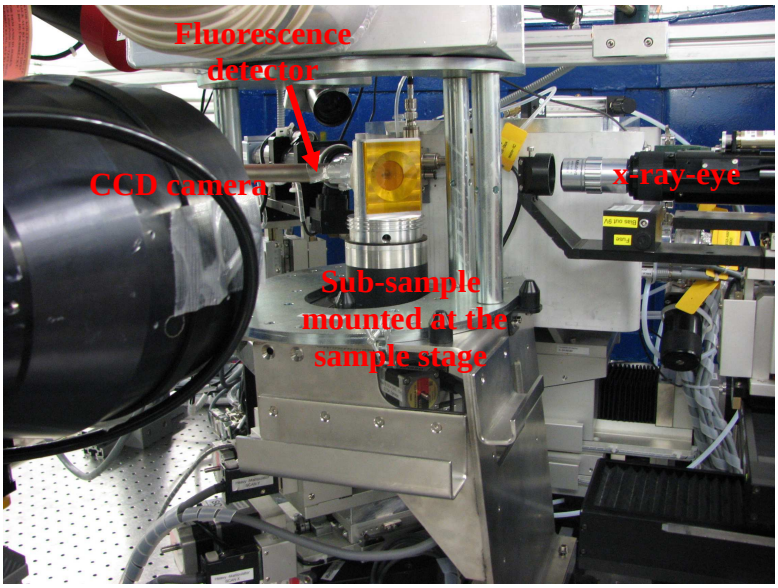

Figure 2.4: A rear view of the experimental arrangement at X05LA (Micro-XAS) beam line for measurements on radioactive fuel samples.

Due to the broad energy spectrum measurable at the end station of the micro-XAS beamline a wide range of elements can be identified and analysed. In addition, the local shielding at the end station of the beam line allows investigation of radioactive materials. The permitted activity for a single active-sample accepted at the beam line is below 100 LA, where LA stands for the French abbreviation of authorization limit (l'imite d'Autorisation). In Table 2.2 various elements that can be analyzed are listed and the electron binding energies (K and L shells) are mentioned. Highlighted in green are excitation energies used at the beam line for the identification and measurements. Highlighted in red are elements mentioned/used in this study.

Using the focusing devices and the liquid nitrogen cooled double-crystal monochromator (a pair of Si (111) crystal) the beam line can provide a monochromatic and focused X-ray beam of 1 μm × 1 μm spot size on the sample. The sample holder (see Fig. 2.3) was positioned on a small table remotely controlled by a three axis-motion manipulator for accurate positioning of the investigated specimens.

Table 2.2: Electron binding energies in electron volts for elements that can be measured at the MicroXAS beamline.

Element	K1s (eV)	L_I2s (eV)	$L_{II}2p_{1/2}$ (eV)	$L_{III}2p_{3/2}$ (eV)
Ti	4966	560.9	460.2	453.8
V	5465	626.7	519.8	512.1
Cr	5989	696.0	583.8	574.1
Mn	6539	769.1	649.9	638.7
...	…	…	…	…
Se	12658	1652.0	1474.3	1433.9
Br	13474	1782	1596	1550
Kr	14326	1921	1730.9	1678.4
Rb	15200	2065	1864	1804
Sr	16105	2216	2007	1940
Y	17038	2373	2156	2080
Zr	17998	2532	2307	2223
Nb	18986	2698	2465	2371
Mo	20000	2866	2625	2520
…	…	…	…	…
Xe	34561	5453	5107	4786
Cs	35985	5714	5359	5012
Ba	37441	5989	5624	5247
La	38925	6266	5891	5483
Ce	40443	6549	6164	5723
Pr	41991	6835	6440	5964
Nd	43569	7126	6722	6208
Pm	45184	7428	7013	6459
Sm	46834	7737	7312	6716
Eu	48519	8052	7617	6977
Gd	50239	8376	7930	7243
Tb	51996	8708	8252	7514
Dy	53789	9046	8581	7790
...	…	…	…	…
Pb	88005	15861	15200	13035
Bi	90524	16388	15711	13419
Po	93105	16939	16244	13814
At	95730	17493	16785	14214
Rn	98404	18049	17337	14619
Fr	101137	18639	17907	15031
Ra	103922	19237	18484	15444
Ac	106755	19840	19083	15871
Th	109651	20472	19693	16300
Pa	112601	21105	20314	16733
U	115606	21757	20948	17166

μ-XRF measurements. The region for detailed μ-XRD and μ-XAFS measurements in irradiated specimens was determined using synchrotron-based analytical μ-XRF mapping. The elements analyzed in XRF were uranium (using the L_α line intensity), krypton (K_α line) and chromium (K_α peak). The fluorescent X-rays were collected using a SiLi drift

solid state detector (SSD) from KETEK. The μ-XRD and μ-XAFS experiments were performed at the same area of the μ-XRF measurements.

μ-XRD measurements. All μ-XRD measurements were performed at room temperature and the energy of the incident X-ray was set to 17200 eV. A charge coupled device (CCD) camera (photonic science, UK) was used to collect the diffraction patterns in transmission mode by exposing the sample to X-rays with 2–5 seconds exposure time. The distance from the edge of the film to the CCD camera (L) was 60 ± 1 mm. In order to prevent damaging the CCD camera, non scattered X-rays were blocked with a 'beam-stop'. The CCD images were integrated and converted to 1-D intensity versus 2θ plots with the help of XRDUA [9] and FIT2D [10] software. The peak positions (2θ) and corresponding angular half-widths (FWHM) were measured. Phase identification and unit cell indexing of XRD were carried out using the Match software package [11].

The CCD area detector uses each pixel as an addressable individual detector, so the spatial position and the energy of an X-ray event can be simultaneously recorded. The range of detection is based on the distance between sample and the camera, as well as the width of the CCD. The range of diffraction is measured in 2θ, the angle of scattering between the incident beam and the diffracted X-rays. The relation of the CCD spot position to the Bragg angle is calibrated by recording Laue patterns from a reference corundum (α-Al_2O_3) powder specimen.

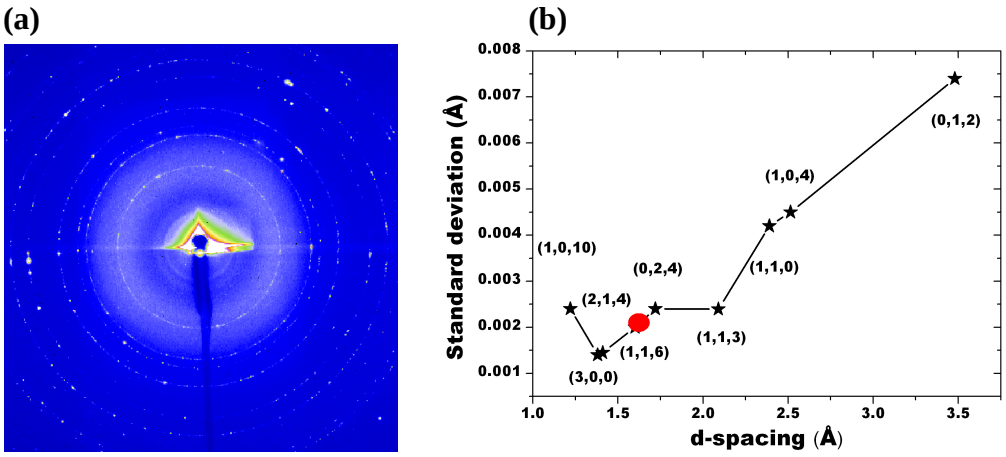

Figure 2.5: (a) μ-XRD pattern and; (b) plot of the standard deviation of the interplanar spacings versus d-values of some XRD lines of corundum Al_2O_3, determined under the given experimental conditions used in this work. The marked red dot corresponds to the d-spacing for (311) reflection in UO_2.

While the diffraction resolution is limited by the spot size of the incident beam as well as the pixel size of the CCD, the accurate measurement of lattice parameters is a function of proper experimental conditions. An example of the diffraction pattern collected from an Al_2O_3 powder reference sample is shown in Figure 2.5. The image is captured out to 48^o (2θ value) based on the width of the CCD. The relative intensities of the diffraction spots are particularly useful for identifying various $d_{(hkl)}$ reflections from the corundum α-phase of alumina. Diffraction rings observed in Figure 2.5a are fitted to determine peak positions (2θ) and angular half-widths in the line profile analysis. Least-squares refinement of peak positions yields unit-cell parameters of Al_2O_3. The estimated uncertainty in the analysis of interplanar spacings (d) is shown in Figure 2.5b. Due to the decreasing trend in uncertainties for extracting lattice parameters from higher order reflections, the (311) reflection of UO_2 is used for detailed quantifications of lattice parameters (see red spot in Figure 2.5b). It leads to measure the unit cell crystal spacing of UO_2 within an accuracy of ± 0.002 Å.

μ-XAFS measurements. All μ-XAFS measurements were performed at room temperature. The incident photon energies were calibrated using a metallic Zr foil, a selenium powder specimen and a Cr-metal foil, respectively, for uranium, krypton and chromium absorption edges. The energy scans were recorded in the range from 17.1 to 17.8 keV for the uranium L_{III}-edge, from 14.2 to 14.8 keV for the krypton K edge and from 5.9 to 6.7 keV for the chromium K-edge by adjusting the Si(111) double-crystal Bragg monochromator.

2.4 Theoretical approach

The analyses of the fuel samples were carried out with various analytical techniques. Most of the presented results are based on synchrotron light microscopy techniques; the theoretical basics of these techniques are described below. There are some results obtained using other analytical instruments (e.g. electron probe micro-analyzer) as well as specialized PC software.

2.4.1 X-ray fluorescence

X-ray fluorescence is a non-destructive method that is used widely for the analysis of material elemental composition. The method is based on the principle that individual atoms, when excited by an external energy source, emit X-ray photons of a characteristic energy of those atoms. Due to the different characteristic energies of different elements it is possible to perform qualitative and quantitative analysis of the sample composition. Qualitative analysis is based on the identification of elements and quantitative consists in the calculation of the amount of the respective elements [12].

Formation of characteristic X-ray lines: The photo-electric effect causes photo-electrons from the atoms shells to be ejected due to their energy above the binding energy and the absorption of energetic incident photons. Created in this way, photo-electrons have a kinetic energy equal to the absorbed energy minus the electron binding energy. The electron vacancies created cause an unstable environment for the atom. As the atom reestablishes, electrons from the outer shells are transferred to the inner shells and during this transfer a characteristic X-ray is generated. The energy of the emitted photon is equal to the energy difference between the two binding energies of the corresponding shells. Each element produces characteristic X-rays of a unique set of energies that can be recorded as spectral lines. This allows identification of the elemental composition of a sample.

In most cases the innermost K and L shells are involved in XRF detection. A typical X-ray spectrum from a sample can display multiple peaks of different intensities, depending on the energies of the incident photons or wavelengths.

The characteristic X-rays are labeled as K, L, M or N X-rays to denote the shells they originated from. For example, a K_α X-ray is produced from a transition of an electron from the L to the K shell, and a K_β X-ray is produced from a transition of an electron from the M to a K shell. Within the shells, multiple orbits of higher and lower binding energy electrons are found. Further designation is α_1, α_2 or β_1, β_2, etc. together with the shells (K, L, etc.) to denote transitions of electrons from these orbits into the same lower shell. A schematic diagram of this process is shown in Fig. 2.6.

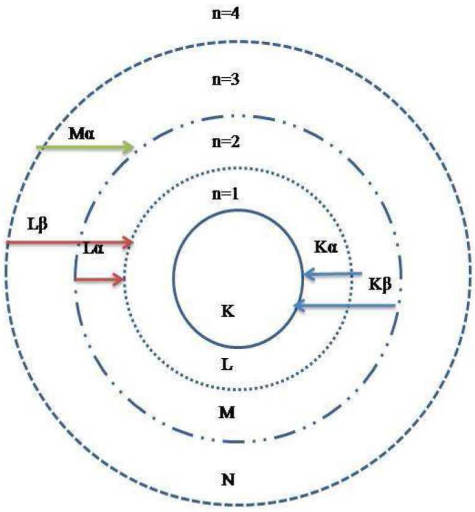

Figure 2.6: Electron shells transition diagram.

In this thesis investigations are performed using synchrotron based X-rays. It may be mentioned that depending on the application, the fluorescent light can also be produced by using other primary excitation sources like energetic alpha particles, protons or high energy electron beams. In the EPMA (electron probe micro-analysis) analysis, fluorescent X-rays are produced by high energy electron beams [13].

2.4.2 X-ray diffraction

X-ray diffraction (XRD) is based on the constructive interference of mono- and/or polychromatic X-rays incident on crystalline materials.

Laue diffraction. It was discovered and firstly described in 1912 by Laue, Friedrich and Knipping in Munich [14,15]. Laue and his co-workers envisaged crystals in terms of a 3D network of rows of atoms. They made their analysis based on the notion that a crystal behaved as a 3D diffraction lattice.

Figure 2.7 shows Laue conditions for a part of a crystal considering only the x-axis. The constructive interference will take place if the path difference is a whole number of wavelengths.

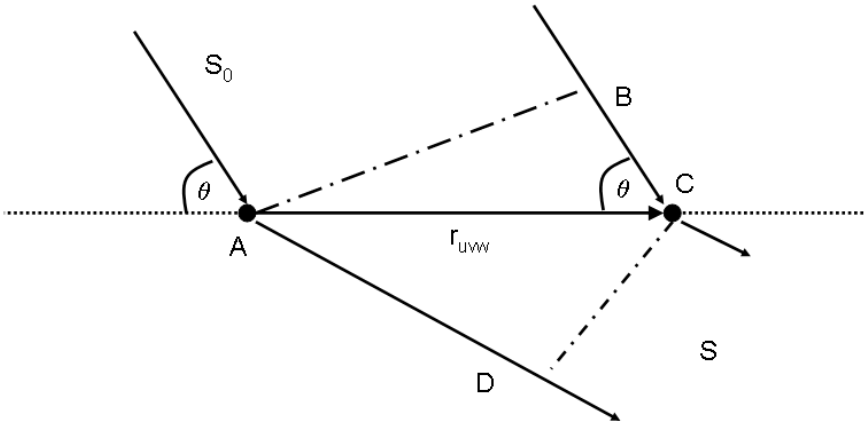

Figure 2.7: The incident (S_0) and diffracted beam (S) directions and the difference between diffracted beams (AD-BC).

The optical path difference is given by:

$$\Delta = \text{AD-BC} \tag{2.1}$$

From this it is easy to arrive to the following equation:

$$r_{uvw} \cdot \mathbf{h} = (ua+vb+wc) \cdot \mathbf{h} = \text{integer} \tag{2.2}$$

where: **h** is the diffraction vector (**h** = S-S_0) and coefficients u,v,w - any integers.

Finally this equation (2.2) can be rewritten as:

$$\mathbf{a} \cdot \mathbf{h} = h \tag{2.3}$$

$$\mathbf{b} \cdot \mathbf{h} = k \tag{2.4}$$

$$\mathbf{c} \cdot \mathbf{h} = l \tag{2.5}$$

Equations (2.3-2.5) are known as Laue equations.

The Laue method can be two types, transmission and back-reflection method, depending on the relative position of the X-ray source, sample and the detector. In the transmission mode the detector is placed behind the sample to record the beams diffracted in the forward direction. In Laue diffraction, the diffracted beam produces an array of spots lying on certain curves (such as, ellipses or hyperbolas) forming the Laue pattern, also called Laue-diagram. A schematic representation of the transmitted Laue diffraction is shown in Fig. 2.8.

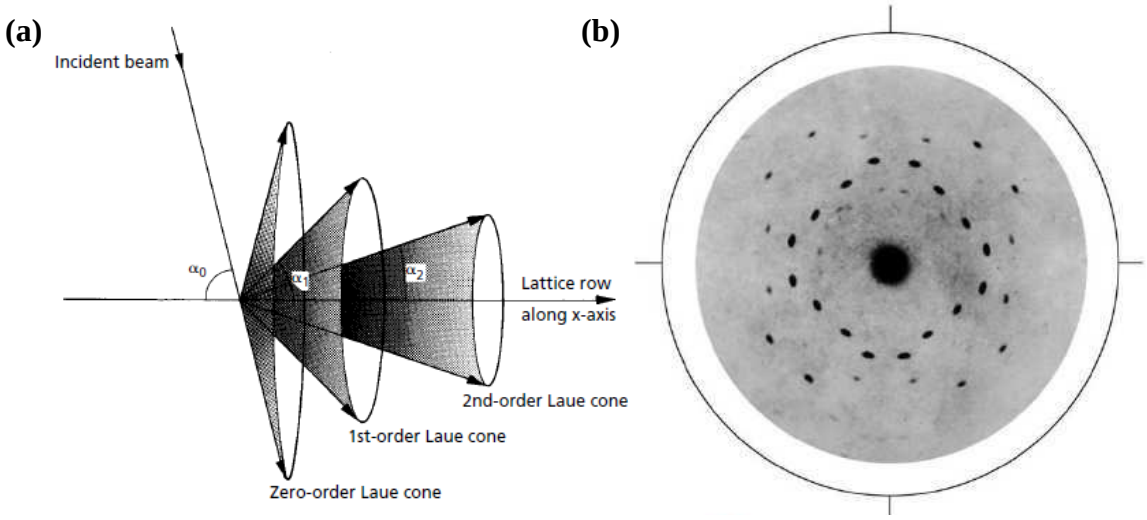

Figure 2.8: (a) Three Laue cones representing the directions of the diffracted beam from a lattice row along the x-axis [16]; (b) Internal atomic regularity on a 'Laue Diagram' is shown. This result was presented at the Bavarian Academy of Science meeting on June 8th 1912. [15].

Bragg equation. In England, William Henry Bragg and William Lawrence Bragg, father and son, respectively, developed a method by which they confirmed the result obtained by Laue. They envisaged crystals in terms of planes of atoms, which behave in effect as reflecting planes (angle of incident and angle of reflected beam are equal) [16,17]. In their model strong reflected beams are produced when the path difference between reflected and incident beam is equal to whole number of wavelengths.

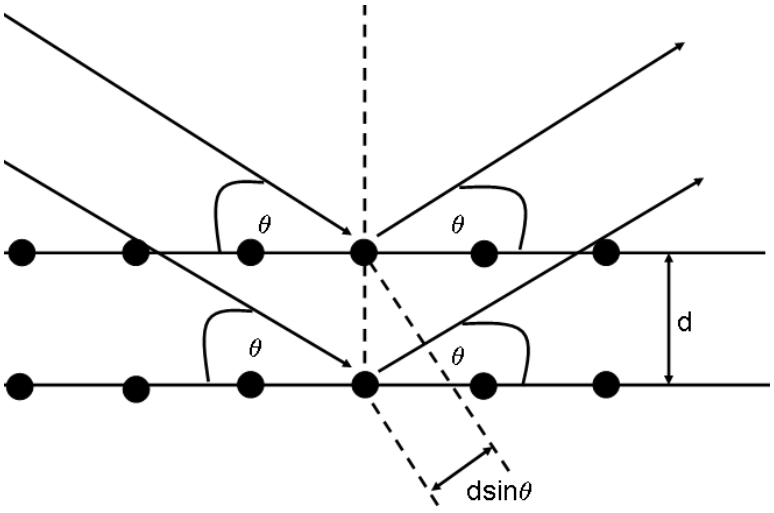

Figure 2.9: Bragg diffraction interpretation. Incident beam is reflected with same angle. The optical path difference between two rays is equal to 2dsinθ.

The Bragg's law may be derived from Figure 2.9 which shows crystal lattice planes and atoms. Using simple geometric rules it can be shown that the constructive interference appears when the following condition is satisfied:

$$n\lambda = 2\,d\,\sin\theta \tag{2.6}$$

This equation 2.6 is the Bragg's law equation. When Bragg's law is satisfied constructive interference occurs. XRD is most widely used for the identification of unknown crystalline materials. Other applications can include determination of unit cell dimensions and crystal structure, orientation of a single crystal or grain, and measurements of size, shape and internal stress of small crystalline regions.

2.4.3 X-ray absorption fine structure

X-ray absorption fine structure (XAFS) spectroscopy is a powerful technique to determine the local structure (electronic and geometric) around the absorbing atoms. XAFS spectroscopy began to emerge as a practical experimental tool in the early Seventies. Using XAFS, a sample is probed with X-rays having the incident energy higher than the binding energy of the core shell-electrons of the studied absorbing element.

EXAFS basics. The incident x-rays can be absorbed and / or the photo-electric effect occurs.

The parameter which gives the probability that x-rays will be absorbed according to Beer-Lambert's Law is the absorption coefficient (μ). The absorption coefficient is a smooth function of energy that is dependent on the sample density (ρ), the atomic number (Z), the atomic mass (A), and the energy of the X-ray (E) as:

$$\mu \approx \frac{\rho Z^4}{AE^3} \tag{2.7}$$

When the energy of the incident X-rays approaches the electron binding energy of a core level electron, there is a sharp rise in the absorption coefficient as the cross-section of the X-ray increases (photo-electric effect). The first inflection point of the rise in the

absorption edge energy spectrum is denoted as the threshold energy or the absorption edge energy (E_0). When the energy of incoming photon is larger than E_0, the momentum (p) of the outgoing photoelectron can be expressed as:

$$p = \sqrt{2m(E - E_0)} \tag{2.8}$$

where m represents the mass of the electron.
Using the de Broglie relation [18], equation (2.8) can be expressed in terms of the wavelength of the photoelectron, λ, as:

$$\lambda = \frac{h}{\sqrt{2m(E - E_0)}} \tag{2.9}$$

where h is the Planck's constant. EXAFS can be understood taking into account the wave behaviour of the photo electron.

The collected XAS spectrum can be divided into different parts. This is normally done based on the energy range of the measured absorption spectrum and with respect to the absorption edge.

A typical division specifying different regions is presented below:

- The pre-edge region - no ionization occurs.
- XANES (X-ray Absorption Near Edge Structure), edge region ($E=E_0 \pm 10$ eV).
- NEXAFS (Near-Edge X-ray Absorption Fine Structure) region between ($E_0+10\ eV < E < E_0+50$ eV).
- EXAFS (Extended X-ray Absorption Fine Structure) region ($E > E_0+50$ eV).

The rising part of the absorption edge itself is sometimes not considered to be in the XANES region, and the beginning of this region is set at $E > E_0+5$ eV. Sometimes the division between the XANES-NEXAFS and EXAFS region is set around 150 eV. A typical XAFS spectrum is shown in Figure 2.10.

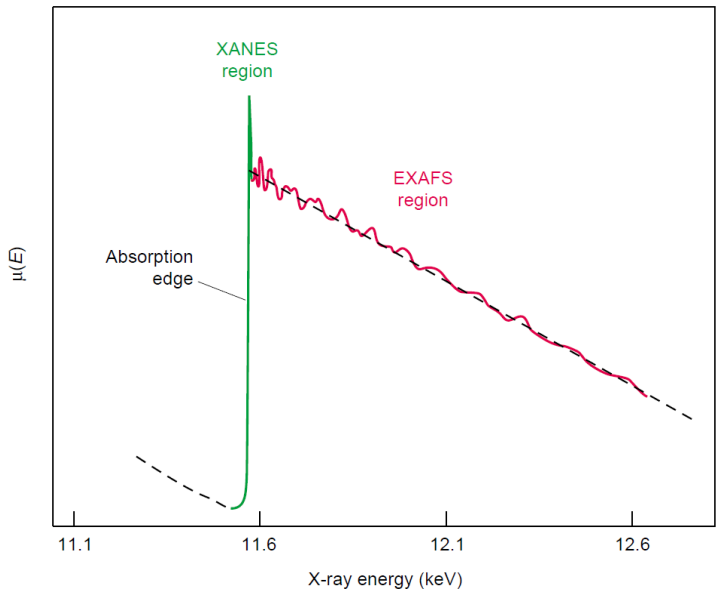

Figure 2.10: Typical XAFS spectrum of a platinum foil. With the green and red colours, respectively, XANES and EXAFS regions are marked [19].

EXAFS equation. The EXAFS region lies well above the absorption edge. The EXAFS function, $\chi(E)$, of oscillations in this energy regime is empirically defined in terms of the absorption coefficient $\mu(E)$ as [20]:

$$\chi(E) = \frac{\mu(E) - \mu_0(E)}{\Delta\mu_0(E)} \tag{2.10}$$

where:

$\mu(E)$ - measured absorption coefficient at the photon energy E
$\mu_0(E)$ - estimated absorption coefficient of the free atom (background)
$\Delta\mu_0(E)$ - measured jump in the absorption at the threshold energy E_0

It is more convenient to represent the EXAFS function, $\chi(k)$, as a function of photo-electron wave vector, k and in units of $Å^{-1}$, rather than as a function of photo-electron energy, E, such that:

$$k = \sqrt{\frac{2m(E - E_0)}{\hbar^2}} \tag{2.11}$$

The EXAFS theory fundamentally derives from the wave nature of photoelectrons. According to quantum theory these photo-electrons are represented as outward propagating spherical waves centred at the excited atoms. The outgoing photo-electrons of the absorbing atom interact with neighbouring atoms (also called backscattering atoms) leading to scattering, and subsequently alternating constructive and destructive interference of the outgoing and backscattered waves. The amount of interference naturally depends on the amplitude and phase of the backscattered waves. The constructive interference occurs when the outgoing and the backscatter wave are fully in phase. At the same time, if the initial and scattered waves are totally out of phase, a destructive interference takes place. The amplitude of the backscatter wave varies depending on the type (atomic number *Z*) and location (distance from the absorber) of the backscattering atoms. This implies that EXAFS is an element specific method and provides local atomic environment around an absorbing atom. The graphical interpretation of interference of a wave function from absorbing and neighbouring atoms is described in Figure 2.11.

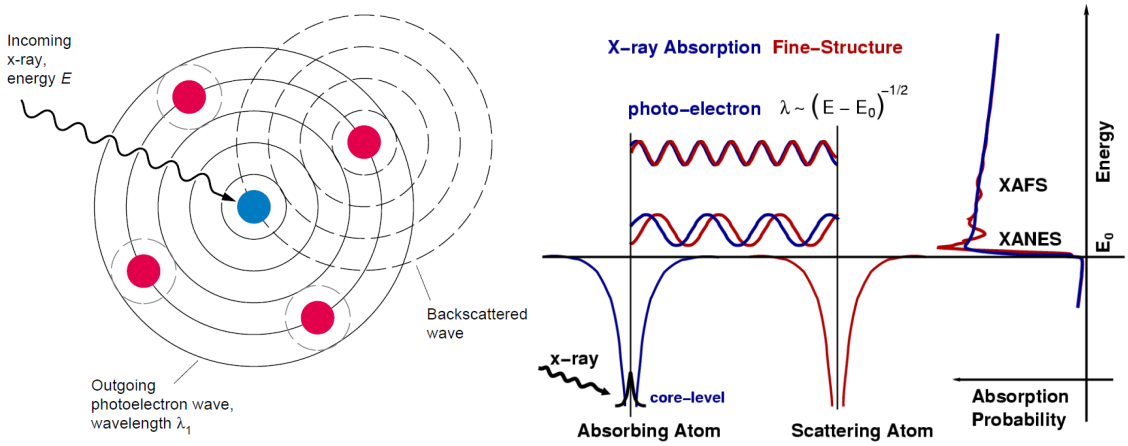

Figure 2.11: Graphical interpretations of spherical waves and XAFS interference in a multi-atom system. The wave function created by absorbing photoelectron (solid line) can backscatter (dashed lines) to the absorbing atom (blue) from neighbour atoms (red). Depending on the phases a constructive or destructive interference occurs [19,20].

In EXAFS theory the simplest derivation of the EXAFS equation is based on the single scattering plane-wave approximation. In essence, it is assumed that due to large kinetic energy in the EXAFS region, the photoelectron scatters only once when it leaves the

absorbing atom. In addition, for a real measurement even for atoms of the same type, it is essential to consider averaging over millions of pairs of atoms to describe the EXAFS equations. The physical description of EXAFS equation in a final function of $\chi(k)$ can be written in terms of a sum of the contributions from all scattering paths of the photoelectron as:

$$\chi(k) = \sum_{i=1}^{n(nr.shells)} A_i(k) \cdot \sin \Phi_i(k) \tag{2.12}$$

As can be seen from this equation the standard EXAFS expression consists of two parts. The first term, $A(k)$, represents the amplitude of backscattering shells and the second component, the sine wave, accounts for the phase shifts as well as the oscillations seen in EXAFS. The function $\sin\Phi(k)$ can be described in terms of the parameter R [inter-atomic distance between absorbing and neighbouring atoms] with a phase given by $2kR$, and the additional phase shift $\phi(k)$ of the photo-electrons as:

$$\sin \Phi_i(k) = \sin(2kR_i - \phi_i(k)) \tag{2.13}$$

The amplitude part in the $\chi(k)$ equation (Eq. 2.12) of each wave contains the coordination number, i.e. the number of atoms in each shell (CN_i), σ_i^2-fluctuation in R_i dimension due to the thermal motion or structural disorder (also known as Debye-Waller factor), S_0^2 - amplitude reduction factor, $F_i(k)$ - the backscattering amplitude, and $\lambda(k)$ which is the mean free path of the photoelectron. The standard expression for $A_i(k)$ is given by [20]:

$$A_i(k) = \frac{CN_i S_0^2 |F_i(k)|}{k_i R_i^2} e^{-\frac{2R_i}{\lambda(k)} - 2k^2\sigma_i^2} \tag{2.14}$$

Introducing the parameters from Eqs. (2.13) and (2.14), the standard EXAFS equation of 2.12 can be written as:

$$\chi(k) = \sum_{i}^{n} \frac{CN_i S_0^2 |F_i(k)|}{k_i R_i^2} e^{-\frac{2R_i}{\lambda(k)} - 2k^2\sigma_i^2} \sin(2kR_i - \phi_i(k)) \tag{2.15}$$

In 1971 Sayers *et al*. [21] demonstrated that the Fourier Transform (FT) could be successfully used to analyze $\chi(k)$ to obtain the Radial Distribution Function (RDF). The Fourier transformation is defined as [22]:

$$\mathrm{FT(R)} = \frac{1}{\sqrt{2\pi}} \int_{k_{\min}}^{k_{\max}} k^n \chi(k) e^{i2kR} dk \tag{2.16}$$

The FT can be used to distinguish different type of neighbouring atoms (due to the different atomic number, *Z*) and isolate individual shell's contribution. An atom with small *Z* number will scatter mainly at smaller *k*-values, while heavier one at higher *k*-values.

There are several tests and factors to assess the quality of a potential model for EXAFS data analysis. The first estimation of how the model agrees with the experimental data can be done by using the $\Re$-factor value, derived from the data analysis. When the difference between model and experimentally collected data is equal to say 1%, the $\Re$-factor = 0.01 [23]. The mathematical expression describing the $\Re$-factor is given by [23]:

$$\Re = \frac{\sum_i |\chi^c(R_i) - \chi^e(R_i)|^2}{\sum_i \left(\chi^e(R_i)\right)^2} \tag{2.17}$$

2.5 References

1 C. Delafoy and P. Dewes, AREVA NP New UO_2 Fuel Development and Qualification for LWRs Applications, 2006 International LWR Fuel Performance Meeting, Salamanca, Spain, 2006.

2 Cardinaels *et al.*, *Chromia doped UO_2 fuel: Investigation of the lattice parameter*. Nucl. Mater. 424 (2012) 252-260.

3 Ch. Riglet-Martial *et al.*, *Thermodynamics of Chromium in UO_2 Fuel: a Solubility Model*, J. Nucl. Mater. 447 (2014) 63-72.

4 A. Leenaers *et al.*, *On the solubility of chromium sesquioxide in uranium dioxide fuel*, J. Nucl. Mater. 317 (2003) 62-68.

5 Ch. Delafoy, *Personal communication*.

6 L. Bourgeois *et al.*, *Factors governing microstructure development of Cr_2O_3-doped UO_2 during sintering*, J. Nucl. Mater., 297 (2001) 313-326.

7 C. Degueldre *et al.*, *Plutonium–uranium mixed oxide characterization by coupling micro-X-ray diffraction and absorption investigations*, J. Nucl. Mater. 416 (2011) 142-150.

8 C. Mieszczynski *et al.*, *Investigation of irradiated uranium-plutonium mixed oxide fuel by synchrotron based micro X-ray diffraction*, Prog. Nucl. Energy 57 (2012) 130-137.

9 W. De Nolf and K. Janssens, *Micro X-ray diffraction and fluorescence tomography for the study of multilayered automotive paints*, Surf. Interface Anal. 42 (2010) 411-418.

10 A. P. Hammersley *et al.*, *Calibration and correction of spatial distortions in 2D detector systems*, Nucl. Instrum. Meth. A346 (1994) 312-321.

11 http://www.crystalimpact.com/match.

12 P. Brouwer, *Theory of XRF*, PANalytical BV (2003).

13 A.C. Thompson *et al.*, *X-ray data booklet*, LBNL (2011).

14 M. Laue, *Eine quantitative Prüfung der Theorie für die Interferenz-Erscheinungen bei Röntgenstrahlen*, Sitz.ber. Bayer. Akad.Wiss., (1912) 363–373.

15 W. Friedrich and P. Knipping, Sitz.ber. Bayer. Akad.Wiss., (1912) 311–322.

16 C. Hammond, *The Basis of Crystallography and Diffraction*, Oxford Sci. Publ. (2009).

17 W. L. Bragg, *The diffraction of short electromagnetic waves by a crystal*, Proc. Camb. Phil. Soc, 17 (1913) 43–57.

18 M. L. de Broigle, *Recherches sur la théorie des quanta*, Ann. de Physique 10, 3 (1925).

19 S.D. Conradson, *XAFS-A Technique to Probe Local Structure*, Los Alamos Science 26 (2000).

20 M. Newville, *Fundamentals of XAFS*, Consortium for Advanced Radiation Sources, University of Chicago (2004).

21 D.E Seyers *et al.*, *New Technique for Investigating Noncrystalline Structures: Fourier Analysis of the Extended X-Ray—Absorption Fine Structure*, Phys. Rev Lett. 27 (1971) 1204-1207.

22 D.C Koningsberger *et al.*, *XAFS spectroscopy; fundamental principles and data analysis*, Top. Catal. 10 (2000) 143-155.

23 E.A Stern *et al.*, *The UWXAFS analysis package: philosophy and details*, D., Physica B, 208&209 (1995) 117-120.

Chapter 3: Uranium Dioxide μ-XRD Investigations

Microstructural changes in a set of commercial grade UO_2 fuel samples have been investigated using synchrotron based micro-focused X-ray fluorescence (μ-XRF) and X-ray diffraction (μ-XRD) techniques. The experimental results are associated with standard UO_2, relatively larger grain chromia-doped UO_2 and $(U,Pu)O_2$ MOX fuels, both fresh and irradiated materials. Further details of analyzed fuel samples are mentioned in Table 2.1.

The lattice parameters of UO_2 in fresh and irradiated specimens have been measured and compared with theoretical calculations. In the pristine state, the doped fuel has a somewhat smaller lattice parameter than the standard UO_2 as a result of chromia doping. There is an increase in micro-strain and lattice parameter in irradiated materials. All irradiated samples behave in a similar manner with an UO_2 lattice expansion occurring during irradiation, where any additional Cr induced effect is obviously insignificant and accumulated damage induced lattice defects prevail. Elastic strain energy densities in the irradiated fuels are also evaluated based on the UO_2 crystal lattice strain and non-uniform strain. The μ-XRD patterns further allow the evaluation of the crystalline domain size and sub-grain formation at different locations of the irradiated UO_2 pellets.

3.1 Lattice parameters measurements

Representative single spot μ-XRD images collected from a Cr_2O_3-doped UO_2 sample are shown in Figure 3.1. It is evident that diffracted beams form arrays of spots lying on concentric circular curves. Several diffraction lines corresponding to (111), (200), (220), (311), (222) and (400) patterns are observed from all fuel samples. In general, two features can be distinguished from the recorded diffraction patterns; fine circular spots and streaking of spots. Beside these two types of reflections, a couple of other weak reflections and features which vary substantially over the scanned area in irradiated samples, are observed but have not yet been fully analysed in the frame of this project.

The pristine Cr_2O_3-doped UO_2 sample exhibits strong single reflections (Figure 3.1a) indicating the presence of large single crystallites. However, the irradiated material has undergone strong crystalline changes. The phenomenon of the Laue spots transforming to partial ring like structure implies that UO_2 grains are changed as a result of irradiation effects. Figure 3.1b and Figure 3.1c demonstrate this process. The irradiation effects are more pronounced in the rim sample. In the centre (Figure 3.1b) of the irradiated pellet the smaller burn-up and higher temperatures have limited the damage. In the periphery of the same pellet larger burn-up and decreasing temperature have increased the damage. These points will be discussed later in this section.

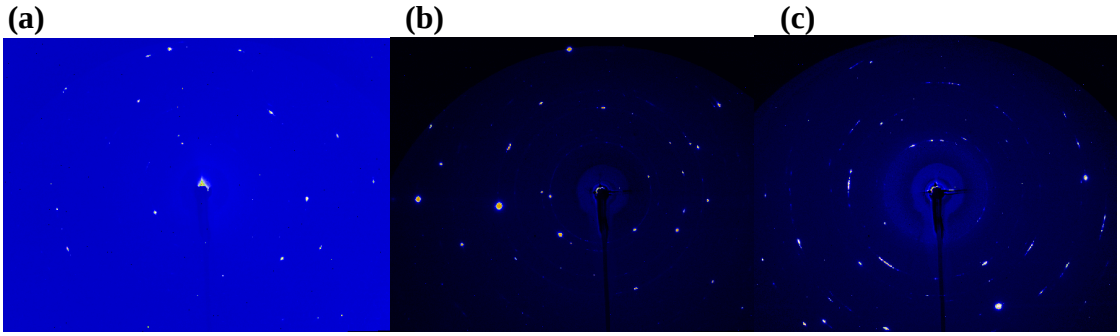

Figure 3.1: Typical 2D μ-XRD images captured (3s exposure) by a CCD camera from chromia-doped UO_2. (a) Pristine fuel; (b) centre region of the irradiated pellet; (c) periphery area of the irradiated pellet.

As already described, Cr_2O_3 doping of UO_2 facilitates pellet densification and fuel grain size growth during sintering [1] compared to standard UO_2 pellets. Therefore, it is of high interest to analyze the details of changes in atomic distances in chromia doped UO_2. To clarify the microscopic mechanism of this restructuring behaviour, determination of accurate and precise lattice constants and densities are required. To obtain quantitative information on UO_2 lattice parameter, μ-XRD data at a lower *d*-spacing (~ 1.65 Å) representing the (311) reflection has been analyzed in detail using the XRDUA [2] computer program. A Gaussian function is chosen as the X-ray diffraction peak profile in this study. Background intensity is subtracted before peak fitting. The residuals peak-fitting procedure provides an interactive peak-fitting process until a minimum residual between fitted and experimental curve is reached. Then, the 2θ position of the (311) reflex is determined from the fitting process. From the measured diffraction line position the lattice parameter, *a*, is obtained using the following relations (3.1) and (3.2):

$$d_{hkl} = \frac{\lambda}{2\sin\theta_{hkl}} \quad (3.1)$$

$$d_{hkl} = \frac{a}{\sqrt{(h^2 + k^2 + l^2)}} \quad (3.2)$$

where Eq. (3.1) represents Bragg's formula, d is the distance between parallel planes of the crystal lattice defined by indices (hkl) and, θ both the angle of incidence and emergence from the scattering planes, for total deviation it is 2θ. For cubic materials, d_{hkl} is related to the lattice constant of the crystal, a, by Eq. (3.2).

3.1.1 Fresh uranium dioxide

Figure 3.2 shows a portion of the experimental μ-XRD patterns, the (311) diffraction peaks profile and the results of lattice parameters for the two UO_2 fresh fuel pellets (sample 1 and sample 2). The experimental lattice parameter of standard UO_2 has been reported in the literature. The value is 5.47065 Å for stoichiometric UO_2 [1]. However, this value of lattice constant is not absolute and believed to vary between 5.468 and 5.472 Å due to slightly different preparation conditions [3,4].

The lattice parameters of cation doped solid solutions are usually calculated using Vegard's law [5]. This law states that, in the absence of strong electronic effects, the variation of lattice parameters is linear with composition in the region where complete solid solutions are established. However, it is known that the deviation from Vegard's law is expected even for thermodynamically ideal solutions when there is a significant difference in lattice parameters of the pure components (e.g., Cr_2O_3 and UO_2 as in the present case). Also, the solid solutions may exhibit a more complex nonlinear behaviour due to several physical factors affecting the host crystal structure, such as the relative atomic sizes of the elements and electrochemical differences between the elements. Therefore, for the chromia doped UO_2, empirical equations are useful for estimating lattice parameters of UO_2 solid solution to predict the effect of chromium. In this respect, the lattice parameter of UO_2 doped with 0.16 wt.% chromia has been calculated using the formalism as suggested by Kim [6]. Knowing the pure UO_2 lattice constant as 5.47065 Å,

the equation for the lattice constant $a_{(UO_{2\pm x},k)}$ of UO_2 solid solution with dopants can be formulated as [6]:

$$a_{(UO_{2\pm x},k)} = 5.47065 + \sum_k \left(0.206 \cdot \Delta r_k + 0.0013 \cdot \Delta z_k\right) m_k \qquad (3.3)$$

where Δr_k ($r_{dopant} - r_{host}$) represents the difference in ionic radius (in Å unit) of the k^{th} dopant and host cation uranium, and Δz_k ($z_{dopant} - z_{host}$) is the corresponding difference in charge. The notation m_k denotes mole percent of the k^{th} dopant which is further represented by [6]:

$$m_k = \frac{n_k M_k}{100 + \sum_k (n_k - 1) M_k} \cdot 100 \qquad (3.4)$$

Here, n_k is the number of cations in the solute oxide and M_k is the mole percent of the k^{th} dopant oxide [6]. Considering that chromium maintains its 3+ charge within UO_2 and complete solid solutions are established, this calculation using Esq. (3.3) through (3.4) yields a lattice parameter of 5.46715 Å for 0.16 wt.% Cr_2O_3 and $r_{Cr^{3+}}$: 0.72 **Å** (as estimated for coordination number CN=8) in fresh UO_2 . Thus, addition of chromium into UO_2 results in a slight contraction of the cubic fluorite lattice by ~ 3×10^{-3} Å (Δa value compared with standard UO_2). The calculated lattice parameter values are shown in Figure 3.2c.

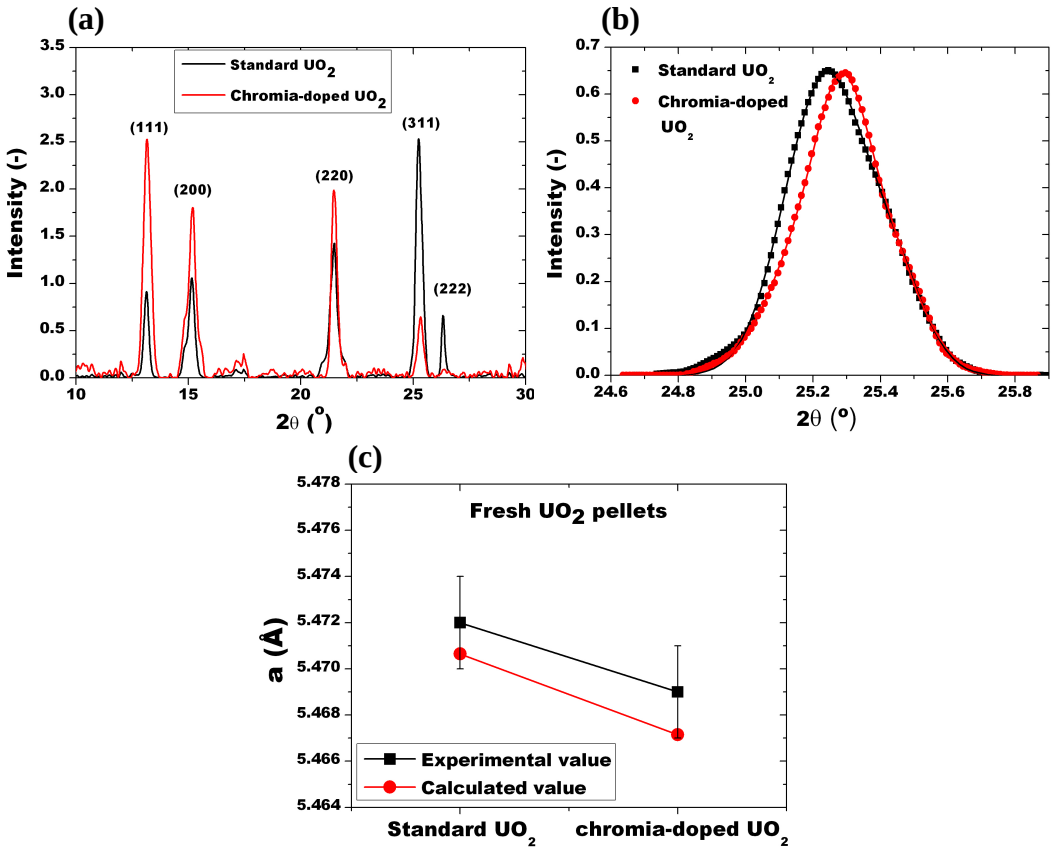

Figure 3.2: (a) Micro-XRD spectra for pristine UO_2 samples (both standard and chromia-doped); (b) experimental (311)-diffraction lines between 2θ values of 24.6° and 25.9° together with fitted curves and; (c) comparison of experimental lattice constants derived from (311)-reflections and *a* values calculated using the empirical equation [6] for a Cr dopant in UO_2. Data are shown using symbols and the solid lines are to guide the eye.

Comparing the μ-XRD data for standard UO_2 with the chromia doped sample in Figure 3.2b and the results presented in Figure 3.2c it is clear that the diffraction lines profile are almost similar, and the doped fuel has a smaller lattice constant than the standard fuel. For the (311) lines of standard and doped UO_2, a full width at half maximum of 2θ = 0.325° and 0.292°, respectively, are measured. The lattice parameters are found to be 5.472 and 5.469 Å for undoped and doped UO_2, respectively. The lattice contraction is 0.003 Å. These results on UO_2 unit cell lattice parameter obtained for fresh undoped and chromia doped specimens are consistent with literature values. A similar effect of Cr in UO_2 has been recently described in Ref. [7]. In the literature, both substitutional model and/or location of trivalent Cr at the interstitial sites in UO_2 have been discussed [1,3,7]. The defects formed in UO_2 due to the added chromium can exist as isolated point defects at low concentrations, but aggregate into clusters at higher concentrations, depending on

defect structures. Previous studies have also accounted for the formation of an O^- lattice or interstitial species to achieve partial electrical neutrality, but these were found to be uncompetitive compared to the O^{2-} mechanism [8]. Nevertheless, it is still not enough to give a clear image of the lattice structure of Cr incorporated UO_2. The occurrence of short range order of oxygen ions and vacancies may be confirmed experimentally through an X-ray absorption fine structure (XAFS) study measuring the first neighbour bond distances and CN's for Cr and U ions in doped UO_2 material. These results would help to describe details of the physical structure of the chromia doped UO_2 lattice. In Chapter 4, we will present the XAS results on the lattice location of Cr in UO_2 lattice. In the following, the lattice parameters of UO_2 fuel materials before and after irradiation are compared.

3.1.2 Irradiated standard and Cr_2O_3-doped uranium dioxide

From the irradiated fuel pellets, sub-samples were prepared and analyzed by μ–XRF to locate the irradiated UO_2 particles. Subsequently, high resolution small-area μ-XRD scans were performed. An example of a comparatively larger-area μ-XRF map together with the reconstructed μ-XRD scan, measured at a selected location on sample 3 (IC) is represented in Figure 3.3. The irradiated fuel particle has a size of about 40 μm × 40 μm comprising 3 to 5 adjacent UO_2 grains which complies with the average grain size of ~ 10 μm UO_2 microstructure. It is important to note here that although the μ-XRF technique could be successfully applied to detect those fuel particles, the lateral resolution is not high enough to distinguish UO_2 grains from other grains and grain-boundaries. Anyhow, the fuel particle illustrated in Figure 3.3 is scanned with the X-ray beam in 6-μm steps. Representative 1D intensity plots over the 2θ interval from 10^o to 30^o from two different positions within the fuel grains are also illustrated in the figure. The power of this micro-diffraction technique can be clearly seen where the intensity variation of several reflections can be remarked. It demonstrates that the diffraction spectra are not similar, both in terms of line shape and integrated intensity. For example, note the relative intensity variation between (311) and (222) peaks and line profile of (220)-reflection in Figure 3.3. The broadening effect is also strong enough to be considered by visual inspection. In general, the sub-structure of the irradiated crystallites gives wide poorly

shaped additional spots (see Figure 3.1b). Other features include smearing of intensity and elongated Laue spots showing sometimes curved streaks around the spots (see Figure 3.1c), yielding some imperfect structure in these samples. The observed changes are related to several effects such as the spatial distribution of the irradiated UO_2 crystallites within the investigated fuel particle, change in distribution and variance of the local orientation inside a single damaged and stressed grain, difference in local (micro- to nano-)strains and strain gradients inside crystallites due to the cation disorder and/or the presence of any non-stoichiometric oxygen, UO_2 grain-subdivision also called polygonization, and other structural disorder originating from irradiation effects in UO_2 lattices. Streaking in micro-Laue patterns due to inhomogeneity in dislocation density and/or elastic stresses is common and has been observed in deformed materials. Further discussion on these aspects is beyond the scope of this work. It is important to also mention that some complexity may arise from the overlap of Laue patterns which can be attributed to each grain and that the multiple grains may have been illuminated more or less in some of the CCD images due to the penetration of X-rays and therefore sampling depth in broken grains. In a future work, we shall highlight these points and capabilities of scanning μ-XRD resolving depth information of diffracting UO_2 grains. It would require a depth resolve method and data analysis using computer aided software tools [9].

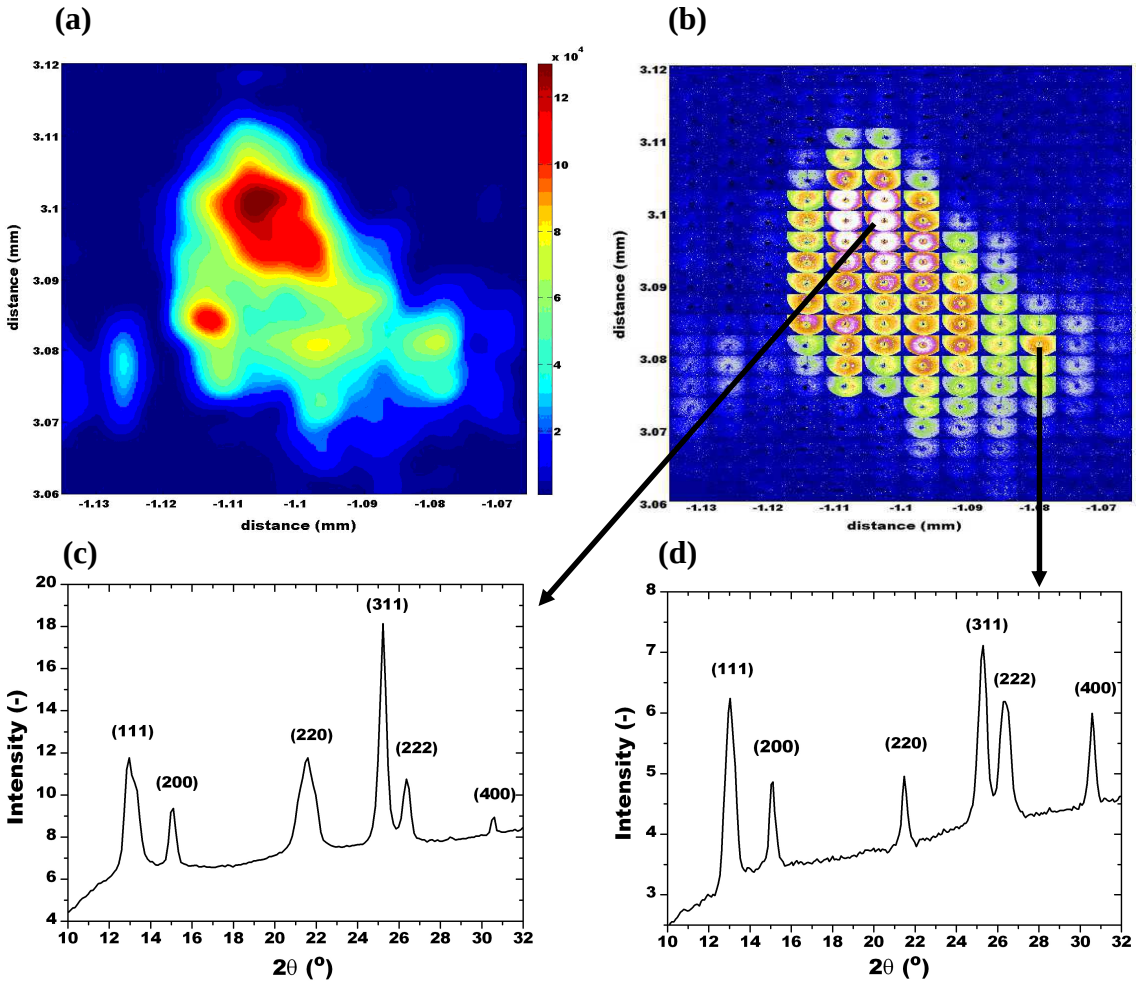

Figure 3.3: (a) Uranium μ-XRF map of an irradiated fuel particle (scan size 70 μm × 60 μm). (b) Reconstructed 2D μ-XRD map of the fuel particle shown in (a). In (c) and (d) integrated 1D diffraction spectra from two different fixed locations (marked as arrowed lines) within the sampling area are shown. See the text for other details.

The specific microstructural information that can be studied from our recorded μ-XRD data of irradiated fuel particles is sample dependent to some extent, in particular, particle size dependent. If the UO_2 grain size is of similar dimensions or greater than the incident X-ray beam, grain specific crystal phase composition/homogeneity and other micro-structural information can be measured. If the grain size is less than the focused X-ray spot size, average crystal structure information relating to the phase, grain size, macroscopic deformation and stress/strain relationships can be detected. In the later case it also provides a better crystallite statistics and improves the statistical relevance of the results. In the following, the results of lattice parameter are presented for irradiated UO_2 materials. The analysis is based on the average of about 225 CCD images (~ 100 μm ×

100 μm examined area; 6 μm step size, 1s exposure) captured from each irradiated particle examined. This procedure has been applied only for the lattice parameter determination of UO_2 in irradiated fuels. In a similar way as of fresh UO_2 pellets, the (311) diffraction line for irradiated fuels is analyzed. The specimens examined are sample 3 (IC and IR) and sample 4 (IC and IR). Portion of the experimental μ-XRD spectra and the variation of experimental lattice constants are shown in Figure 3.4. The measured lattice parameters are listed in Table 3.1. The calculated $a_{(UO_{2\pm x},FPs)}$ values reported in Table 3.1 are obtained by the substitution of aliovalent and isovalent cations of fission products in solid solution for the host U^{4+} cation in UO_2. We will discuss this point later in this section.

Table 3.1: Experimental and calculated UO_2 unit cell lattice parameters for the standard and chromia-doped fuel samples. Results are shown for fresh and irradiated materials. Note the calculation values for irradiated fuel are conservative considering Cs, Xe, Rb and Kr as partially dissolved in the fuel (see text); calculations with data from Table 3.2.

Fuel type/region		**Lattice constant**	
		Experimental value (± 2.0×10^{-3}) (Å)	**Calculated value (Å)**
Standard UO_2	fresh fuel (NI)	5.472	5.47065 (from literature)
	Irradiated centre (IC)	5.482	5.47449
	Irradiated rim (IR)	5.483	5.47567
Chromia-doped UO_2	fresh fuel (NI)	5.469	5.46715
	Irradiated centre (IC)	5.482	5.47099
	Irradiated rim (IR)	5.485	5.47217
$(Pu,U)O_2$	fresh fuel (NI)	5.454	5.468
	Irradiated center (IC)	5.487	5.469
	Irradiated rim (IR)	5.456	5.468

It has been observed that the diffracted peaks position of the (311) plane decreases towards lower 2θ values for all irradiated UO_2 samples. This result indicates an increase of the lattice spacing in the irradiated compared to fresh fuel. Within the measured uncertainty limits, a slight variation in the lattice spacing of the (311) planes also exists between the centre (IC) and rim (IR) regions of the studied samples (see Figure 3.4 and Table 3.1). For the standard UO_2, the average lattice constant is increased to calculated 5.483 Å which is very close to the lattice constant of the irradiated chromia doped sample from our measurement, 5.485 Å with ~ 0.03% accuracy. Comparing these values with those of fresh UO_2, one can notice that the difference in lattice parameters is significant and vary between 11-16 × 10^{-3} Å (~ 0.22%, an average value) for both the standard and

chromia-doped samples. Notably, the structural lattice modifications and change in lattice parameter in these two different materials (undoped and doped UO_2) are similar. The differences noted in the lattice parameters are associated to the atomic scale structural alteration of UO_2 caused by the irradiation effects. Since under irradiation these fuels undergo a number of micro-structural and compositional changes depending on local burn-up as well as temperature experienced in the pellet, here we are interested primarily in those changes most likely influencing the lattice structures.

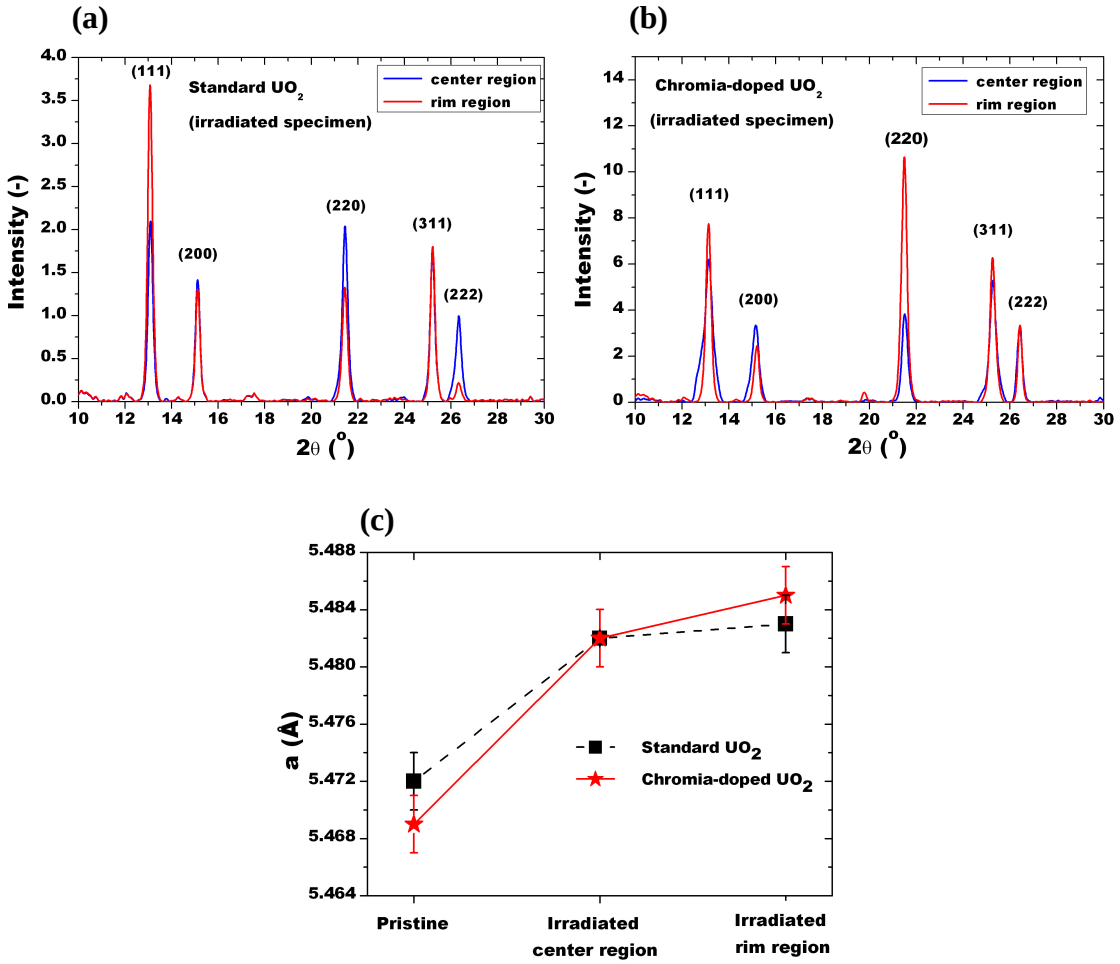

Figure 3.4: Comparison of experimental μ-XRD intensity plots and measured lattice parameter values for irradiated materials: (a) standard UO_2 and (b) chromia-doped UO_2. In (c) the burn-up increases from left to right and solid as well as dashed lines connecting data points are to guide the eye.

Incorporation of fission products in UO_2 lattice. During the fission process a wide range of solid and gaseous fission product (FP) atoms are generated from fissile uranium. They disturb the cation-cation and cation-anion network of the host UO_2 lattice. The

formation of FPs together with other activation products leads to a doping of the lattice depending on their solubility limit and chemical affinity in UO_{2+x}. Complex inter-metallic and other oxide precipitates involving FPs, Pu, U and O atoms are also formed which is controlled by the temperature (diffusion), fission yield of elements and oxygen potential of the fuel. The gaseous FP atoms such as Kr and Xe are reported to be practically insoluble in UO_2 [10]. As a consequence, the fission gas atoms at a lower yield may be trapped at defect sites in the UO_2 lattice. At higher concentrations they always form bubbles, move and accumulate at the grain boundaries, and the final release along this pathway to the free volume of the fuel rod.

Over the past decades many experimental tests and theoretical calculations have been carried out for interpretation and understanding the complex fission products behaviour in nuclear fuels. There are also many codes developed worldwide in order to model FP behaviour and impact in irradiated nuclear fuels (e.g. ORIGEN, FALCON, ANGE, TRANSURANUS etc.). Post irradiation examination on irradiated UO_2 has revealed that in the matrix fluorite phase some of the actinides and rare earth elements are incorporated as solid solutions. A part of Sr, Ba and Zr compounds is also soluble in this phase. This is in agreement with theoretical calculations [11] on solution energies of fission products in predicting their site occupancy in UO_{2+x}, although the extent of solubility critically depends on the oxygen to metal ratio in the fuel. The fission product oxides whose cations are closer in size to the U^{4+} are the most soluble. Larger FP cations belonging to the alkali metal group such as Cs require a large positive incorporation energy in UO_2 when trap sites are equivalently available for occupations in the lattice, and therefore, incorporation is energetically less favourable [12]. At the same time iodine, whose fission yield is roughly one order of magnitude smaller than that of Cs, can form CsI that is insoluble in UO_{2+x} [13]. Transition metal ions of Ru, Pd, Rh, Tc etc. are known to be resistant to oxidation and always precipitate out of solution in a more stable secondary phase as metallic inclusions in the fuel.

In the following, an analysis of lattice parameter evolution for the accommodation of FPs in uranium dioxide is presented. It should be mentioned that the theoretical analyses are done only for irradiated chromia-doped UO_2 and MOX fuels. Since the average burn up

in irradiated pellets of standard and chromia-doped UO_2 was comparable, the lattice constant calculations were not taken up for the irradiated standard UO_2 fuel.

In the analysis, inert gas species Kr and Xe are predicted to be insoluble [14], and influence on UO_2 lattice parameters of some FPs (e.g. Br and I) which are possibly stable as anions in UO_{2+x} is disregarded. In a simplified approach only cations of rare earth elements and other FPs mentioned before, which may be introduced as dissolved atoms into uranium dioxide fluorite structure, have been considered. Regarding Cs there have been a number of attempts to understand its behaviour as a dissolved cation in UO_2. Earlier Kleykamp [15] has reported that no thermodynamic equilibrium can be attained between Cs_2O and UO_2 in the annealing experiment at 1000°C. The results of electron probe micro analysis (EPMA) measurements in several transient-tested fuels have shown a very low solubility of Cs in UO_2 (less than 0.06 wt% at temperatures between 1700 and 1950°C [16]). In this work, therefore, any Cs influence on UO_2 lattice parameter for irradiated materials could be neglected. This assumption could be supported by the size factor rule described by Hume-Rothery [17] that solubility is limited if the size of the solute ion differs from that of the host ion by more than 15%. The radius of the U^{4+} ion in the cubic structure (coordination number 8) is 1.00 Å whereas the ionic radius of the Cs^+ ion varies from 1.67 (coordination number 6) to 1.88 Å (coordination number 12) [18].

Table 3.2: Fuel elemental fractions, ionic radius of U, Pu and FP atoms considered in Eq. 3.3. The analysis is shown for the irradiated chromia-doped UO_2. Note: * Cs^+ and Rb^+ estimated solubility.

Cation	Ionic radius (Å)	Centre region (wt.%)	Rim area (wt.%)
U^{4+}	1.00	86	80
Pu^{4+}	0.96	0.85	2
Sm^{3+}	1.079	0.1	0.2
Pm^{3+}	1.093	0.005	0.01
Nd^{3+}	1.109	0.35	0.5
Pr^{3+}	1.126	0.1	0.2
Ce^{3+}	1.143	0.2	0.4
La^{3+}	1.160	0.1	0.2
Ba^{2+}	1.420	0.1	0.2
Cs^+	1.740	0.06*	0.06*
Nb^{4+}	0.790	0.005	0.01
Zr^{4+}	0.840	0.35	0.5
Y^{3+}	1.090	0.05	0.15
Sr^{2+}	1.260	0.05	0.15
Rb^+	1.610	0.06*	0.06*

In Table 3.2 average elemental concentrations of several FP elements for the irradiated chromia-doped UO_2 sample are shown. The irradiated pellet had a local burn-up of ~ 3.1% and 7.5% FIMA (fission per initial metal atom) in the centre and periphery regions, respectively. The quantitative data on elemental fraction in Table 3.2 are obtained from EPMA studies on the radial distributions of FPs measured on this irradiated doped fuel pellet. Additional data of a few selective FP elements that we have not measured by EPMA are estimated from expected fission yield histograms for a given burn-up as found in Ref. [11]. Values of ionic radii are taken from Shannon's table [18]. The maximum solubility of selective FPs, such as Zr, Ba and Sr that have shown only a limited solubility in UO_2 and $(U,Pu)O_2$, are estimated from solubility data available in the literature [19]. Lattice parameter changes are calculated on the basis of their ionic radii and valence states. These two factors, size and their charge difference with the host uranium determine whether additive cations will either contract or expand the initial UO_2 unit cell. It should be noted, however, that the calculations do not include the UO_2 lattice dilatation due to defect formation by α-particles self-radiation and/or other irradiation induced defects that have occurred in this irradiated pellet. It is also presumed that fission products do not interact with each other.

From Eq. (3.3) and (3.4) the UO_2 lattice parameter is calculated where $a_{(UO_{2\pm x},FPs)}$ (see calculated values in Table 3.2 represents the lattice parameter of uranium dioxide comprising soluble fission products in solid solution. Our analysis shows that the cations with larger ionic radius (e.g., La, Ba, Cs etc. see Table 3.2) tend to increase the lattice spacing of UO_2 and those with smaller ionic radius decrease the spacing. The net effect depends on the concentrations and valences of the constituting elements. The component of the lattice parameters that are derived from size compensation of larger cations and those from the lower ones largely balance out and only small variations in the lattice parameters remains. Maximum deviations found between $a_{(UO_{2\pm x},FPs)}$ and the lattice constant of fresh UO_2 are only 3.5×10^{-3} Å and 4.7×10^{-3} Å (~3.8×10^{-3} Å and ~5.0×10^{-3} Å in a very conservative way, considering small amounts of soluble Xe (*r*: 2.2 Å) and Kr (*r*: 2.0 Å) e.g. 0.01 wt%), respectively, for the centre and periphery regions of the doped pellet. Our calculations agree reasonably well with fission product oxides

solubility calculations of Kleykamp [15] and experimental observations by Une *et al.* [20], in which they found that $\Delta a \approx 0.7 \times 10^{-3}$ Å per percent burn-up (FIMA) in irradiated UO_2. All these results imply that substantial quantities of fission products can be accommodated without significant changes in the lattice. Hence, the anticipated change of UO_2 lattice spacing in irradiated fuels due to only successive inclusion of soluble FPs is small (in the range of $1 - 3 \times 10^{-3}$ Å and up to 5×10^{-3} Å in a conservative way), and can not be used alone to explain the enlargement of the lattice constant by 12×10^{-3} Å that we have measured. This discrepancy is related to the accumulated irradiation induced defects and fission gas which have modified the crystal lattice of UO_2 in the irradiated matrix. It is generally accepted that atomic displacements caused by the fission processes, are the most important source of radiation effects in the fuel. Displacements lead to local changes in the microstructure, composition and stoichiometry. Those effects result in the modification of physical properties. For example, the lattice parameter in UO_2 increases as a function of irradiation dose/burn-up and is due to the variation in the population of defects (interstitials and vacancies) and their clusters [21]. It is emphasized that the resulting processes are very complex. Although the lattice expansion measured can not be assigned only to any particular type of defect or phenomenon, interstitial dislocation loops certainly contribute in a significant way [22]. Computational models [8,23] and experimental investigations [24,25] on the nature and stability of defects generated during irradiation in UO_2, on damage formation and recovery, and on the fission products behaviour have shown that a large fraction of the damage can be recovered instantaneously by the temperature effects. This helps to explain the structural stability of UO_2 and the absence of amorphization. However, eventually high concentrations of point defects and extended defects together with fission gas coexist in high burn up UO_2, which thereby expand the crystal lattice as observed.

3.1.3 Irradiated MOX fuel

Typical Laue patterns recorded for $(Pu,U)O_2$ are given in Figure 3.5 for the non-irradiated (NI) as well as irradiated sample for the centre (IC) and rim region (IR). The single peaks

observed in the 2θ range 11°-13°, 13.5°-14.5°, 19.5°-20.5°, 23°-24°and 24°-25°, correspond to the (111), (200), (220), (311) and (222) reflections, respectively.

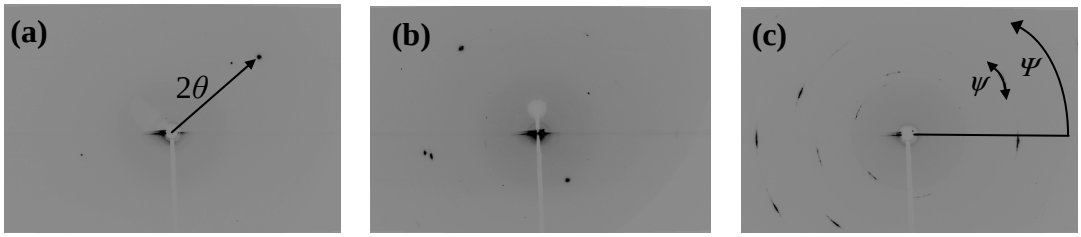

Figure 3.5: Typical patterns obtained for (a) pristine MOX fuel sample 5 (NI), (b) irradiated centre (IC) and (c) irradiated rim (IR). Directions for 2θ angle and for circular position Ψ are noted. Ψ – reflex circular position, ψ – reflex azimuthal width.

All these peaks are fitted using the PeakFit program to reveal the contributions of individual phases to the intensity values of experimentally observed peaks. Due to the decreasing error of measured reflexes with an increase of 2θ angle, the (222) reflex was taken into account. In this work, attempts have also been made to evaluate the lattice parameters in MOX based on the ionic radii of the constituent elements. The empirical formula used to calculate the lattice parameter a (pm) is same as used for the standard and Cr_2O_3-doped fuel comparison (see Eq. 3.3).

In the pristine state, the lattice constant a obtained from Eq. (3.3) was simplified to the terms related to UO_2 and PuO_2. For the irradiated specimens contributions from some of the known FP phases crystallizing in a cubic system (i.e., CeO_2, ZrO_2 and BaO) are taken into account with their molar fraction x as measured by EPMA [26] (see Table 3.2).

In Table 3.1 the lattice parameters obtained from experimental data are compared with those calculated using Eq. 3.3. The ionic radii utilized from Table 3.2 are for the coordination number CN = 8, which corresponds to U^{4+} in UO_2. The results in Table 3.1 reveal that the relative difference between experimental and calculated lattice parameter is about 0.22% in average.

Experimental intensity plots and calculated 2θ values for the (111) reflex are compared in Fig. 3.6 for un-irradiated, irradiated fuel centre and rim. The 2θ shifts between dashed lines and intensity profiles are smaller than the error ($\Delta 2\theta$ = 0.02°). Actually, the determination of lattice parameters needs to be very precise. According to Amaya *et al.* [27], the change of a for 60 MW d kg^{-1} is only 0.2% with a detection limit of 0.08%.

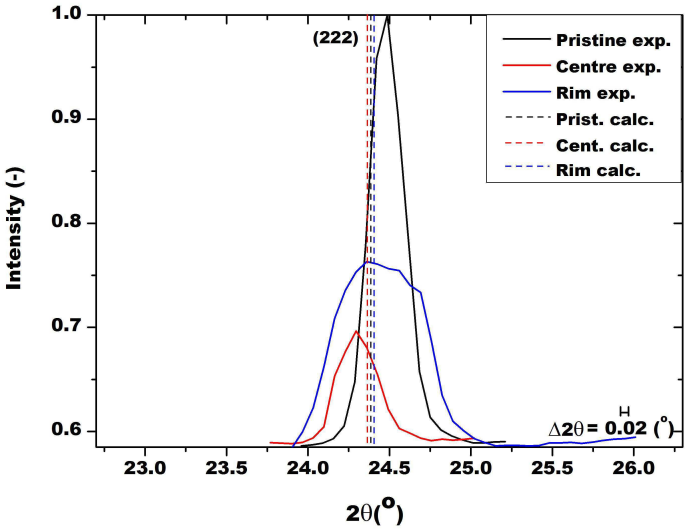

Figure 3.6: Comparing experimental intensity plots and calculated 2θ values for reflex (222) for un-irradiated fuel, irradiated fuel centre (local burn-up ~50 MW d kg^{-1}) and rim (local burn-up ~110 MW d kg^{-1}).

Via 2θ only small *d*-spacing shifts are detected as function of local burn-up. In the case of the (222) reflex the shift goes to slightly higher 2θ values or a smaller lattice spacing (compare Table 3.1,Figure 3.6). A reduction of the lattice spacing with local burn-up can be explained by 2 possibilities:

- fission products are formed and reduce the spacing, see Table 3.1, where lattice constants for fuel with and without fission products are considered;
- stress on the lattice is reduced in a sort of relaxation by sub-grain formation which results in a decrease of the lattice spacing.

The first explanation is endorsed by the calculated influence of the fission products; the second explanation is supported by the fact that the measured lattice constant reduction is stronger than the calculated one. Due to the only slight shifts and the scarce data a final assessment of the importance of the two effects is difficult.

3.2 Strain analysis

As the μ-XRD methods allow examining very small sample areas, it is very suitable for the analysis of grain specific uniform and non-uniform strain in irradiated UO_2. High spatial resolution in scanning μ-XRD determines subtle variations in strain and reveals

differences between crystallites and strain distributions within crystallites. Stress or strain in the irradiated UO_2 is known to cause visible changes in the diffraction patterns due to deviations from original crystallinity [28]. The changes can be observed as diffraction peak asymmetry, peak broadening, and peak shifting. In the following, average strain energies in standard UO_2 and chromia-doped UO_2 are evaluated from μ-XRD results. From single spot consecutive Laue images and corresponding integrated intensity plots we have also attempted to obtain information about strain distributions within irradiated UO_2 crystallites. It requires decoding and separate out contributions of overlapping Laue patterns from (sub)-grain volumes along the incident X-ray beam path. However, these are much more rigorous analysis and have not yet been completed.

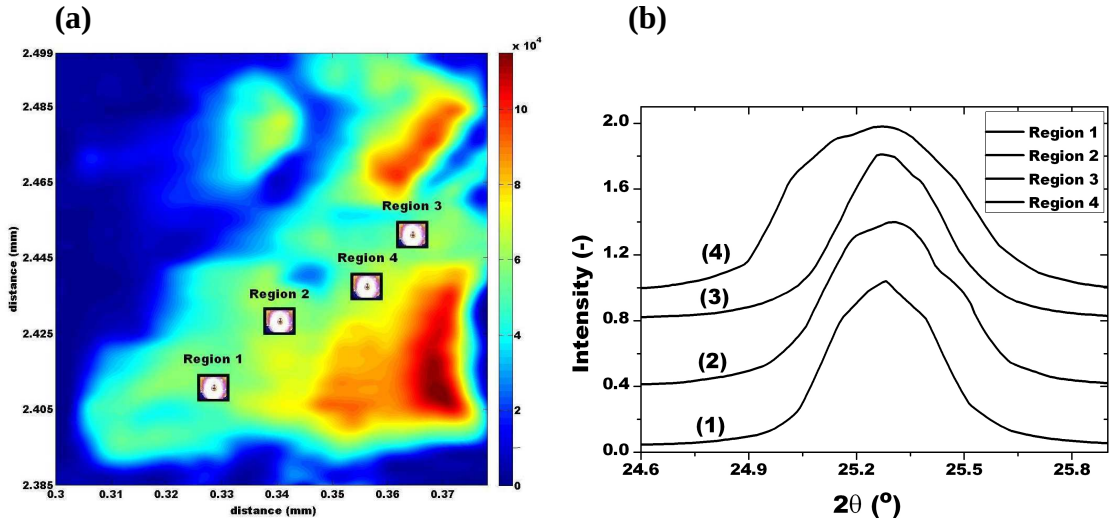

Figure 3.7: (a) Microprobe synchrotron radiation XRF map of uranium from an irradiated chromia doped UO_2 fuel particle taken from the centre region of the pellet (sample 4, IC); scan dimension 80 μm × 115 μm; step size 3.0 μm. (b) plots of intensity versus 2θ for XRD (311) peaks, derived from the integration of respective CCD images taken from different locations in the fuel particle shown in (a). The diffraction curves are vertically shifted with respect to each other for clarity.

It is mentioned earlier that the average grain sizes are about 10 and 50 μm in the standard and chromia-doped UO_2 fresh-fuel, respectively. Therefore, we have selected irradiated fuel particles of similar dimensions in sample 3 and sample 4 for scanning μ-XRD. Due to higher burn- up in the rim area of irradiated pellets and hence complexity in the observed micro-Laue patterns (spot intensity distributions, elongated or diffused spots, large streaking etc., which can no longer be fitted with the Gaussian function to identify the spot centres and/or to estimate widths), only fuel particles from the centre region (IC)

of the irradiated pellets were examined for strain analysis. Careful analysis has been carried out on selected single spot Laue images and the corresponding diffraction line patterns in different regions within the fuel particle. The intensity distributions in μ-XRF maps are used to choose areas that minimized overlapping of different grain orientations and compare two single spot diffraction spectra originating apparently from identical domain volumes.

An example that illustrates combined micro-beam μ-XRF with μ-XRD approach to quantify strain in chromia-doped UO_2 is shown in Figure 3.7. A selected area μ-XRF map of uranium in UO_2 fuel particles collected from the centre region of the irradiated pellet (sample 4, IC) is displayed in the left plot. The mapping remains a non-absolute analysis and gives the spatial distribution of uranium in the viewing region. Also the colour bar counts presented in the image are only meaningful in a relative way. It is evident from Figure 3.7a that the uranium distribution is homogeneous at several regions in the map, but can also be observed at higher concentrations at some locations of the particles as distinct from the surrounding regions. This uranium heterogeneity is associated with the thickness variations in the UO_2 particles within the sampling area. Therefore, single spot μ-XRD spectra are selected from regions where the probed volumes are rather similar to quantify average strain energy in the material. The plot on the right in Figure 3.7 shows four single spot (311) diffraction lines collected from the specified locations labelled in Fig. 3.7a. Note that there is little difference between the diffraction patterns in term of peak angular width, suggesting little difference in the state of irradiated UO_2 crystallites between these zones. All the peak widths are, however, notably broader compared to that is measured for not irradiated UO_2 samples (see Figure 3.2b).

Without discussing here the algorithm in detail, it is preferred to mention the following relations that are required to determine strain energies from experimental diffraction data. The strain energy density, *U*, which is the total strain energy per unit volume of a material and isotropic too, can be approximated by the following relations [27]:

$$U = \frac{3}{2} E \varepsilon_{total}^2 \qquad (3.5)$$

$$\varepsilon_{total} = \varepsilon_c + \sqrt{\frac{2}{\pi}}\varepsilon_{nu} \tag{3.6}$$

where ε_{total} represents the total strain and E is the modulus of elasticity (Young modulus). In this work, uniform crystal strain (ε_c) in irradiated UO_2 crystallites is estimated from the lattice parameter changes in irradiated UO_2 samples with respect to soluble FPs-doped UO_2 at a given burn-up as proposed in Ref. [29]. The non uniform strain or microstrain, (ε_{nu}), occurring between irradiated crystallites, is evaluated by adopting the Williamson-Hall technique [30]:

$$\beta\cos\theta = \frac{\lambda}{D_v} + 4\varepsilon_{nu}\sin\theta \tag{3.7}$$

where β is the peak broadening of a reflection (in radians) located at an angle 2θ, λ is the wavelength of incident X-rays and, D_v is the volume weighted crystallite size. In all analyses, a Gaussian convolution for the experimental peak profiles is assumed.

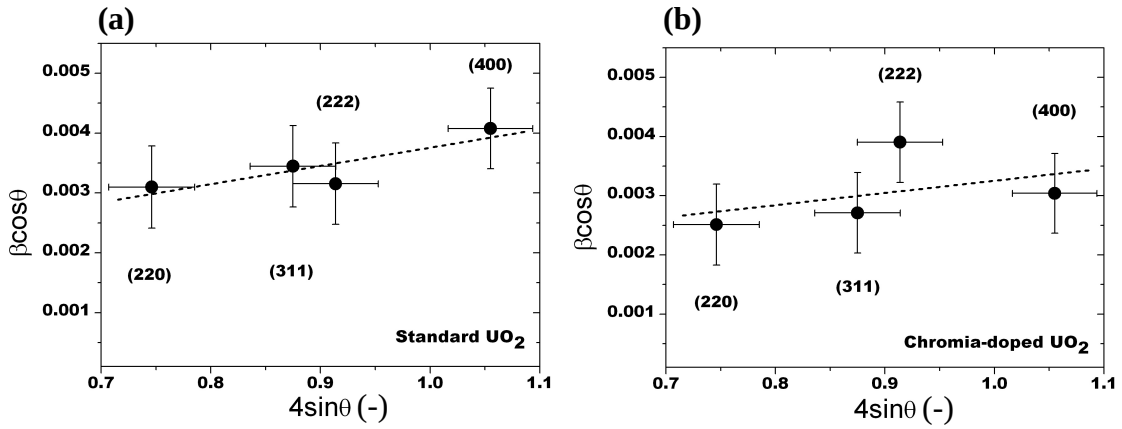

Figure 3.8: Williamson-Hall plot to determine the ε_{nu} value in irradiated crystallites for; (a) standard UO_2, (b) chromia-doped UO_2. The error bars on data points show the standard deviations to the mean responses. The dashed line in each plot shows a linear fit to data points. See text for details.

Figure 3.8 shows Williamson-Hall analyses of the diffraction peak widths from successive orders for standard and chromia-doped irradiated UO_2. The measured FWHM of peaks from irradiated crystallites have been corrected for size and instrumental effects based on the experimental result of the unirradiated UO_2 sample. The slope of the plot between $\beta\cos\theta$ and $4\sin\theta$ in Fig. 3.8b gives the microstrain of $\varepsilon_{nu} = 2.1 \times 10^{-3}$ for the

chromia-doped specimen. The uniform crystal strain (ε_c) is found to be about 3.0×10^{-3} for a local burn-up of ~3.1% FIMA. This results in an accumulated strain energy of U = 6.4 MJ m^{-3} in chromia-doped fuel, when any significant level of Laue pattern streaking and/or change in Laue spot shape in transverse direction is excluded. The uncertainty estimate in the obtained strain energy is ~20%, associated with the linear least square fitting procedure (Figure 3.8). Following a similar analysis for the standard UO_2 (sample 3, IC), we obtain approximately a value of U = 7.1 MJ m^{-3}. This magnitude of strain energy slightly overestimates the result of Amaya *et al*. [31] reported for UO_2 samples irradiated in test reactors at various burn-up. Nevertheless, our results provide a quantitative trend on accumulated strain energies in two samples of standard and chromia-doped UO_2. Relatively, their behaviour is rather similar at the given burn-up. The strain energy is dependent on the irradiation process, the sum properties of the modified strain regions and the strain reactive irradiation induced micro-structures. It is considered that accumulated irradiation defects in terms of dislocations and their motion are the most important mechanisms responsible for strain variation in irradiated UO_2 matrix [27]. If the strain is too large for elastic deformation, grains polygonization allows random dislocation arrays to rearrange to reduce strain energy.

3.3 Laue diffraction from polygonized UO_2 grains

It is known that in the rim at the pellet periphery with a thickness of 50–200 μm at high burn-up the so-called high-burn structure is created. Original UO_2 grains of typically 10 μm in size are subdivided into new smaller grains in the size range of 150 nm down to sub-nm, depending on the local burn-up. At very high burn-up ($\geq$ 75 MW d kg^{-1}) this structure extends deeper into the fuel pellet. The high burn-up or rim structure observed in irradiated UO_2 is apparently the result of different mechanisms: defect accumulation, reorganization of dislocations as precursor for subdivided grains, fracture of grains due to intra-granular bubbles, polygonization and finally possibly temperature induced recrystallization. The schematic drawings for theoretical Laue reflections obtained from ideal and polygonized grain are presented at Figure 3.9. Experimental observations of the UO_2 polygonization have been reported in many publications [32,33].

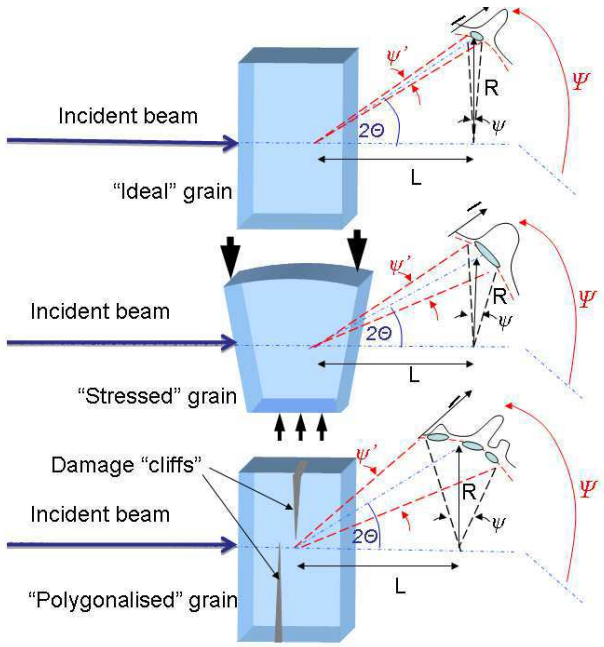

Figure 3.9: Schematic graphs of Laue transmission diffraction. On the top picture – "ideal" grain without stress. In the middle – bent grain deformed due to stresses (broadened peak on the diffraction pattern). On the bottom – grain with sub-grains (peak modulation on the diffraction pattern). Ψ-reflex circular position, ψ-reflex azimuthal width.

Several models are also present in the literature [34,35] to describe the UO_2 grain subdivision mechanism. In the simplest picture, reorganization of dislocations into sub-boundary domains is the main mechanism responsible for the formation of smaller grains. It occurs in the fuel after a certain burn-up (~30 MW d kg^{-1} [36]) forming low angle smaller grains and each newly formed polygon is oriented slightly differently from its neighbours so that the boundaries between them are low angle tilt boundaries.

To illustrate the consequence of UO_2 sub-grains formation on Laue spots shape as well as on intensity distributions, we now return to the experimental Laue images shown in Figure 3.1. The most obvious feature identified in the irradiated samples is the modification of spot shapes in transverse direction. The Laue pattern of the IR sample (Figure 3.1c) exhibits clear and strong streaking that is distinctly different from the other spots. These features, however, have essentially diminished and are only occasionally present in the IC sample (Figure 3.1b). No streaking could be identified in spot patterns from fresh UO_2 sample (Figure 3.1a). We may recall that the results presented in Figure 3.1 are single spot Laue images. Within the complete data-set in scanning μ-XRD of irradiated UO_2 particles, slight transverse curvatures and uniform streaking in spots

(mostly induced by cross-slipped and tangled dislocations) are also observed in some cases. These data have not yet been analysed in detail and are therefore not presented. Here, we have concentrated on the spot intensity distributions that display non-uniform streaking, observed experimentally as occasional splitting of individual spots into 2 or more sub-domains. Samples of irradiated UO_2 particles are examined and single point Laue image analyses have been performed to localize polygonized regions. To estimate the apparent number of sub-grains per grain the profiles of intensity distribution of the (311) reflection were analysed as a function of azimuthal angle ψ as described below.

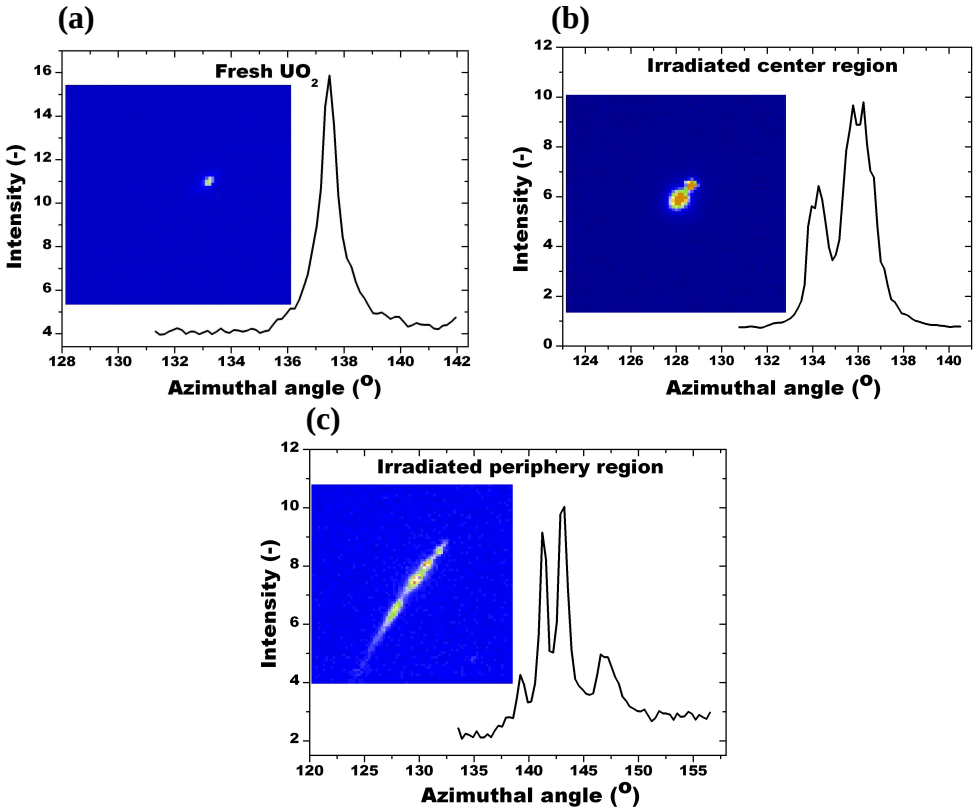

Figure 3.10: Plot of Laue spot evolution and intensity distribution over a limited azimuth range for chromia-doped UO_2 fuel specimens. Laue spots are shown in inserts. Illustrated are representative examples showing the characteristic peak splitting of the (311) reflection; (a) fresh fuel pellet, (b) centre region of the irradiated pellet (IC), and (c) periphery region of the irradiated pellet (IR).

Examples of magnified images of the (311) reflection, illustrating the change in spot shape and distinct splitting observed experimentally in chromia-doped UO_2 samples are shown in Figure 3.10. Pixilation of the CCD detector can be clearly seen in all Laue spots. Analysis of the (311) UO_2 Laue spot (inserts in Figure 3.10 for irradiated samples reveals strong broadening in the transverse direction, which can not be observed for the

fresh UO_2. The comparison of the intensity distribution for unirradiated, IC and IR samples shows that the total angular width (azimuthal) of the two IC and IR samples is much larger than for the unirradiated sample. For the unirradiated material, only one single peak without satellite is always recorded regardless of any specific location within the fuel pellet examined. This is shown in Figure 3.10a and the measured value of the peak width $\Delta\psi$ (FWHM) is 1.0 ± 0.2, the error corresponds to the pixel size and the standard deviation from the fitting. Profiles of intensity distribution of irradiated UO_2, however, are different, typically consisting of more than one single peak. In the IC sample, 2 – 3 main peaks (Figure 3.10b) are observed in single spot images; for IR up to 4 peaks have been recorded (Figure 3.10c). Current values of $\Delta\psi$ range from 0.7 to 1.5 ± 0.2^o for the (311) reflex in these samples. Interestingly, most of the peaks are well separated although some components have a relatively weaker signal at the respective intensity level. These structures seem to emanate from polygonized sub-grains in irradiated UO_2. The presence of several peaks or group of peaks could indicate that subdivided grains have been illuminated by the synchrotron micro-spot beam in the respective location within the sample particle examined. In that case, it seems plausible to assume that the number of peaks recorded is related to the number of sub-grains being exposed to the beam. For a given diffraction line and at the next step (of 3 μm interval) in scanning μ-XRD similar Laue pattern does not always reappear. This suggests the very local occurrence of these sub-grains and the probability for yielding any reflections from sub-grains depends on the probability of finding any such micro-structures within the illuminated sampling volume being spanned.

The comparison between sub-grains size values with actual grain size, as they appear in scanning μ-XRD, is not very straightforward. It is difficult to extract such information automatically by image processing, as varying sampling depths due to the penetration of X-rays and remnant structural disorder originating from irradiation effects do not allow to separate these features from the images. In fact, a quantitative connection between sub-grains and original grain necessarily needs assumptions on the actual size of the irradiated UO_2 particle that we have analyzed. Sub-grain numbers (i.e., number of recorded peaks) in each analyzed sample particle were counted from all single shot Laue images and

normalized with respect to the corresponding grain dimension of fresh fuel (see Table 3.1). The size of the analyzed irradiated particle in scanning μ-XRD was about 80 μm for the IC and about 60 μm for the IR sample. Figure 3.11 presents the analysed numerical results for the apparent number of sub-grains per fuel grain as a function of local burn-up in the standard UO_2 and the chromia-doped UO_2 sample.

The data from $(Pu,U)O_2$ MOX fuel are also included in Figure 3.11 as they provide additional data for intermediate and/or high burn-up regime. The results show a general trend that polygonization increases with local burn-up.

Coming back to Fig. 3.11, we may infer that even for a burn-up of about 30 MWd kg^{-1} the first steps of UO_2 polygonization is evident from X-ray diffraction, which otherwise may not be observed from other typically employed microscopy techniques like EPMA or scanning electron microscopy. It is important to emphasize here that this step is not due to only the presence of fission gases or any pressurized intra-granular bubbles, which may induce fracture of UO_2 grains as discussed in prior research [37]. Thus, polygonization is obviously also driven by the strain energy. An estimation of the strain yielding cracking in UO_2 may be calculated using the stress–strain relation given by Hooke's law:

$$\sigma = E \cdot \varepsilon \tag{3.8}$$

where σ is the normal stress proportional to strain, ε, with the constant of proportionality, i.e. the elastic modulus, denoted by E, as also used in equation (3.5). In a simplified approach, it can be assumed that the stress is increased linearly with the strain up to a critical limit of ε_F beyond which the UO_2 grain fails and a fracture is initiated. For calculating an estimate of ε_F, experimental data from literature can be utilized. Pujol *et al*. [38] have shown that dissolution of fission products causes UO_2 stiffness to increase during irradiation, namely at a rate of 3.5% per 10 MWd kg^{-1} of burn-up. The average value of E reported from experiment is ~ 260 GPa for a burn-up of 30 MWd kg^{-1}. Note that the fracture stress (σ_F) of UO_2 is temperature dependent. Using a fracture stress value of 200 MN/m^2 [39] for a temperature of 1300 K that is in the range of operating conditions at the pellet centre of LWR fuels, we estimate ε_F of ~ 0.8×10^{-3} by equation

(3.8). This critical strain ε_F is already lower than the strain we have found experimentally to be about 4×10^{-3} in our results (see previous section), based on the simplified approach considering fuel polygonization at this burn-up of 30 MW d kg^{-1}.

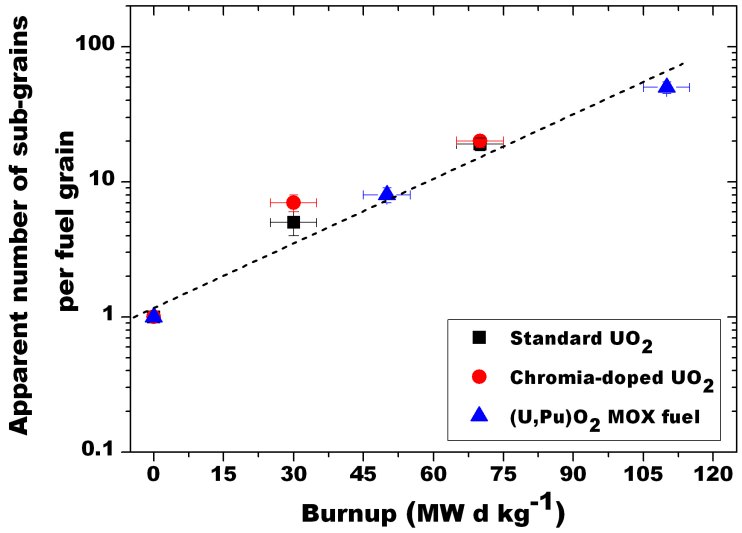

Figure 3.11: Apparent number of sub-grains per grain as a function of burn-up for irradiated fuel materials. The dashed line is only to guide the eye. See the text for detail.

During normal operating conditions, the fuel experiences temperatures between ~ 1300–1500 K at the centre area and between ~ 600 – 800 K at the periphery. As already mentioned, polygonization in UO_2 is probably triggered mostly by irradiation induced dislocations. The grain subdivision is controlled by the competition between dislocation production, which is governed by the local fission rate, and defects annealing, which is mainly controlled by temperature. The damage annealing is higher (so called healing effect) for the centre area than for the periphery in the fuel pellet. The effect of temperature on the failure behaviour of UO_2 has been investigated by Canon *et al.* [40]. With four-point bend tests a brittle-to-ductile transition temperature could be revealed at about 1500 K. This is a further argument for less polygonization in the hot fuel centre compared to the colder rim.

3.4 Intermediate XRD summary and conclusions

The following samples have been analysed: (a) un-irradiated un-doped and (b) chromia-doped; both, irradiated (c) standard and (d) chromia-doped UO_2 which stem from a commercial LWR reactor irradiated up to an average burn-up of ~ 40 MWd kg^{-1} and (e) MOX fuel irradiated up to a burn-up of ~ 60 MWd kg^{-1}.

Synchrotron based analytical methods of micro- X-ray fluorescence (μ-XRF) and X-ray diffraction (μ-XRD) were used to probe the specimens. Single spot Laue diffraction images of the specimens in scanning XRD mode have been collected with a high resolution CCD camera. The diffraction data of 2θ between 10^o and 30^o were analyzed with an emphasis on the (311) XRD line profile, taken as indictor of any structural alteration of UO_2 crystallites in an atomic scale. There was a measurable variation in the position as well as the width of this line in scanning μ-XRD data set obtained from irradiated fuel particles. The lattice parameters of UO_2 in fresh and irradiated specimens have been measured and compared with theoretical predictions. In the data analysis, the role of Cr as a dopant and the impact of several fission product elements resulting from irradiation have been considered. The trends observed are that in fresh UO_2 the lattice contracts as a result of Cr_2O_3 doping, but expands in irradiated materials. The lattice parameters in fresh materials are found to be 5.472 ± 0.002 Å and 5.469 ± 0.002 Å for undoped and doped UO_2, respectively. All irradiated samples behave in a similar manner (at the given burn-ups) with UO_2 lattice expansion occurring upon irradiation, where any Cr induced effect seems insignificant and irradiation induced defects prevail. The expansion is about 12×10^{-3} Å (an average value) with respect to the unit cell parameter of fresh UO_2. Elastic strain energy densities in the irradiated fuels are also evaluated based on the UO_2 crystal lattice strain and non-uniform strain. The origin of the strain both for undoped and chromia-doped specimens is considered to be the same, i.e. irradiation defects. Results of μ-XRD measurements on chromia-doped UO_2 fuel particles, taken from the centre region of the irradiated pellet, indicate a lattice strain of about 0.4%, which is not significantly different from the corresponding result for the standard UO_2. This magnitude of strain is in the range linked with polygonization. As a consequence, subdivision of UO_2 grains occurs, and this can be observed in the μ-XRD

data. In this work, the grain subdivision process has been observed in all irradiated UO_2 samples that were examined. Polygonization is dependent on local burn-up: in fresh fuels no polygonization is found, in the centre region of irradiated pellets some polygonization is detected. The effect is more pronounced in the rim area of irradiated pellets. Apparent numbers of sub-grains per UO_2 grain as a function of burn-up are reported. The method described here, applying micro-focused synchrotron radiation, appears to provide a novel method of determining grain specific both stress-free lattice spacing and strain distributions in irradiated nuclear fuels.

3.5 References

1 A. Leenaers *et al.*, *On the solubility of chromium sesquioxide in uranium dioxide fuel*, J. Nucl. Mater. 317 (2003) 62-68.

2 W. De Nolf and K. Janssens, *Micro X-ray diffraction and fluorescence tomography for the study of multilayered automotive paints*, Surf. Interface Anal. 42 (2010) 411-418.

3 S. C. Middleburgh *et al.*, *Solution of trivalent cations into uranium dioxide*, J. Nucl. Mater. 420 (2012) 258-261.

4 M. Idiri *et al.*, *Behavior of actinide dioxides under pressure: UO_2 and ThO_2*, Phys. Rev. B 70 (2004) 014113.

5 L. Vegard, *Die Konstitution der Mischkristalle und die Raumfüllung der Atome*, Z. Phys. 5 (1921) 17-26.

6 D. J. Kim, *Lattice Parameters, Ionic Conductivities, and Solubility Limits in Fluorite-Structure MO_2 Oxide [M = Hf^{4+}, Zr^{4+}, Ce^{4+}, Th^{4+}, U^{4+}] Solid Solutions*, J. Am. Ceram. Soc. 72 (1989) 1415-1421.

7 T. Cardinaels *et al.*, *Chromia doped UO_2 fuel: Investigation of the lattice parameter*. Nucl. Mater. 424 (2012) 252-260.

8 B. Dorado, *Stability of oxygen point defects in UO_2 by first-principles DFT+U calculations: Occupation matrix control and Jahn-Teller distortion*, Phys. Rev. B 82 (2010) 035114 .

9 http://xraysweb.lbl.gov/microdif.

10 P.V. Nerikar *et al.*, *Thermodynamics of fission products in $UO_{(2 \pm x)}$*,Condens. Matter 21 (2009) 435602

11 R.W. Grimes and C. R. A. Catlow, *The Stability of Fission Products in Uranium Dioxide*, Phil. Trans. R. Soc. Lond. 335 (1991) 609-634.

12 J. P. Crocombette, *Ab initio energetics of some fission products (Kr, I, Cs, Sr and He) in uranium dioxide*, J. Nucl. Mater. 305 (2002) 29-36.

13 G. Brillant *et al.*, *Fission products stability in uranium dioxide*, J. Nucl. Mater. 412 (2011) 170-176.

14 D.C. Parfitt and R. W. Grimes, *Predicting the probability for fission gas resolution into uranium dioxide*, J. Nucl. Mater. 392 (2009) 28-34.

15 H. Kleykamp, *The chemical state of the fission products in oxide fuels*, J. Nucl. Mater. 131 (1985) 221-246.

16 C.T. Walker *et al*., *Observations on the release of cesium from UO_2 fuel*, J. Nucl. Mater. 240 (1996) 32-42.

17 W. Hume-Rothery, *Elements of Structural Metallurgy*, Institute of Metals London, Monograph and Report Series No. 26 (1961).

18 R. D. Shannon, *Revised effective ionic radii and systematic studies of interatomic distances in halides and chalcogenides*, Acta Cryst. 32 (1976) 751-767.

19 H. Kleykamp, *The solubility of selected fission products in UO_2 and (U,Pu)O_2*, J. Nucl. Mater. 206 (1993) 82-86.

20 K. Une *et al., Microstructural change and its influence on fission gas release in high burnup UO_2 fuel*, J. Nucl. Mater. 188 (1992) 65-72.

21 J. Spino and D. Papaioannou, *Lattice parameter changes associated with the rim-structure formation in high burn-up UO_2 fuels by micro X-ray diffraction*, J. Nucl. Mater. 281 (2000) 146-162.

22 A. N. Goland and D.T. Keating, *Lattice Parameter, Volume, and Length Changes in Crystals Containing Dislocation Loops*,J. Appl. Phys. 41 (1970) 814-815.

23 M. Iwasawa *et al*., *First-Principles Calculation of Point Defects in Uranium Dioxide*, Mater. Trans. 47 (2006) 2651-2657.

24 H. Matzke and A. Turos, *Ion implantation studies of UO_2 and UN*, J. Nucl. Mater. 188 (1992) 285-292.

25 N. Ishikawa, *et al*., *X-ray study of radiation damage in UO_2 irradiated with high-energy heavy ions*, J. Nucl. Mater. 419 (2011) 392-396.

26 C. Degueldre *et al., Plutonium–uranium mixed oxide characterization by coupling micro-X-raydiffraction and absorption investigations*, J. Nucl. Mater. 416 (2011) 142–150.

27 M. Amaya *et al*., *Measurements of Crystal Lattice Strain and Crystallite Size in Irradiated UO_2 Pellet by X-ray Diffractometry*, J. Nucl. Sci. Technol., 45 (2008) 244-250.

28 A. Debelle *et al., Strain and stress build-up in He-implanted UO_2 single crystals : an X-ray diffraction study*, J. Mater. Sci. 46 (2011) 4683-4689.

29 K. Une and M. Oguma, Oxygen *potentials of UO_2 fuel simulating high burnup*, J. Nucl. Sci. Technol., 20 (1983) 844-851.

30 G. K. Williamson and W. H. Hall, *X-ray line broadening fromfiled Al and W*, Acta. Metal. 1 (1953) 22-31.

31 M. Amaya *et al*., *Relationship between Changes in the Crystal Lattice Strain and Thermal Conductivity of High Burnup UO_2 Pellets*, J. Nucl. Mater. 396 (2010) 32-42.

32 T. Sonoda *et al*., *TEM observation on irradiation-induced microstructural evolution in high burn-up UO_2 disk fuel*, Nucl. Instr. Meth. B 191 (2002) 622-628.

33 V. V. Rondinella and T. Wiss, *The high burn-up structure in nuclear fuel*, Mater. Today 13 (2010) 24-32.

34 J. Y. Oh *et al*., *Simulation of high burnup structure in UO_2 using potts model*, Nucl. Engin. Tech. 41 (2009) 1109-1114.

35 H. Y. Geng *et al*., *Molecular dynamics study on planar clustering of xenon in UO_2*, J. Alloy. Comp. 457 (2008) 465-471.

36 K. Nogita and K. Une, *Radiation-induced microstructural change in high burnup UO_2 fuel pellets*, Nucl. Instrum. Meth. B91 (1994) 301-306.

37 J. Spino *et al*., *Detailed characterisation of the rim microstructure in PWR fuels in the burn-up range 40-67 GWd/tM*, J. Nucl. Mater. 231 (1996) 179-190; and references therein.

38 M. C. Pujol *et al*., *Bulk and Young's modulus of doped UO_2 by synchrotron diffraction under high pressure and Knoop indentation*, J. Nucl. Mater. 324 (2004) 189-197.

39 A. G. Evans and R. W. Davidge, *The strength and fracture of stoichiometric polycrystalline UO_2*, J. Nucl. Mater. 33 (1969) 249-260.

40 R. F. Canon *et al*., *Deformation of UO_2 at High Temperatures*, J. Am. Ceram. Soc. 54 (1971) 105-112.

Chapter 4: Chromium Speciation

The objective of this part of the study was to analyze in a non-destructive way the atomic scale microstructure of the chromium oxide precipitates found in the chromia doped UO_2 fresh fuel. The next neighbour atomic environment of dissolved chromium in UO_2 matrix (before and after irradiation) has been also investigated for chromia doped fuels. An industrial grade fresh Cr_2O_3-doped UO_2 pellet was examined beforehand, using scanning electron microscopy and electron probe micro analysis. The average grain diameter of the UO_2 matrix was obtained by a SEM image analysis method. Precipitates were detected by EPMA. For all precipitates of micrometer scale analyzed by EPMA the composition was determined to be very close to Cr_2O_3. In the following, the structural properties and the next neighbour Cr atomic environment in these precipitates were studied by a combination of more sensitive tools such as micro-focused X-ray diffraction (μ-XRD) and absorption spectroscopy (μ-XAS).

4.1 Chromium precipitation

The grain microstructure of the chromia doped UO_2 was examined with the help of the SEM, see the example in Figure 4.1. The doped fuel is characterized by a homogeneous grain microstructure comprising large UO_2 grains as compared to conventional, undoped UO_2 fuel [1]. As pores are inherent parts of as-sintered UO_2 they are also observed, both within the grains and at grain boundaries. A combined SEM and image analysis revealed an average grain size of ~ 48 μm using the standard procedure [2]. The larger pores size has been estimated to be between 0.3 and 7 μm, located in some areas of the sample examined.

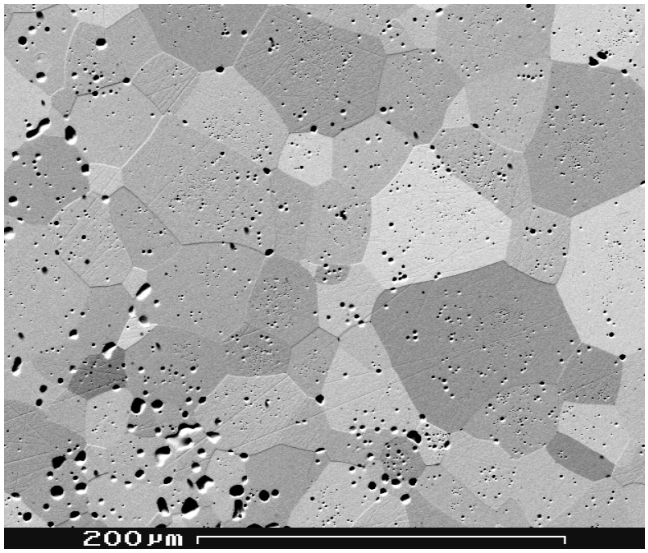

Figure 4.1: SEM image from a selected area of the sintered UO_2 fuel pellet fabricated with 0.16 wt.% of Cr_2O_3 as a dopant. The polished UO_2 specimen was etched with a H_2SO_4 (10%) and H_3PO_4 solution (490 K, 400 s) prior to the SEM examination.

4.1.1 EPMA Studies

It was difficult to examine by SEM directly Cr-rich regions in the specimen and distinguish between pores and precipitates and/or any surface particles from backscattered electron images (BSE). The precipitates are either spherical appearing similar to pores or they are angular especially when occasionally found at grain boundaries. Remains of precipitates were also observed in pores suggesting that part of them were lost during sample preparation. Cr_2O_3 particles were observed by EPMA and the chemical compositions were determined from elemental X-ray mapping of uranium, chromium and oxygen. Furthermore, several mappings at various locations were made to visualize the distribution, size and number density of Cr_2O_3 precipitates. In these zones, additional spot-mode analyses were made to confirm the matrix Cr content in the fuel. In order to quantify the chromium content as accurate as possible either dissolved in the UO_2 matrix or in the precipitates, several analyses were combined.

An example of EPMA observation of chromium in chromia doped UO_2 is presented in Figure 4.2. The elemental mapping of Cr shows high intensity localized spots at the surface of the specimen (Figure 4.2a); mapping of oxygen revealed similar spots (image not shown). Figure 4.2b represents typical characteristic X-ray spectra of Cr in the doped

UO_2 pellet. Characteristic Cr K_α X-rays under the micro-particles are observed with high intensities, whereas the K_α X-rays intensity of Cr in the UO_2 matrix is very low (inset in Figure 4.2b). The bright spots obtained in the Cr and O elemental EPMA maps always coincide with surface features observed at the corresponding backscattered electrons (BSE) images, suggesting the presence of chromium oxide precipitates. Detailed EPMA image analyses reveal that the precipitates just below the surface appear apparently smaller depending on their locations in a shallow sub-surface zone and the penetration depth of the incident electron beam. Their number and size distributions are quite regular all over the specimen, whereas the exact quantification of the number or sizes has not been considered for this work. The shape of the precipitates found is spheroidal and the size range is from submicron up to about 7 μm when the precipitates in pores are included. The characteristic X-ray fluorescence spectra reveal that all precipitates contain Cr and O and they are clearly in an oxide state.

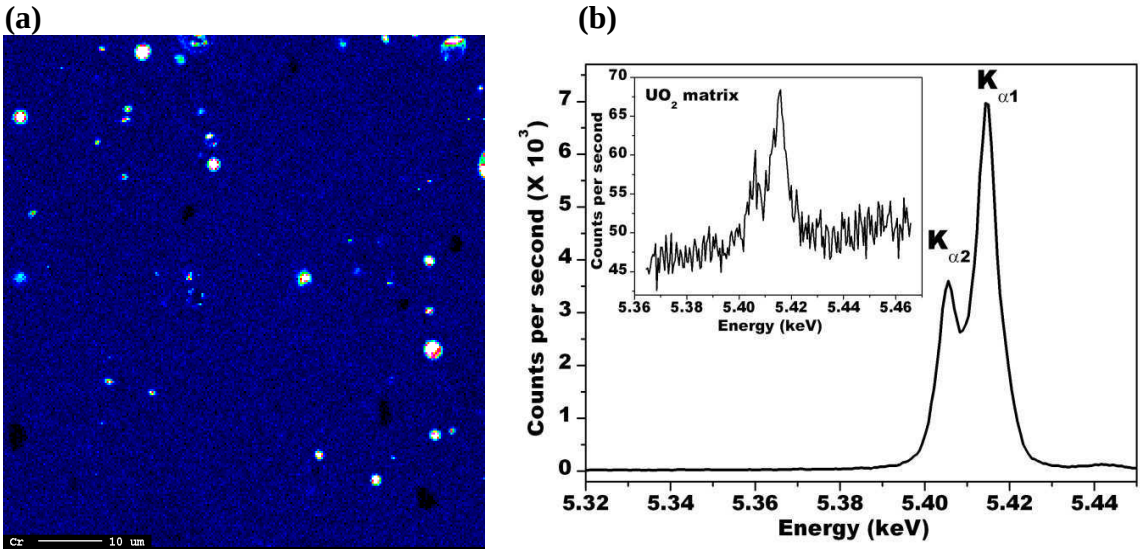

Figure 4.2: EPMA – distribution of chromia. a) X-ray image with Cr mapping; b) X-ray spectrum (Cr K_α line) measured from a Cr_2O_3 precipitate. In the inset the respective Cr X-ray spectrum of dissolved chromium measured in UO_2 matrix is shown. Note that the X-ray yields differ by almost two orders of magnitude in the two spectra. The analysis was carried out under identical EPMA conditions (10 keV, 92 nA, electron beam spot size ~ 150 nm). See text for details.

Figure 4.3 illustrates the distribution of Cr, O and U from a selected region of the specimen, observed by high resolution EPMA mapping. Characteristic line-scan profiles over the exposed areas are displayed in the images. The mappings are a non-absolute analysis and give the spatial distribution of elements in the observed region. The colour

bar counts presented in the image deliver only relative information. Figure 4.3a and Figure 4.3b clearly show the presence of Cr and O in the precipitates. From EPMA line analysis, little or no uranium is found inside the precipitates (Figure 4.3c) and little chromium in the UO_2 matrix (Figure 4.3b). When little uranium is found it exists only in small concentration, for smaller precipitates in particular, which is due to the resolution effect in EPMA with impact originating from the surrounding matrix.

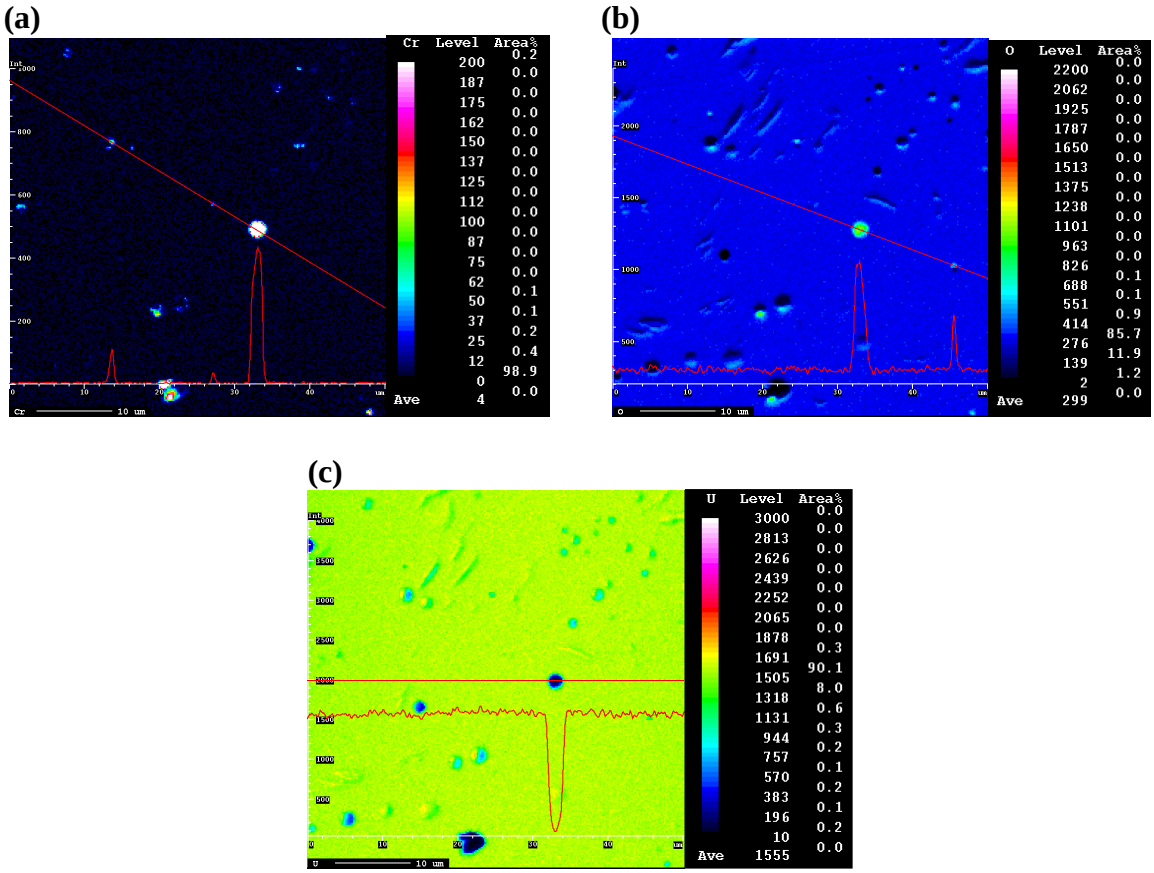

Figure 4.3: Single-precipitate analysis in high resolution mode by EPMA in a 50 µm × 50 µm area. The selected Cr_2O_3 precipitate has a diameter of about 2.5 µm. The X-ray mappings together with intensity scales of the specific elements (a) Cr, (b) O and (c) U are shown as well as corresponding line-scan profiles over the exposed area.

We have analyzed 10 large chromium precipitates (≥ 2 µm) at different locations on the sample. The composition of the precipitates is found to be very close to Cr_2O_3. The uncertainty estimate in the obtained chemical composition is ≤ 1%, associated mainly with the analysis of oxygen content in the fuel specimen and its comparison with reference standard materials. The trace amount of Cr has been also verified and measured at 10 different locations excluding pores and precipitates in the fuel matrix. Due to a low

chromium signal from the matrix, Cr, U and O fluorescent spectra in spots mode have been acquired for longer measurement time. The mean Cr concentration in the sample is found to be ≅ 0.07±0.01 wt.% as the dissolved component in the UO_2 matrix, from EPMA data analysis.

4.1.2 μ-XRF and μ-XRD Analyses

Results from elemental μ-XRF scans showing the Cr distribution in chromia doped UO_2 are presented in Figure 4.4. The incident synchrotron X-ray energy of 6200 eV, slightly above the Cr K-edge excitation energy, was selected for the mapping. A measuring time of 10s per pixel was chosen to achieve data with good counting statistics. Figure 4.4a displays a larger area map on the specimen and Figure 4.4b represents the high resolution μ-XRF scan of an isolated Cr-bearing precipitate from a selected sampling area. The colour bar of Cr K_α counts in Figure 4.4 deliver only relative information. It is important to mention that Cr counts are magnified in Figure 4.4b so that areas with intermediate to low Cr fluorescence counts also appear. Particles of Cr are indicated by the presence of purple and red colors in Figure 4.4a, while the cyan patches also indicate Cr-bearing precipitates below the sample's surface.

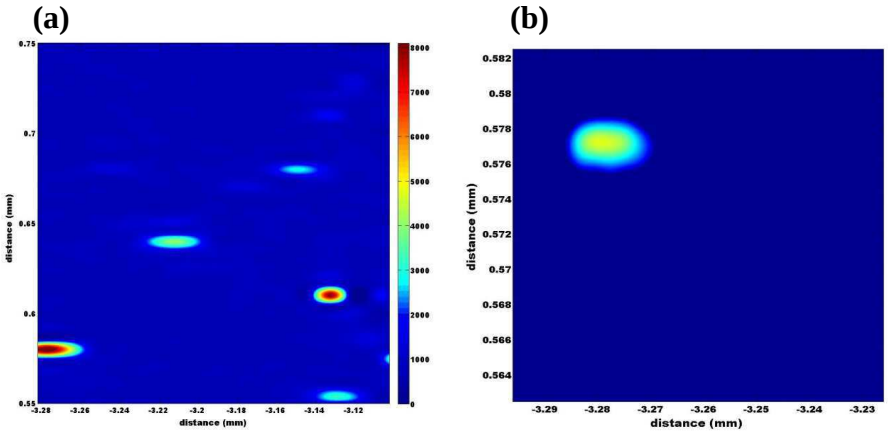

Figure 4.4: (a) μ-XRF 200 μm × 200 μm map of chromia-doped UO_2 recorded at excitation energy of 6200 eV. The distribution of Cr is shown and regions with high concentration are detected. (b) High resolution μ-XRF scan of an isolated Cr-bearing precipitate. The diameter of the precipitate is about 7 μm.

All hotspots appear as somewhat elongated horizontal streaks. It is related to the different focal spot size of the incident X-ray beam used on the sample, approximately about 3 μm × 1 μm, elongated along the horizontal direction.

As already mentioned in chapter 2 (section 2.3) the μ-XRD measurements were performed using the photon energy of 17200 eV. At this energy and normal incidence angle geometry, the X-rays attenuation length in UO_2 is about 22 μm. Therefore, the diffraction signal arises from a sample volume which is defined by the lateral beam dimensions, i.e., 1 μm × 1 μm, and the attenuation length, which is 22 μm. At this condition, the structural information that is gathered should correspond to an average result of a couple of individual precipitates present along the beam path and illuminated by the X-ray beam. These particles, however, were not easily detectable using 17200 eV X-rays because of the absence of any Cr fluorescent signal and their fine dispersion in the UO_2 matrix. In addition, the volume fraction of Cr_2O_3 with respect to UO_2 was extremely low; the latter was dominating to yield CCD saturation for longer acquisition times. Therefore, the complete micro-diffraction analysis was accomplished by step-wise moving the sample edge across the focused beam of 1 μm × 1 μm in steps of 5 μm. The Laue images were captured for an exposure time of 3s. In practical terms, the measurements were evaluated by analyzing Cr_2O_3 crystalline phase by means of a search/match program [3] and inspecting about 200 diffraction spectra collected from the thinner area at the sample edge.

An example of combined μ-XRF with μ-XRD to analyze Cr_2O_3 precipitates is shown in Figure 4.5. The probing region of the specimen in scanning μ-XRD was identified by the uranium μ-XRF map recorded over the same sample area at the mentioned incident energy. Figure 4.5a shows the U L_α fluorescence intensity map covering an area of 100 μm × 100 μm. As seen in the micrograph, uranium imaging does not provide any good colour contrast for additional patterns or weak/hot spots in the specimen. Although the specimen should have some Cr_2O_3 particles in the scanned area, their contribution seems hidden by the high uranium intensity. The lateral resolution in the uranium map is furthermore limited by the penetration depth of the X-ray beam. However, rescaling the

U map using a log-scale band in higher magnifications micrographs clearly demonstrate weaker phase contrast of open pores on the UO_2 surface.

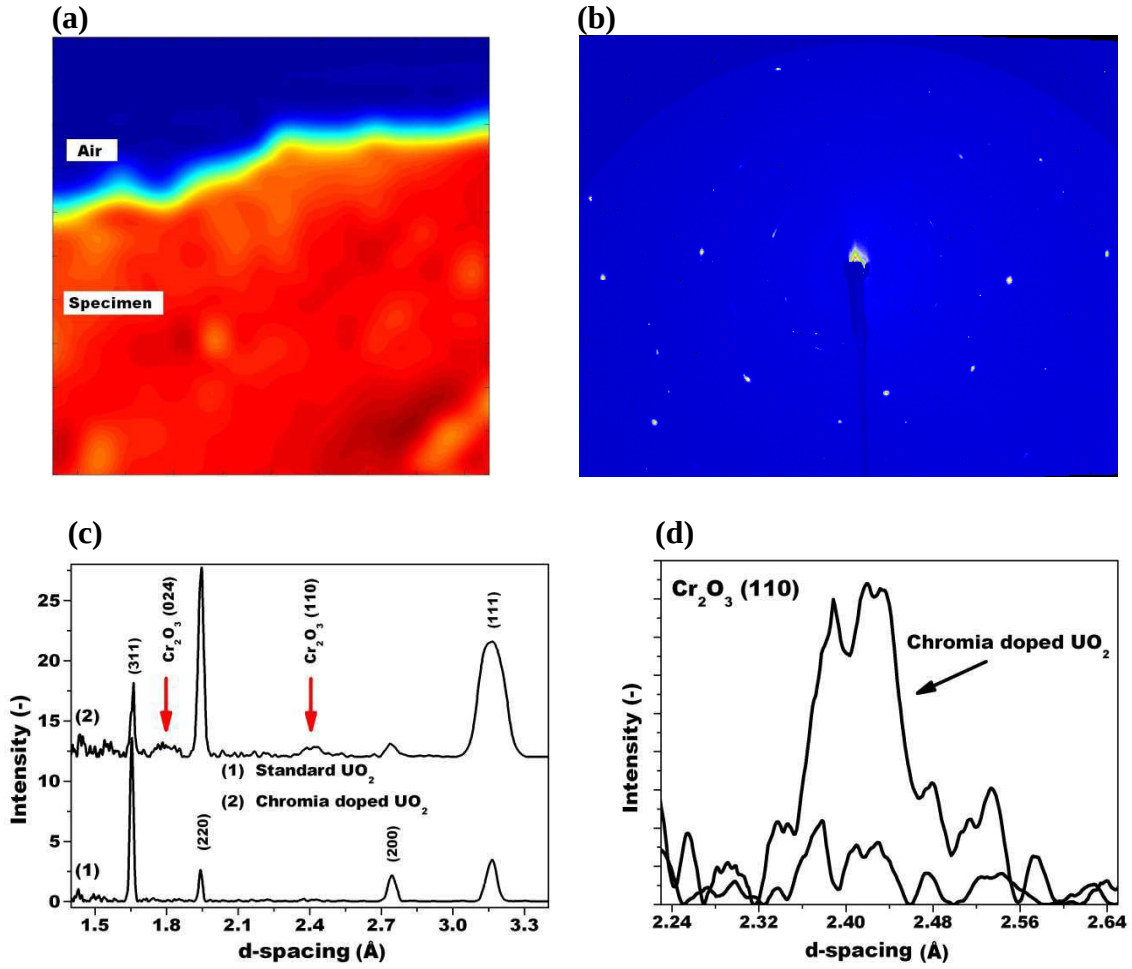

Figure 4.5: (a) µ-XRF map with U L_α fluorescent line measured from the sample shown in Fig. 4.1. Imaging size: 100 µm × 100 µm, pixel size: 5 µm × 5 µm, XRF spectrum collection time per pixel: 3 s. (b) Selected single-spot 2D µ-XRD image from the sample. (c) Integrated 1D X-ray diffraction pattern of the Laue image showing several diffraction lines for Cr_2O_3 doped and undoped standard UO_2. The plots are vertically shifted to each other for clarity. (d) Magnified view of the Cr_2O_3 (110) diffraction peak from the extracted residue of standard UO_2 and chromia doped samples. See text for details.

Since each image pixel is related to a position on the sample, the main utility of the map is that it makes possible to identify areas of homogeneous UO_2 matrix, avoiding open surface-pores or artefacts, thus allowing the selection of representative spots for the µ-XRD spectra.

Figure 4.5b shows a selected Laue image obtained from micro-beam XRD. The gauge volume was located very close to the border of the apex (Figure 4.5a). The micro-beam has penetrated through the UO_2 and produced Laue spots both from the UO_2 and Cr_2O_3. Most of the bright spots in Figure 4.5b originate from UO_2, contributions of chromium-rich particles are not directly visible due to the particles' low volume fraction.

Figure 4.5c illustrates the integrated 1-D X-ray diffraction pattern of the Laue image shown in Figure 4.5b. The background intensity is subtracted using the dark current CCD image. For comparison, a micro-beam XRD spectrum measured form a standard UO_2 specimen is included in the figure. Figure 4.5d shows the enhanced line profile of the Cr_2O_3(110) diffraction peak from the extracted residue of the standard and chromia doped samples. All intense peaks of the standard and doped UO_2 specimens can be well-indexed to a cubic fluorite structure of uranium dioxide [8]. Two distinctive weak peaks (see arrows at about 1.8 and 2.4 Å d-spacing in Figure 4.5c) are observed for the chromia doped specimen. There is no exact match of these peaks with those of UO_2, but the best match is for the chromium sesquioxide phase [3].

The crystal lattice structure of Cr_2O_3 is of corundum type (space group $R\bar{3}c$, no. 167) and the hexagonal close packed unit cell at room temperature is given by $c_H/a_H = 2.740$ [4]. Here, c_H denotes the height of the cell and a_H represents the length of the sides of the base. The interplanar spacing of successive lattice planes (d) of Miller indices (hkl) is given by the following relation:

$$d_{hkl} = \left[\left(h^2 + k^2 + hk\right)\frac{4}{3a_H^2} + \frac{l^2}{c_H^2} \right]^{-\frac{1}{2}} \qquad (4.1)$$

The residual method, using PeakFit [5] has been applied for the analysis of the diffraction peaks in the chromia doped UO_2. In this method, the residual is the difference in the y values between a data point of two specimens (undoped and doped UO_2) evaluated at the data point's x value. The results show that those peaks are indeed of polycrystalline Cr_2O_3 phase, exhibiting well resolved (024) and (110) diffraction lines corresponding to interplanar spacings (d) of 1.79 and 2.42 Å, respectively, determined within an accuracy of ±0.01 Å. Using the relationship given by Eq. (4.1) the unit cell lattice parameters of

the chromia particles are estimated to be a_H = 4.84 Å and c_H = 13.72 Å. These values are somewhat different compared to those found in literature, a_H = 4.953 Å and c_H = 13.578 Å for standard α-Cr_2O_3 hexagonal crystal cells [6]. The differences can be attributed to the crystallinity level of chromia particles in UO_2. It also should be mentioned that both (024) and (110) lines widths of chromia particles in the fuel exhibit larger values compared to the reference powder specimen. This relates to the measured μ-XRD pattern of fine Cr_2O_3 precipitates in an imperfect state resulting Bragg scattering in the presence of lattice defects. Further investigation on these changes (i.e., intensity, line width etc. in the XRD pattern) can be performed by detailed synchrotron μ-XRD measurements on isolated Cr_2O_3 precipitates especially prepared from UO_2 samples. Future attempts shall be made to produce such specifically targeted specimens by focused ion beam (FIB) methods.

Analyzing the μ-XRD data of chromia precipitates the sole product is assumed to be pure Cr_2O_3. However, one can also consider the lattice structure of $(Al_xCr_{1-x})_2O_3$ depending on the aluminium content in those Cr_2O_3 particles. The presence of a trace amount of Al was confirmed (Al seems to stem from the lubricant utilized during pellet fabrication) by analysis with EPMA which showed a varying level of Al concentration (atomic) between 6 to 8% relative to the total chromium content in the chromia precipitates. It is also necessary to mention that no detectable amount of aluminium was measured in the UO_2 grains. According to the Vegard's law [7] for ternary $(Al_xCr_{1-x})_2O_3$ compounds, the lattice parameters have a linear dependence on the composition *x*, according to $c(x) = x \times c_{Al_2O_3} + (1 - x) \times c_{Cr_2O_3}$, where $c_{Al_2O_3}$, $c_{Cr_2O_3}$, and $c(x)$ are the respective *c*-axis lattice constants of the hexagonal structured Al_2O_3, Cr_2O_3, and $(Al_xCr_{1-x})_2O_3$. The same relation also holds good for the *a*-axis parameter of $(Al_xCr_{1-x})_2O_3$ alloy. Taking the average Al fraction *x* from EPMA results and using the literature data for unit cell parameters of Al_2O_3 [8] as well as Cr_2O_3 [6], we estimate a_H = 4.94 Å and c_H = 13.53 Å for the $Al_{0.14}Cr_{1.86}O_3$ composition. These lattice constants values with the prediction of Vegard's law do not agree well with the experimentally observed values. This result validates that the poor crystallinity and/or lattice distortion in remnant chromia crystallites is not due to any aluminium doping into those precipitates.

4.1.3 μ-EXAFS Investigations

The μ-XAS experiments in fluorescence mode were performed at the same area of μ-XRD measurements. We examined Cr K-edge absorption spectra in Cr-bearing precipitates of the UO_2 specimen. Precipitates were easily identified using μ-XRF mapping on the specimen (see Figure 4.4) and four separate precipitates analysis by μ-XAS were realized. At least ten individual scans were averaged to improve the signal-to-noise ratio for the Cr μ-XAS spectrum taken at a single spot location on the sample analyzing each μm-sized Cr_2O_3 precipitates in the fuel.

All chromium XAS data were reduced to normalized X-ray absorption near edge spectra (XANES) and extended X-ray absorption fine structure (EXAFS) files using the computer program IFEFFIT [9]. Thereafter, k^2-weighted EXAFS was Fourier transformed (FT) into real space to obtain a radial distribution function (RDF) of the near-neighbors around the absorbing Cr atom. A quantitative analysis was done on the FT peaks by using standard fitting procedures. Average bond lengths, R, average coordination numbers, CN, ΔE_0 (E_0 correction), and Debye–Waller (DW) factors, σ^2, were derived from these fits. Theoretical phase-shift and backscattering amplitude functions for quantitative EXAFS fitting were generated using the modern relativistic code FEFF-8.4 [10] and known atomic coordinates of α-Cr_2O_3 structure as referred earlier [11]. The FEFF model comprises all single scattering paths within the fit range and some selective multiple scattering paths up to 4.5 and 3.5 Å for standard α-Cr_2O_3 and Cr_2O_3 precipitates found in the chromia doped UO_2 fuel, respectively.

In the FT-data of standard α-Cr_2O_3 several peaks are visible, corresponding to distinct shells of Cr and O atoms at different distances from the absorbing chromium atom. Figure 4.6 shows the FT-EXAFS data of α-Cr_2O_3 reference powder specimen and Cr_2O_3 precipitates found in UO_2. The results are shown as radial distance function (RDF) (both experimental and corresponding best-fitted one). The quantitative EXAFS for all Cr_2O_3 precipitates in UO_2 were very similar, though not identical, and examples of only two measured μ-XAS spectra are shown in Figure 4.6b and Figure 4.6c. A cross check of the investigated particles revealed that there is no major difference between them with

respect to their Cr atomic environment, but there is a distinct difference to the pure α-Cr_2O_3 phase. This can be qualitatively seen in Figure 4.6d where the Cr FT of the EXAFS signals clearly feature differences in many respects, suggesting that there is significant structural changes in the atomic neighborhood around the Cr center. For the precipitates formed in UO_2, quantifiable differences in Cr–O and Cr–Cr bond lengths, coordination numbers and radial distribution functions can be distinguished in comparison with those of the α-Cr_2O_3 structure.

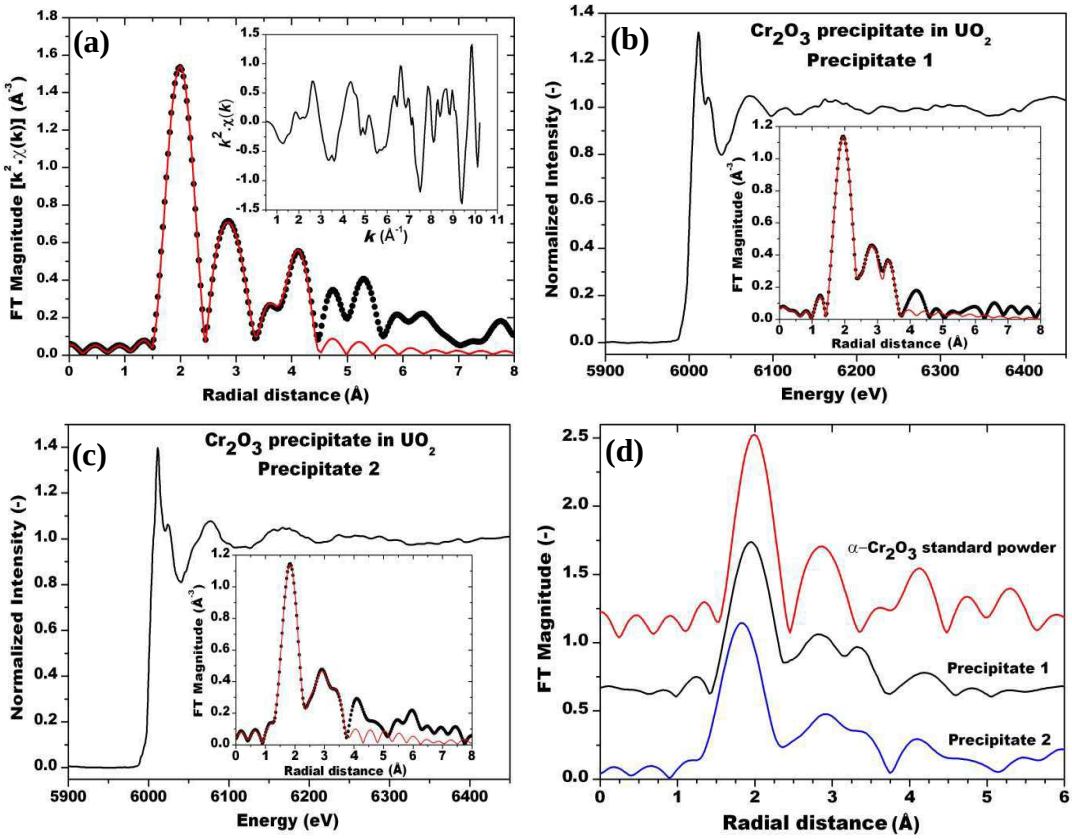

Figure 4.6: (a) Modulus of the k^2-weighted Fourier transforms of Cr EXAFS data measured from reference Cr_2O_3 powder specimen. The spectra drawn with points and solid curves are the observed and corresponding best-fitted one, respectively. In the inset, magnitude of the k^2-weighted experimental EXAFS signal versus the photoelectron wave number k is shown. (b) and (c) Normalized and background removed Cr K-edge absorption spectra of Cr_2O_3 in UO_2. Data are shown for two precipitates. In the insets, magnitude of the corresponding k^2-weighted Fourier transformed EXAFS signal (dot symbol) and the best- fitted curve (solid line) are shown. (d) Comparison of the Fourier transformed Cr K-edge EXAFS for reference Cr_2O_3 powder and the two precipitates analyzed in the UO_2 sample. In this plot, the curves are vertically shifted with respect to each other for clarity. The first prominent peaks in the Fourier transforms are assigned to the Cr–O contribution.

The EXAFS measurement from reference α-Cr_2O_3 reveals an excellent crystallinity around Cr atoms. The FT data presented in Figure 4.6a illustrates Fourier features which are characteristics of the Cr_2O_3 corundum structure cells [12]. By comparing the structural parameters obtained from EXAFS analysis of chromia precipitates in UO_2 with those of the standard α-Cr_2O_3, we have noticed that the interatomic distance of the averaged first two Cr–O shells is significantly shorter in the chromia precipitates of the doped fuel. In this sample the next neighbor number of six atoms in the oxygen octahedra is also reduced strongly in the Cr coordination sphere. A single-distance fit, after X-ray scattering phase shift is accounted for, yields a coordination number of 4.3±0.3, and a distance of 1.90 Å which is 0.09±0.02 Å smaller than the one (1.99 Å) evaluated for standard α-Cr_2O_3. In addition, the oxygen site of the chromia precipitates has about 28% vacancy, suggesting that there is significant structural change in the nearest neighbor Cr–O coordination sphere. In contrast, when looking at the metal–metal correlation the shortest chromium atom pairs found at 2.72 Å evidence a significant elongation of the Cr–Cr separation with respect to 2.64 Å distance in the reference material. The derived value of CN = 0.8±0.1 agrees well with the expected single-fold coordination for this shell. However, the best-fit average bond distances of Cr–O and Cr–Cr pairs, found for more distant oxygen and chromium atoms, do not tally very well with the corresponding crystallographic values. Further details on the structural environment around chromium in chromia precipitates found in UO_2 are described in Ref. [12]. Additional μXRD and μXAS work is required to determine the average crystallite properties and/or atomic scale microstructures of Cr_2O_3 precipitates in doped UO_2 pellets. Efforts will be made to examine different chromia doped UO_2 fresh fuel pellets as a function of initially added chromia enrichment, prepared under the same conditions.

4.2 Dissolved chromium

Since the Cr incorporated UO_2 structure can not be obtained directly from a measured EXAFS spectrum, model structures must be assumed. The corresponding simulated RDF or EXAFS/XANES spectrum should be calculated, with determination of which models best fit the data. The FEFF-code [10] has this attractive property when simulated with a cluster of atoms centered on the absorbing atom. In the following we first describe the results on experimental U L_3-edge EXAFS, the corresponding theoretical spectrum calculated applying FEFF for a fluorite-UO_2 structure, and state various FEFF-control cards required to match the experimental spectrum. This is followed by a comparison of experimental Cr K-edge results between fresh and irradiated specimens, and FEFF analyses considering a cationic substitutional behavior of chromium in UO_2. The aim was to evaluate the number and kind of nearest Cr neighbours necessary to reproduce at least the general shape of Cr K-edge experimental RDF spectrum. For the chromium uranium substitutional model, the use of U L_3-edge FEFF analysis made it simpler to analyze Cr K-edge spectrum. It provided most of the necessary parameters and relevant control-cards in the FEFF input file generated from uranium dioxide crystal structure, for quantitative fittings of Cr K-edge data.

4.2.1 μ-XRF measurements

The region for μ-XAFS measurements in the irradiated sub-sample was determined using μ-XRF mapping. The elements analyzed by XRF were uranium (L_α line intensity) and chromium (K_α line). The elemental maps of uranium and chromium measured at a selected location of the sample and an XRF spectrum acquired with an excitation energy of 6500 eV (above the Cr K-edge) from the specimen are presented in Figure 4.7. The fluorescence images show that uranium and chromium are systematically co-located and share rather a homogeneous distribution.

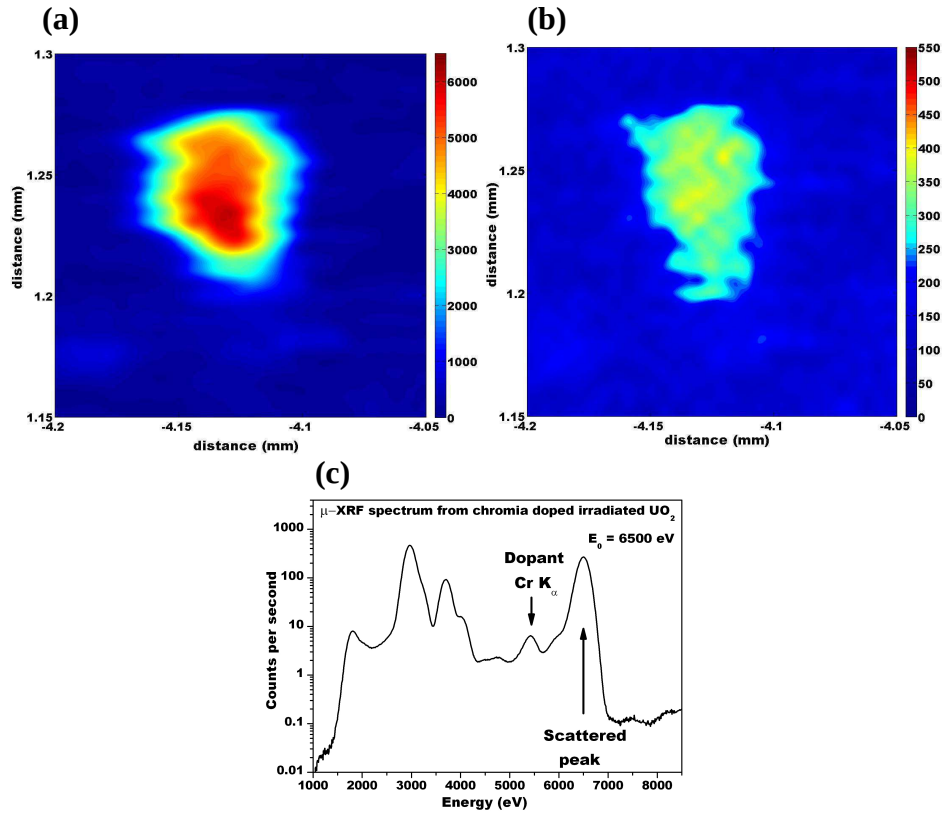

Figure 4.7: Microprobe synchrotron radiation XRF maps from an irradiated chromia doped UO_2 fuel particle are shown for elements (a) U and (b) Cr. Map size is 150 μm × 150 μm measured with a step size 3.0 μm in both directions. (c) A representative micro-beam XRF spectrum, with indicated chromium K_α signal, measured from the sample. Strong XRF peaks observed at the low energy side emanate from atmospheric argon at 2958 eV and Ca (present in the adhesive Kapton tape where fuel particles were collected) at 3692 eV.

The analyzed UO_2 fuel particle has a size of about 60 μm × 70 μm. Based on the imaging results single-spot Cr K-edge μ-EXAFS spectra were measured at different locations from this particle, where the probed volumes were apparently similar.

4.2.2 U L_3-edge EXAFS

Figure 4.8 shows the U L_3-edge EXAFS spectrum measured from the irradiated UO_2 and its simulation using the FEFF package. The first-derivative spectrum, used to evaluate the energy position of the edge, revealed the E_0 value of 17,170 ± 1 eV, is consistent with published data for U^{4+} oxidation state [13]. For a quantitative analysis of the experimental EXAFS, the fitting procedure was adopted using the standard methods as summarized in the experimental section. The FT was performed in the spectral *k* range of 2.5–11.5 $Å^{-1}$.

The resulting RDF is shown in Figure 4.8 as an inset. The dots represent the experimental values and the line the best fitted curve. Good fitting quality can be observed from the figure. It can be observed that the RDF around uranium exhibits mainly two major coordination peaks, the other peaks are only very weak. The first strong one at ~ 1.8 Å stands for the nearest oxygen neighbours (eight atoms), and the second peak at about 3.7 Å for the next nearest uranium (twelve atoms) neighbours that would tally well with the fluorite-UO_2 model structure.

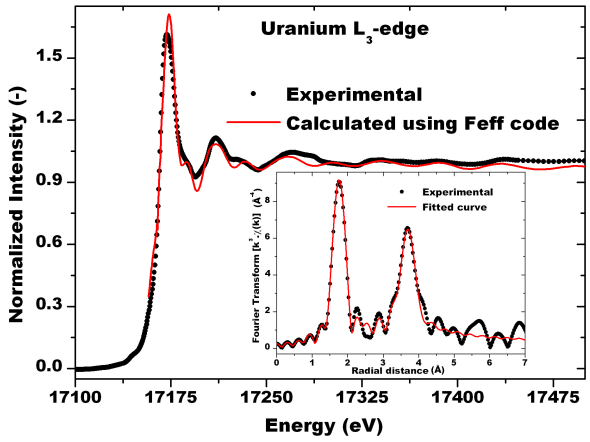

Figure 4.8. Normalized and background removed uranium L_3-edge absorption spectrum measured from the irradiated UO_2 together with FEFF calculated spectrum based on the refined structural parameters derived from EXAFS fits. In the inset, modulus of the k^3-weighted FT-EXAFS data is shown (uncorrected for phase shift function). The spectra drawn with points and solid curves are the experimental and corresponding best-fitted one, respectively. The fitting range was between 1.2 and 5.2 Å. See text for further details.

The local structural parameters obtained by the curve-fitting of U L_3-edge data are summarized in Table 4.1. FEFF fits to the FT-EXAFS reveal the presence of U–O backscattering at 2.36 ± 0.02 Å distance, U–U at 3.83 ± 0.03 Å and U–O at 4.41 ± 0.03 Å corresponding to the first three single-scattering paths. The coordination numbers of the U absorber are about 8, 11 and 24 with DW factors of $4\pm1\times10^{-3}$, $6\pm2\times10^{-3}$ and $13\pm2\times10^{-3}$ $Å^{-2}$, respectively, for these shells. According to the fits results, multiple-scattering components arising from oxygen and uranium neighbours also contribute at 3.71 and 4.33 Å distances. The spectral features shown in Figure 4.8 and the reported best-fit values of structural parameters in Table 4.1 are comparable with the outcome of other EXAFS studies on UO_2 available in the literature [14]. However, it is clear from the results of this

work that the low chromium content in the chromia-doped UO_2 grains does not produce any EXAFS signal for U–Cr pairs, uranium being the absorber atom, due to the very weak backscattering events from the insufficient amount of dopant atoms. On the contrary, EXAFS study of chromia-doped UO_2 at the chromium edge is able to provide a signature of the Cr–U coordination shell discussed later in this section.

Table 4.1: EXAFS fit parameters of U L_3-edge and Cr K-edge data. CN, R and σ are the coordination number, average radial distance and Debye-Waller factor, respectively. The estimated errors on the numerical results are mentioned in the text.

Chromia-doped UO_2 (irradiated)					Chromia-doped UO_2							
Absorber	Neighbour atom				Absorber	Neighbour atom	Pristine			Irradiated		
		CN	R(Å)	σ^2(Å^2)			CN	R(Å)	σ^2(Å^2)	CN	R(Å)	σ^2(Å^2)
U	O	7.7	2.36	0.004	Cr	O	6.5	2.02	0.003	6.2	2.05	0.004
	U	11.1	3.83	0.006								

Ab-initio calculations for the U L_3–edge EXAFS were undertaken using the FEFF package. The calculation was characterized by some default conditions, which included Hedin-Lundqvist-potentials, the many-pole model for the self energy and loss function, the core-hole treatment with final state rule and self-consistency. Since the primary purpose was to simulate uranium near-neighbour EXAFS, multiple scattering effects were neglected. Self consistency calculations were refined with a radius of 5 Å around the central U atom. The refined experimental parameters of the radial distances (R) (see Table 4.1) were reintroduced as fixed values with the help of the ATOM card in FEFF for the calculation of the EXAFS spectra. Since the code was unable to reproduce the experimental EXAFS features during the preliminary analyses, several calculation parameters in the relevant FEFF-control cards were varied, with the aim to analyze their influence on the theoretical spectra. After some tests, the final calculation comprised a correction factor of 9.5 eV related to the Fermi level and a Debye temperature of UO_2 (400 K [15]) in the DW factor calculations. A statistical structural disorder in the atomic layers was furthermore incorporated with the help of the SIG2 card (a value of 0.004), followed by a convolution with the experimental resolution of 1.0 eV (using the CORRECTIONS card) in FEFF. In this way it was possible to obtain a good agreement between experiment and computed spectrum, in terms of both absolute values and the

line-shape. Most of the dominant EXAFS features present in the experimental data are reproduced.

4.2.3 Cr K-edge EXAFS

As already mentioned earlier, the energy calibration at the beam line for Cr K-edge XAFS measurements was carried out using a Cr metal foil. Measurements were also performed for α-Cr_2O_3 reference powder.

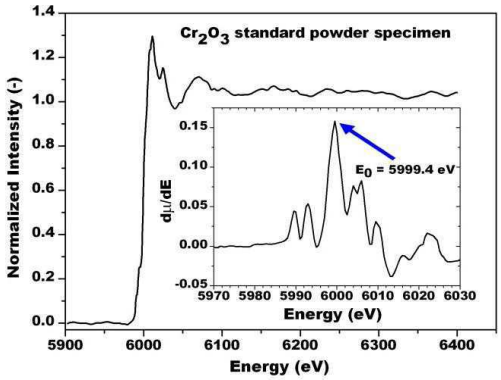

Figure 4.9: Normalized and background removed Cr K-edge absorption spectrum of α-Cr_2O_3 powder reference material. The inset shows the first derivative of the XANES part of the spectrum.

Experimental Cr K-edge absorption edge data, extracted EXAFS oscillation $\chi(k)$ and RDF spectra of fresh and irradiated UO_2 are shown in Figure 4.9. The profile and position of the edges, XANES and EXAFS, FT magnitude curves are all very similar for the two samples examined. These results demonstrate that the environment of the chromium is analogous in the two samples and no major changes take place on the local structure of Cr upon irradiation, at least for an average burn up of ~40 MW d kg^{-1} in the irradiated pellet. The threshold energy at the absorption edge, taken as equal to the maximum value of the inflection point, reveals an E_0 value of 6000 eV for Cr in the fuel samples. This value is 11 eV higher compared to the reference K-edge excitation energy of a corresponding Cr metal foil, and identical to that of the α-Cr_2O_3 reference powder specimen (see Figure 4.9).

This evidences an apparent Cr oxidation state of 3+ in the chromia-doped UO_2. However, a shoulder structure discerned at 5996 eV is also noticed in the XANES region (Figure 4.10b, marked by an arrow). It should be emphasized that the Cr K-edge XANES

spectrum of α-Cr_2O_3 reference powder sample does not possess any such pre-edge feature at 5996 eV, and it is only observed in the XANES data measured from UO_2 grain regions in chromia-doped samples. The origin of this additional structure is still unknown at this time. With regard to literature denotation it may be attributed to the symmetry forbidden 1s → 4s transition of Cr^{2+} [16,17,18], although the exact assignment is irrelevant for this work. This speculation, whether a part of dissolved chromium in UO_2 is reduced, requires in-depth simulations of the measured XANES spectra for confirmation. It will be the subject of future work. Another possibility would be the CrO phase present in chromia-doped UO_2 as an undissolved product, presumably with nanometric crystallite sizes. This should also be evaluated in detail from experimental work. In the following, an analysis of the Cr K-edge EXAFS for the local environment of chromium in the UO_2 matrix is reported.

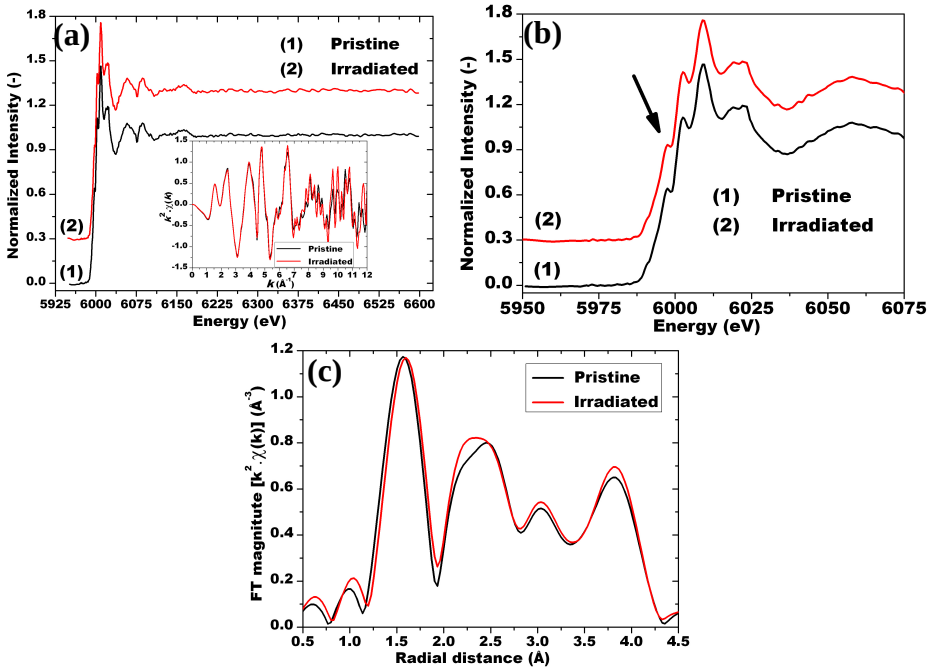

Figure 4.10: (a) Normalized and background removed X-ray absorption spectra at the Cr K-edge measured from the pristine and irradiated Cr_2O_3-doped UO_2 fuels. The plots are vertically shifted to each other for clarity. The inset shows k^2-weighted EXAFS oscillation in overlap mode for the two samples. (b) Zoom of the XANES part is compared for the two samples. The region of interest is marked by an arrow. (c) Results of FT-EXAFS (without any phase-shift correction) preformed in the wave vector region 2–9.5 $Å^{-1}$.

The FT magnitude curves shown in Figure 4.10c illustrate that there are several coordination shells of chromium neighbours. The two RDF spectra of fresh and irradiated

UO_2 have similar features, confirming again the information that the chromium environment is not altered in irradiated UO_2 as compared to its pristine state.
However, the contributions of the individual shells around Cr are not easily resolved with exception of the first shell (Figure 4.10c). The dominant first peak at ~ 1.6 Å stems from the first neighbour O atom shells, and contains no contribution from any Cr–Cr or Cr–U correlation. Group of peaks which have longer radial distances at about 2.4, 3.0 and 3.8 Å are sensitive to the coordination numbers as well as geometry of O, Cr and U neighbours.

The spectral features of these peaks are clearly complicated as they are indistinctly separated because of an overlap between peaks of different O, Cr and U atoms shells including multiple scattering effects. The closeness of both oxygen and chromium shells combined with the effect of static and thermal disorder and the limited *k*-space resolution do not allow visually to resolve all next neighbour shells in the 2 – 4.5 Å region. It may be noted that the FT magnitude curve is not the true radial distribution function, since the EXAFS oscillations are phase shifted by the atomic potentials (absorber and backscatters), so that the positions of the peaks do not correspond to true distances. Usually, the peaks should be shifted by some values of about 0.1 to 0.4 Å, when the data is phase-corrected using a model structure.

For the assignment of different Cr neighbours we have analyzed the radial distribution function of pristine chromia-doped UO_2. Theoretical amplitude envelopes and phase functions were obtained by FEFF simulations based on the reference model of the Cr substituted UO_2 structure. This assumption is based on the proposed solution mechanism involving dissolution of Cr_2O_3 and entry of Cr ions into the UO_2 lattice. For Cr_2O_3 solution in UO_2 chromium is in 3+ oxidation state where as in UO_2 uranium has a 4+ valence state. Therefore, incorporation of chromium atoms into the UO_2 structure requires evolution of charge compensating defects (such as U^{5+}) and/or defect clusters (vacancies, interstitials, Frenkel pairs or Schottky defects, etc.) in order to achieve electro-neutrality in the crystal. For example, the substitutional entrance of Cr ions at regular U sites requires creation of oxygen ion (O^{2-}) vacancies (one vacancy per two Cr atoms to balance the charge), which can then act as charge compensation species to maintain electrical neutrality in the UO_2 lattice. Neutrality can be also maintained by the

presence of a neighboring uranium atom in the 5+ valence state for substitution of U^{4+} by Cr^{3+}. If Cr ions enter interstitially and occupies the central hole locations in the oxygen octahedrons, oxygen interstitials and uranium vacancies could be formed. In the literature, both the substitutional behavior of Cr and/or location of trivalent Cr at the interstitial sites within UO_2 have been discussed [19,20,21,22].The possible structure as well as energetics of point defects and defect-clusters formed in UO_2 due to the added chromia has been also studied theoretically using atomic scale simulations [20,21]. Most of these results highlight the fact that chromium preferentially enters uranium dioxide by substituting regular uranium atoms accompanied by the formation of charged defect clusters. Recently, some works have indicated the precipitation of Cr^{3+} with U^{5+} to form secondary $UCrO_4$ phase from hyperstoichiometric chromia-doped UO_{2+x} and/or formation of other Cr–U–O based compounds such as UCr_2O_6 in combination with Cr^{3+} and U^6+ ions [23,24]. These double oxide compounds in the Cr–U–O system, however, are known to be unstable in reducing atmospheres and at high temperatures above 1000 ^oC [23,25]. Let us also mention that we have not yet identified the presence of any Cr–U-bearing oxides being $UCrO_4$ or UCr_2O_6 from Cr, U and O EPMA quantitative analyses performed on fresh and irradiated chromia-doped UO_2 pellets.

The postulated substitutional model fits well with experimental data what is visible on Figure 4.12a. Using the Fourier transformed EXFAS signal and the chromium-uranium model, it was possible to identify the atomic shells accordingly: the first shell contains oxygen neighbours of the absorbing Cr atom located at ~ 1.6 Å, and the peak at 3.8 Å can be assigned to the second shell, i.e. to the Cr–U single scattering path from FEFF including some multiple scattering processes. Even though the amount of chromium is small (~ 1080 μg/g) in the fuel and the dopant is expected to be in solid solution in the UO_2 grains, the Cr–O distance in the chromia-doped UO_2 differs significantly from the true U–O bond length in standard UO_2 (see Figure 4.10). Importantly, the assignment of distinct FT feature at 2.4 Å requires a Cr–Cr contribution which can not be neglected in the curve-fitting a priori. One way to have a Cr–Cr peak at this distance is to add artificially an intermediate FEFF path in order to get an extra EXAFS signal corresponding to a Cr–Cr scattering path of the photoelectrons. The other alternative

would be to incorporate a second Cr atom in the uranium lattice. Note that the FT peak at 2.4 Å points out a much smaller distance than the shortest U–U distance (of 3.86 Å) in UO_2. Therefore, replacement of two nearest uranium by chromium is not reasonable for the analysis.

We have no unique explanation for the short Cr–Cr signal found in the FT data. We hypothesize that it reflects contributions of some un-dissolved nano-scale Cr_2O_3 particles in chromia-doped UO_2 as already confirmed from EPMA mapping (see Figure 4.11) analyses on fresh fuel materials [12,19]. These ultrafine particles seem to be located in deeper layers below the sample's surface and within the UO_2 volume probed by the incident X-ray beam. Although they are not measured in μ-XRF maps, their contribution to the measured Cr μ-XAFS spectra is obviously detected.

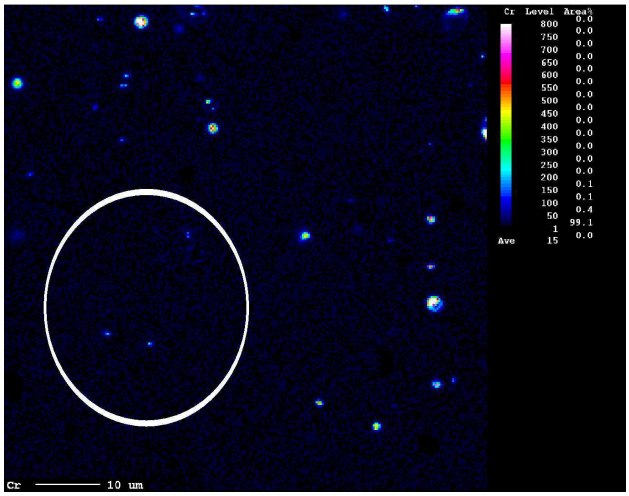

Figure 4.11: High resolution EPMA image showing Cr map in the chromia-doped fresh fuel pellet. A group of the nano-size Cr_2O_3 particles can be observed within the encircled area.

In this prospect, linear combination fits were tested for the EXAFS and FT-EXAFS spectra using FEFF calculated scattering paths of Cr substituted UO_2 and α-Cr_2O_3 reference (Figure 4.12). The crystallographic data of α-Cr_2O_3 together with EXAFS results can be found in the literature [12,26]. It has been noted that the relative intensity of short Cr–Cr and first-shell Cr–O FT-peaks in α-Cr_2O_3 is significantly different in comparison with experimental results shown in Figure 4.10c. Therefore, for resolving the structural parameters, only paths of the single-fold coordinated shortest Cr–Cr pair (2.65 Å) located along the *c-axis* of α-Cr_2O_3 hexagonal unit cell and the outer Cr–O pair at 3.36

Å (three-fold coordinated) have been considered when fitting the radial distribution function in the data reduction process. Due to the limited data set of the wave vector region 2–10 $Å^{-1}$ in our measurements and increased number of variables in linear combination fits, it was necessary to employ highly constrained fits where the Debye-Waller factors of all atoms were empirically adjusted values. Under this approach with restrictions it was possible to get a reasonable agreement between experiment and fitted RDF spectrum, in terms of both absolute magnitudes and the line-shape, with physically sensible values of the CNs and R parameters.

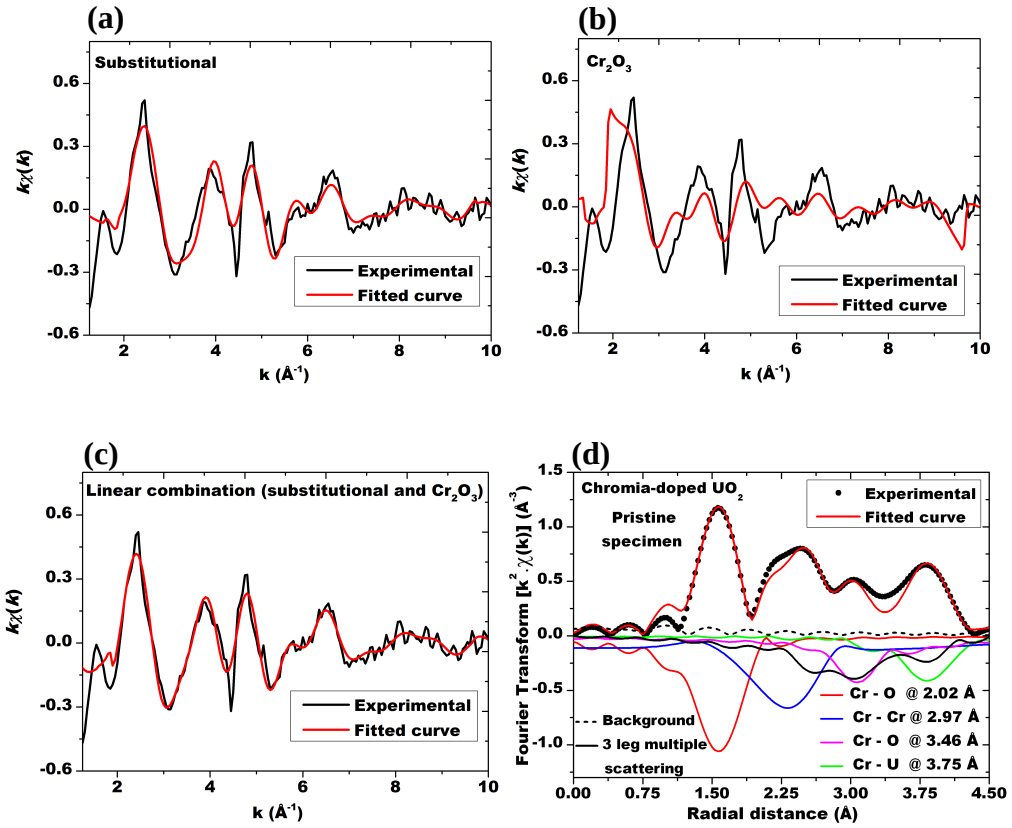

Figure 4.12: Cr K-edge $k\chi(k)$ experimental signal fitted with (a) substitutional model with Cr atom substituting the U site in the UO_2 lattice and (b) the α-Cr_2O_3 crystal phase. (c) Linear combination fit to the spectrum (best fit for 85% substitutional chromium and 15% Cr_2O_3). (d) Individual shells of the central Cr atom fitted in RDF. See the text for details.

An overall fit together with contributions from individual shells is shown in Figure 4.12d. The determined Cr–O and Cr–U average distances in UO_2 are 2.02±0.03 and 3.75±0.04 Å, respectively, with coordination numbers 6.0±0.5 and 11.0±1. This result signifies local lattice distortions around Cr meaning large bond length variations between 0.1 and 0.3 Å

depending on the Cr proximity to those oxygen and uranium atoms, with lower distances than anticipated. Note that the ideal crystallographic values of nearest U–O and U–U distances in uranium dioxide are 2.36 and 3.86 Å, respectively. The decrease of Cr–O and Cr–U coordination as well as bond distance in chromia-doped UO_2 may be explained by the charge compensation effects resulting from Cr^{3+} incorporation at U^{4+} sites and ionic-size differences of cations. At the same time, ab-initio fits based on the FEFF model of the component α-Cr_2O_3 give a number of chromium atoms of 0.8±0.5 at 2.97±0.05 Å and a contribution of 5.0±1 oxygen atoms at 3.46±0.05 Å. These results suggest that although chromium in α-Cr_2O_3 has only one chromium neighbour in the first Cr–Cr shell [26], this contribution to the corresponding EXAFS fit is not negligible. On the other hand, the contribution of chromium and oxygen from Cr_2O_3 precipitates does not result in a very good fit (see Figure 4.12b and Figure 4.12d) in the analysed region of the RDF, even though the structural values determined are sensible. This may be an indication that more than one Cr environment, associated with both Cr and O atoms in those particles, is required in determining the EXAFS pattern that we have measured. Thus, it is difficult to provide any further detail of the Cr environment in undissolved Cr_2O_3 particles in UO_2, except that it exists to a considerable degree of local order as evidenced by the presence of two well-defined expected peaks in the measured radial distribution function.

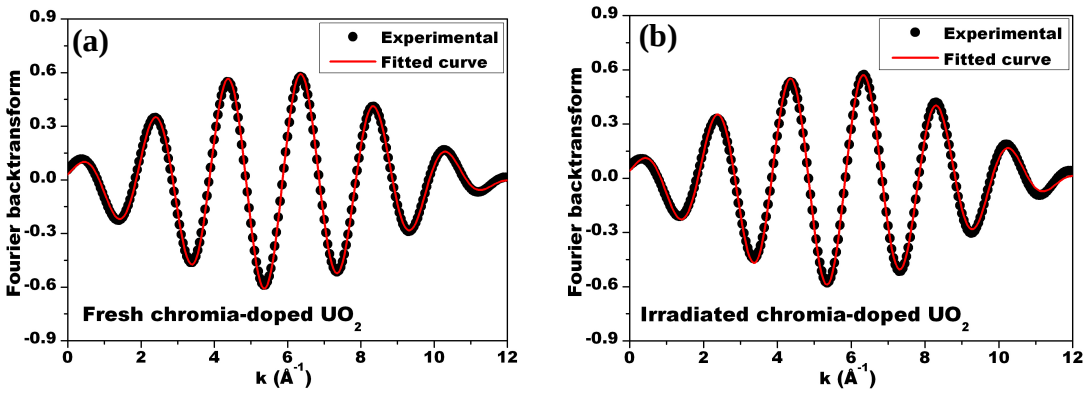

Figure 4.13: Fit to the first-shell (Cr–O) back-transformed EXAFS function (using k^2-weighting) with FEFF model calculations. The Fourier filtering range is 1.1–1.9 Å. The results are shown for (a) pristine UO_2 and (b) irradiated UO_2. The circles and the solid curves show the data and the best fit, respectively.

Further reliability tests have been performed for the coordination parameters obtained from linear combination fits, analyzing only the first-shell signal of the Cr K-edge

EXAFS data. After extraction of the Cr–O shell component from radial distribution functions (see Figure 4.10c), the back-transformed spectra were best-fitted by using R, CN, and σ as free parameters, which is a more realistic approach. The fitted curves represent the experimental data, see Figure 4.13.

The quantitative fittings of the nearest oxygen neighbour in pristine and irradiated UO_2 samples give the average bond lengths and coordination numbers around the chromium atoms, and those results are summarized in Table 4.1. From this table, it can be seen that the dissolved Cr in fresh UO_2 is surrounded by approximately six oxygen atoms at an average distance of 2.02±0.02 Å, which is close to the CN and average Cr–O nearest neighbour bond length of 2.05±0.02 Å, in irradiated UO_2. These findings are direct experimental evidence, which circumstantiates that Cr^{3+} incorporation at U^{4+} sites disrupts both the cation-cation and cation-anion network in the UO_2 lattice and our results provide a quantitative atomic scale information of these processes. It appears that for Cr/U = 0.0012 (and Cr/U = 0.006 in atomic ratio), atomic disorder around Cr become large by the doping, as evidenced by the reduction of CNs and interatomic distance between Cr and first nearest O atoms. But for the irradiated specimen, as this effect has already appeared by the doping, small irradiation effect (at the given burn up) is not observed.

4.3 Intermediate XAFS summary and conclusions

Using the SEM image analysis method the average grain diameter of the Cr_2O_3-doped UO_2 matrix was found to be about 48 μm. The presence of chromia precipitates were evidenced by EPMA. For all precipitates of micrometer sizes analyzed by EPMA the composition was determined to be very close to Cr_2O_3. The mean dissolved Cr concentration in the UO_2 matrix is found to be ≅ 0.07±0.01 wt.% .

The result obtained by EPMA was confirmed by Cr K-edge XANES, which showed only Cr^{3+} as oxidation state in the precipitates. Micro-beam XRD and EXAFS data were evaluated for quantitative results concerning lattice parameter and chromium environment in the precipitates. The lattice parameters (a_H and c_H) were calculated based

on two diffraction peaks, namely (024) and (110) lines of the Cr_2O_3 hexagonal crystal cell. The measured values of the same lattice parameters in the doped material showed a decreasing trend in a_H, an elongation along c_H and hence an increase of axial ratio c_H/a_H, when compared with the unit cell parameters of reference chromium sesquioxide powder. The diffraction peaks assigned to chromia precipitates in UO_2 are rather broader than those of the reference powder. These results suggest that precipitates contain structural disorder and have a distorted lattice structure with respect to that of standard crystalline α-Cr_2O_3. According to the EXAFS results obtained from chromia precipitates data, the first two Cr–O coordination shells are populated with about 4 oxygen neighbors at an averaged distance of 1.90±0.02. This differs from Cr bonding configuration in standard and crystalline α-Cr_2O_3 (six oxygen atoms in octahedral symmetry at an average distance of 1.99 Å). Regarding the metal-metal correlation, the shortest Cr–Cr distance of 2.72 Å, measured from chromia particles is notably longer than the Cr–Cr separation of 2.64 Å evaluated for the standard α-Cr_2O_3. The Debye–Waller factors associated to Cr–O and Cr–Cr bonds in the precipitates are found larger than that of the reference sample. A possible explanation to account for these observations is the apparent sizes of those Cr_2O_3 crystallites that are present as > 1 μm precipitates in the chromia doped UO_2 pellet.

The speciation of dissolved chromium have been studied using XAFS techniques (both XANES and EXAFS) of two Cr_2O_3-doped (0.16 wt.%) UO_2 fuels, a pair of fresh and irradiated (average burn-up of 40 MW d kg^{-1}) materials, using micro-focused synchrotron light. The results provide quantitative insight into the local atomic environment of the dopant chromium in uranium dioxide grains including the oxidation state assignment. According to Cr K-edge μ-XAFS spectra of pristine and irradiated UO_2, the profile and position of the edges, XANES and EXAFS are all very similar. The measured edge positions of the XANES spectra are 6000 eV in both Cr_2O_3-doped UO_2 matrixes furnishing the chemical information of Cr^{3+} oxidation state. These results imply that the local structure around chromium is comparable in the two samples and no major changes take place on the state of Cr due to irradiation, at least up to an average burn-up of ~ 40 MW d kg^{-1} in the irradiated pellet.

To determine the local atomic arrangement of chromium dissolved in the uranium dioxide matrix, the Cr K-edge radial distribution function has been compared with fine structures obtained by ab initio multiple-shells EXAFS simulations using the FEFF code. Although the experimental EXAFS data resemble Cr on substitutional U sites in the lattice, it does not completely match with the theoretically expected EXAFS signal, indicating disordering of atomic arrangement around Cr atoms. A direct comparison of position and intensity of main U–O and Cr–O peaks in the FT allows figuring out the significant structural information contained on it. The fitting results show that the dissolved Cr in as-fabricated UO_2 is surrounded by approximately six nearest neighbor oxygens at an average distance of 2.02±0.02 Å. The closest Cr–O shell of the irradiated sample has a similar coordination number and bond length to that of the pristine chromia doped UO_2. A comparison of these structural values with that of the ideal crystallographic values of nearest U–O shell in uranium dioxide indicates that the bond length contracts and the coordination number decreases in chromia-doped UO_2. We emphasize that these conclusions are still preliminary and confirmation will require further theoretical work, including experimental investigation of ultrathin chromia-doped UO_2 samples where the contribution to micro-beam XAFS spectra emanating from any undissolved dopant product can be neglected in analyzing large grains uranium dioxide microstructure.

4.4 References

1 K.W. Song *et al.*, *Grain size control of UO_2 pellets by adding heat-treated U_3O_8 particles to UO_2 powder*, J. Nucl. Mater. 317 (2003) 204-211.

2 *Standard Test Methods for Determining Average Grain Size*, ASTM-E-112.

3 http://www.crystalimpact.com/match.

4 *Crystal data, Eskolaite (α-Cr_2O_3)*, Mineral data publishing, 2001-2005.

5 Jandel Scientific; PeakFit v2.01.

6 C. ChangFeng *et al.*, *First-principles study of hydrogen diffusion mechanism in Cr_2O_3*, Science China, 54 (2011) 88-94.

7 L. Vegard, *Die Konstitution der Mischkristalle und die Raumfüllung der Atome*, Z. Phys. 5 (1921) 17-26.

8 W.Y. Ching and Y.N. Xu, *First-Principles Calculation of Electronic, Optical, and Structural Properties of α-Al_2O_3*, J. Am. Ceram. Soc. 77 (1994) 404-411.

9 http://cars9.uchicago.edu/ifeffit/feffit.html.

10 J.J. Rehr *et al.*, *Parameter-free calculations of X-ray spectra with FEFF9*, Phys. Chem. Chem. Phys., 12 (2010) 5503-5513.

11 A.H. Hill *et al.*, *Crystallographic and magnetic studies of mesoporous eskolaite, Cr_2O_3*, Microporous and Mesoporous Materials 130 (2010) 280-286.

12 G. Kuri *et al.*, *Local atomic structure of chromium bearing precipitates in chromia doped uranium dioxide investigated by combined micro-beam X-ray diffraction and absorption spectroscopy*, J. Nucl. Mater. [2014 submitted].

13 C. Degueldre *et al.*, *Plutonium–uranium mixed oxide characterization by coupling micro-X-ray diffraction and absorption investigations*, J. Nucl. Mater. 416 (2011) 142-150.

14 S.D. Conradson *et al.*, *Local structure and charge distribution in the UO(2)-U(4)O(9) system*, Inorg. Chem. 43 (2004) 6922-6935.

15 N.M. Butt *et al., Compilation of temperature factors of cubic compounds,* Acta Cryst. A49 (1993) 171-174.

16 A.J. Berry and H.St.C. O'Neill, *A XANES determination of the oxidation state of chromium in silicate glasses,* American Mineralogist 89 (2004) 790-798.

17 http://ftp.esrf.eu/pub/UserReports/38684_A.pdf.

18 http://ftp.esrf.eu/pub/UserReports/40325_A.pdf.

19 A. Leenaers *et al., On the solubility of chromium sesquioxide in uranium dioxide fuel,* J. Nucl. Mater. 317 (2003) 62-68.

20 Cardinaels *et al., Chromia doped UO_2 fuel: Investigation of the lattice parameter*. Nucl. Mater. 424 (2012) 252-260.

21 S.C. Middleburgh *et al., Solution of trivalent cations into uranium dioxide,* J. Nucl. Mater. 420 (2012) 258-261.

22 K.S Kim *et al., Sintering of a Mixture of UO_2 and Gd_2O_3 Powders Doped with Cr_2O_3-SiO_2,* J. Korean Nucl. Soc. 33 (2001) 386-396.

23 M.W.D. Cooper *et al., Formation of (Cr, Al)UO_4 from doped UO_2 and its influence on partition of soluble fission products*, J. Nucl. Mater. 443 (2013) 236-241; and references therein.

24 M. Fraczkiewicz, *Dopage au chrome du dioxide d'uranium: modifications physiques induites,* Ph.D. Thesis, University of Grenoble, 3rd June 2010.

25 S. Sampath *et al., Thermal behaviour of co-precipitated mixtures of chromium(III) and uranium(VI),* Thermochimica Acta 55 (1982) 249-251.

26 A.N. Blacklocks *et al., An XAS study of the defect structure of Ti-doped α-Cr_2O_3,* Solid State Ionics 177 (2006) 2939-2944.

Chapter 5: Analysis of Fission Gas using EXAFS

5.1 Krypton investigations

EPMA results of Pu and some of the selected FP elements, obtained from standard and Cr_2O_3-doped UO_2 are shown in Figure 5.1. Due to the higher burn-up (more FPs) and the lower temperature (less diffusivity), more Xe is present at the periphery. Comparing the two irradiated fuels also the insignificant difference regarding the amount of xenon of doped and standard fuel at the rim region can be observed.

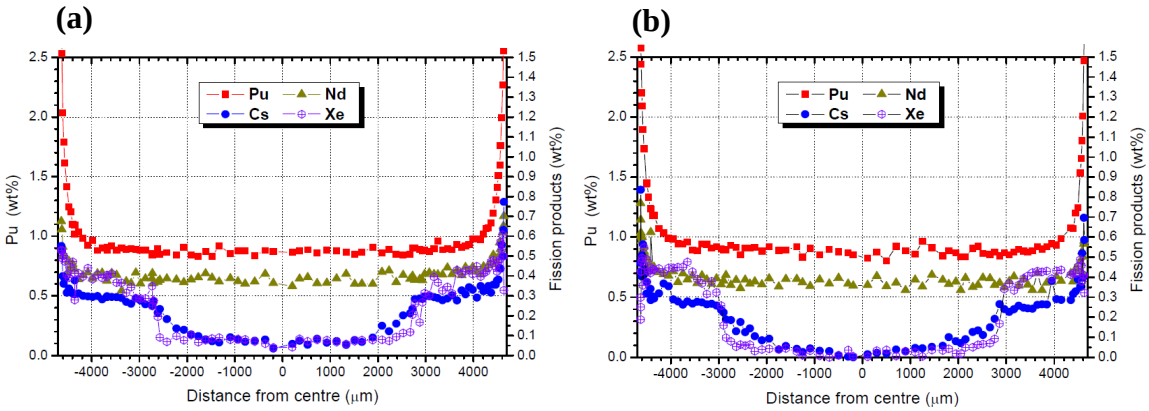

Figure 5.1: EPMA fluorescence spectrum of an uranium pellet. (a) standard (b) doped fuel [1].

By consequence the samples for which fission gas analysis was made were from the pellet rim. As Xe K line is not detectable at the microXAS beamline and the L line interferes with signals coming from other fission products, the measurements were focused on krypton. The XAFS spectra of the Kr K-edge collected from standard and doped fuel particles are comparable. They show well defined XAFS oscillations after a weak white line (Figure 5.2a&b). Spectra taken from various particles are also comparable. Scans over the biggest particles do not reveal any systematic change of the spectra during successive recording. If a significant white line is not observed in the XAFS spectra of the noble gases (it is 'gases' because a mixture of fission gases is assumed to be in bubbles) at room temperature, pressure oscillations are also absent in the near edge region. After spectrum background subtraction and normalization the edge energy was found by derivation to be at 14326 eV in the standard irradiated fuel and at

exactly the same energy in the chromia doped fuel. These data allow calculations in the *k* space (Figure 5.2b).

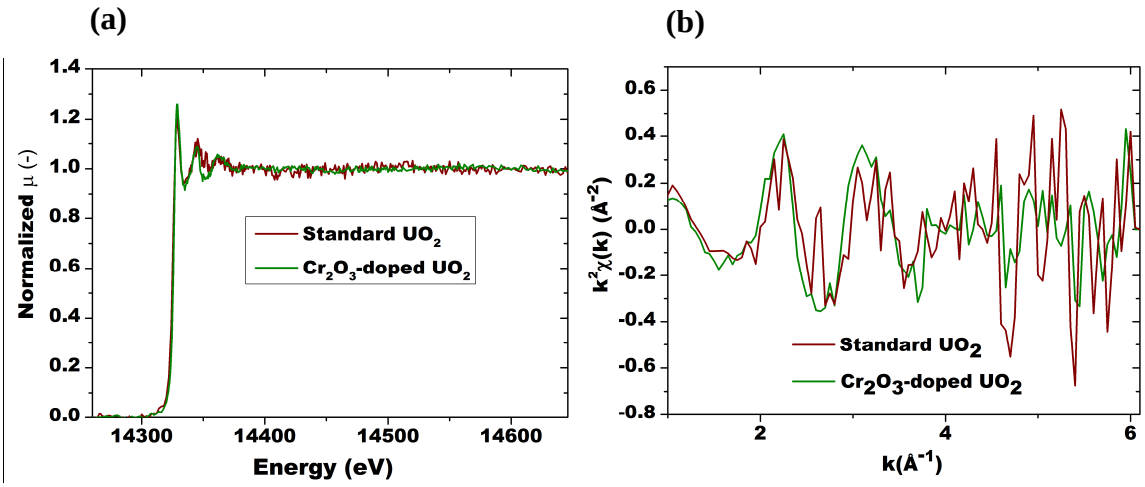

Figure 5.2: (a) Kr K-edge XAFS spectra measured from standard and doped UO_2 fuels. (b) The k^2-weighted EXAFS function extracted from the data of two samples is shown.

The recorded spectra contrast with the literature based XAFS spectra of the noble gases at room temperature and atmospheric pressure. As reported in the literature, the white line and oscillations appear when the gas pressure or density increases. Two possible hypotheses may be formulated to explain the observed XAFS features. First, partial dissolution of Kr atoms in the UO_2 matrix is suggested, however, the concentration of these species is rather limited. Second, krypton local density increases in formed nanophases. In the first case, krypton atoms are surrounded by oxide ions. In the second case one assumes that first neighbours are other fission gases (i.e. Xe, Kr, He…etc.). The backscattering amplitude functions for oxygen and noble gases are different. For oxygen as a neighbour, backscattering amplitudes are damped more rapidly than for xenon or krypton. The absence of rapid decrease of the EXAFS signal (Figure 5.2b) testifies the lack of the oxide neighbours and supports the second assumption [2]. However, it should be noted that recorded EXAFS signal contains average information on the krypton local environment. Consequently, a small part of the signal obtained from dissolved Kr in the fuel matrix cannot be excluded. A similar conclusion about the krypton neighbour can be obtained taking into account that ^{235}U fission generates about ten times more Xe than Kr [3]. The dilution effect implies that Xe most probably is the next neighbour of Kr in any

cluster, nano- bubble or phase containing the fission gases. Consequently, the analysis focuses on the presence of Xe only in the surrounding of Kr.

It should be noticed also that the Xe/Kr atomic ratio of the generated fission gas in a fuel is determined by various fuel design specifications and irradiation conditions such as the initial concentration of ^{235}U, weight of the fuel, neutronic flux spectrum, irradiation duration, operation history of the reactor, and the analysis date, which can induce some variations even for fuels with the same initial enrichment and burn-up [4].

The occurrence of other rare gases is negligible. Some of the fuel vendors for instance are using for manufacturing conditions an atmosphere of 4% hydrogen in argon, but the residual argon fraction has been found to be restricted in spent fuel. Gas release from the nuclear fuels out of pressurized closed pores produced by autoclave anneals has been studied by Thermal Desorption Spectrometry [5]. This release occurred in a narrow temperature range between about 1000 and 1500 K for UO_2. Presence of hydrogen was consequently negligible. Occurrence of radiogenic helium is also limited in a spent fuel that has not been aged for 1000 years.

The Fourier transform of the XAFS signal recorded during the experiment was performed in the k range from 1.5 to 5 $Å^{-1}$.

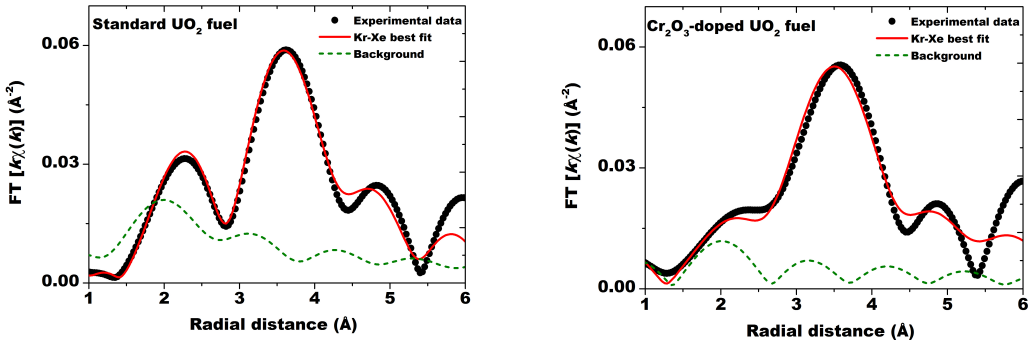

Figure 5.3: Fourier transformed EXAFS of krypton K-edge XAFS data for standard and doped fuels fitted with Xe fcc lattice with one Xe atom substituted by Kr per unit cell. Conditions: *k* window from 1.5 to 5 $Å^{-1}$, phase corrected.

The XAFS data $k^2\chi$ vs. *k* between doped and un-doped fuel confirm a larger degree of correlation for Kr in the doped fuel compared to standard fuel; the data of the latter exhibits more noise.

After Fourier transform (FT) of the signal significant differences between doped and standard fuel are observed (see Figure 5.3). The nearest neighbour distance for the doped fuel (3.59 Å) is smaller than for the standard fuel (3.66 Å). In addition, the amplitude of the FT signal is higher for the doped fuel, suggesting that in average more gas atoms (besides Kr probably mainly Xe) are hosted in the FG cluster in the case of the Cr_2O_3-doped UO_2 fuel.

The internal bubble pressure can be revealed with the help of recorded EXAFS signals. The comparison of the absorption data recorded for both materials with the spectra reported by DiCicco *et al*. [6] reveals a very high krypton-xenon density. Obtained oscillations in the absorption spectra are different for gas and are more comparable with the liquid or solid state of krypton. From the peaks shape of our recorded data the predicted pressure seems to lie above the critical point for liquid-solid phase transition, which is 0.801 GPa at 292 K [7].

The effect of the pressure on the X-ray absorption spectroscopy on solid krypton up to 20 GPa has been reported by Polian *et al.* [8]. This work was completed by the study of Lecerda *et al.* [9] who reported about the local environment of Kr atoms implanted into an amorphous carbon matrix; noble gas atoms were trapped under different internal pressure (intrinsic stress) ranging from 1 up to 12 GPa. The effect of the internal pressure on the implanted Kr atoms subject to the highly strained environment of the carbon matrix was investigated. The analysis of X-ray near edge spectroscopy shows an evident increase of the white line for both gases as the stress increases. This result is indicative of clustering of the implanted Kr atoms. The analysis of the Fourier transformed EXAFS results for Kr atom indicates an decrease of the first neighbour distance to about 2.8 Å at a pressure around 10 GPa with increasing compressive stress. Since due to assumption mentioned above regarding the Xe as a next Kr neighbour the work of Garcia *et al*. [10]as well as Martin *et al*. [11] on Xe in UO_2 must also be accounted for; a Xe–Xe distance of about 3.5–4 Å (pressure dependent) was found. The Kr–Xe distance estimated from the rare gas van der Waals (VDW) radii and the experimental data are compared in Table 5.1. An octahedral configuration for the Xe next neighbour atoms is suggested.

Table 5.1: Estimation of the Kr – Xe properties and comparison with gas atom radii [12].

Noble gas parameter	*CN* = 12	*CN* = 6	Experimental values (±0.03)*	
			Standard	Doped fuel
Kr VDW radius *r* (Å)	2.02	1.78		
Xe VDW radius *r* (Å)	2.16	1.96		
Kr – Xe distance *R* (Å)	4.18	3.74	3.66	3.59

* Estimate from the XAFS data measurements.

Using inter-atomic distances obtained for the standard and Cr_2O_3-doped UO_2 fuel the approximation of the atomic density can be calculated. The density in number of atoms per unit volume may be estimated in an fcc structure model with a Xe atom substituted by one Kr [13]. This structure for a Kr–Xe distance of ~3.66 Å (standard UO_2) and ~3.59 Å (doped fuel) corresponds to a density of around 28.8 atoms nm^{-3} and 30.6 atoms nm^{-3} respectively. Following the work reported by DiCicco *et al*. [6] regarding inter-atomic distances of compressed solid Kr the pressure of such densities can be predicted. As found for densities from 28.8 to 32.6 nm^{-3} the corresponding pressure is located between 2.0 GPa and 4.0 GPa respectively. However, considering xenon as nearest neighbour, also the work of Asaumi [14] should be taken into account. In his report the estimation of xenon bubble internal pressure was done using the Birch–Murnaghan type equation of state (EOS) for solid xenon at around 0 K [14]:

$$P = \frac{3}{2} B_0 \left[\left(\frac{V_0}{V} \right)^{7/3} - \left(\frac{V_0}{V} \right)^{5/3} \right] \left\{ 1 + \frac{3}{4} \left(B_0' - 4 \right) \left[\left(\frac{V_0}{V} \right)^{2/3} - 1 \right] \right\} \tag{5.1}$$

where:

B_0, B_0'- bulk modulus

V_0- molar volume (T=0, P=0)

V- molar volume

Pressure quantification using the same EOS was also reported by Martin *et al.* [11] and by Garcia *et al.* [10]. Similar investigations were performed with data of this work. However, due to changed conditions there are several corrections that need to be done. The main difference is the volume of the unit cell itself. It is not made of homogeneous

material anymore and substituting one Xe atom by krypton will decrease the size of the molar volume (V_0). The next correction is the change in the bulk modulus value. It was reported already by [15,16] that the bulk modulus for Kr fcc is smaller compared to the Xe. The modulus difference between Xe and Kr fcc is about ~8%. Compared to the discussion on the changes in the atomic radii (Table 5.1), also the difference in absolute molar volume can be predicted and it may vary between ~2-9 %. The results for the pressure as a function of inter-atomic distances are compared and presented in Figure 5.4.

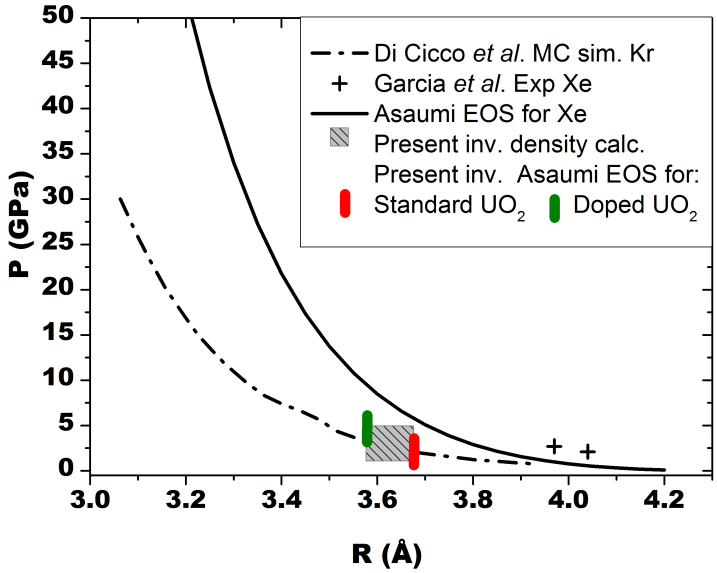

Figure 5.4: The apparent pressure as a function of inter-atomic distance.

As can be seen the calculated pressure for standard as well as doped fuel vary between the theoretical calculations for Xe and Kr fcc structure and is consistent with the experimental data. The measured and calculated pressure of krypton collected from chromia-doped fuel is a bit higher than that for the standard one. This result could be explained by the larger amount of FG atoms retained in the Cr_2O_3-doped UO_2 material. However, this extremely inter-atomic distance sensitive calculation is strongly dependent on the sample preparation method.

It must be noted that the way of how the samples had been prepared for the present studies (2.2 Sample preparation method) is not optimal. Under the peeling conditions most of the fission atoms coming from larger bubbles are lost and the signal collected may come only from the highly pressurized nm-size aggregates. Additionally, although the investigated grains were coming from the same region of interest (periphery of the

pellet) the original radial position of the grains could be a little different. This may cause a small difference in the local burn-up and hence in the quantity of produced krypton in both samples.

5.2 Intermediate fission gas EXAFS summary and conclusions

The krypton X-ray absorption signal has been collected for both irradiated specimens; standard uranium dioxide and chromia-doped fuel. Fourier transformed EXAFS signals revealed the nearest neighbour positions [~3.66 Å (standard UO_2) and ~3.59 Å (doped fuel)]. The analysis of the fcc structure density and pressure of the gas bubbles was based on the presence of Xe only in the surrounding of Kr.

Following previous studies described in literature the densities in number of atoms per unit volume for standard and doped fuel were estimated and compared with the results of internal pressure calculations obtained using the Birch–Murnaghan type EOS. The results show a slightly higher density (also pressure) in case of the chromia-doped fuel. This can be explained as a consequence of the larger amount of FG atoms retained in the Cr_2O_3-doped UO_2 material compared to standard one. The obtained results were presented and compared with the literature theoretical calculations performed for pure Xe and Kr crystals and experimental data of xenon implanted uranium dioxide specimens.

It would not be correct to say that the measured pressure comes exclusively from the μm-sized bubbles that are found by the EPMA investigations. Due to the sample preparation used and the size of the particles – also being in the μm range – practically all fission gas has been released. It can be assumed that only in some rare cases intact bubbles remain in the ultra thin samples. However, the measured XAFS signal implies the close vicinity of gas atoms. If they are not in the μm-sized bubbles, they must be either quasi dissolved in the bulk or in nano-sized aggregates. These would not be visible with the EPMA. Here, transmission electron microscopy (TEM) could help to obtain more information. It is a speculation to state that the fission gas retention ability of doped fuel works on a scale below the bubbles sizes measured in the typical and standard examinations like EPMA.

5.3 References

1 M. Martin and R. Restani, *Personal communication*.

2 R. Wulf *et al., Structural environment of krypton dissolved in vitreous silica,* Am. Mineral, 84 (1999) 1461-1463.

3 S. D. Park *et al., The measurement of compositions and the isotopic distribution of released fission gas in the fuel rods of pressurized water reactors (PWR) of Korea,* J. Radioanal. Nucl. Chem. 284 (2010) 287-295.

4 S.D. Park *et al., Distribution characteristics of fission gas along the axial direction for an irradiated fuel rod of a pressurized water reactor (PWR),* J. Radioanal. Nucl. Chem. 298 (2013) 679-689.

5 P. Bailey *et al., Gas release from pressurized closed pores in nuclear fuels*, J. Nucl. Mater., 158 (1988) 19-24.

6 A. DiCicco *et al., High-pressure EXAFS measurements of solid and liquid Kr*, Phys. Rev. B, 54 (1996) 9086-9098.

7 R. K. Crawford and W. B. Daniels, *Experimental Determination of the P-T Melting Curves of Kr, Ne, and He,* J. Chem. Phys. 55 (1971) 5651-5656.

8 A. Polian, *et al., X ray absorption spectroscopy on solid krypton up to 20 GPa*, Physica B, 158 (1989) 525-526.

9 R.G. Lacerda *et al.*, EXAFS study of noble gases implanted in highly stressed amorphous carbon films, J. Non-Crystalline Solids, 299–302 (2002) 805-809.

10 P. Garcia *et al., A study of xenon aggregates in uranium dioxide using X-ray absorption spectroscopy,* J. Nucl. Mater., 352 (2006) 136-143.

11 P. Martin *et al., XAS characterisation of xenon bubbles in uranium dioxide*, Nucl. Instrum. Methods B, 266 (2008) 2887-2891.

12 Y. Zhang and Zh. Xu, *Atomic radii of noble gas elements in condensed phases*, Am. Mineralogist, 80 (1995) 670-675.

13 C. Degueldre *et al., X-ray fluorescence and absorption analysis of krypton in irradiated nuclear fuel: an analytical approach,* Nucl. Instr. Meth. B [2014 submitted].

14 K. Asaumi, *High-pressure x-ray diffraction study of solid xenon and its equation of state in relation to metallization transition*, Phys. Rev. B 29 (1984) 7026-7029.

15 J.H. Kim *et al.*, *High-pressure equations of state of krypton and xenon by a statistical mechanical theory*, J. Chem. Phys. 91 (1989) 3133-3147.

16 H. Shimizu *et al.*, *High-pressure elastic properties of liquid and solid krypton to 8 GPa*, Phys. Rev. B 57 (1998) 230-233.

Chapter 6: Conclusions

This doctoral thesis is focused on studying the atomic scale structural modifications of the lattice structure in nuclear oxide fuel during irradiation. The experimental investigation has been undertaken for a set of fresh and irradiated standard UO_2, Cr_2O_3-doped UO_2 and $(U,Pu)O_2$ MOX fuels; the irradiated fuel was procured from commercial nuclear reactors in Switzerland. One of the main objectives of this work was to investigate the atomic scale environment of chromium as the dopant in chromia-doped UO_2 fresh fuel and the influence of irradiation on chromium in spent fuels. From the bibliographical review, it was found that the basic mechanism of chromium incorporation in the UO_2 lattice still remained unclear despite extensive efforts. Most importantly no information was available about the atomic scale structure of the dopant chromium in irradiated chromia-doped spent fuel. There are still a lot of open questions on the nature and configuration of structural defects formed during irradiation in chromia-doped fuels and the role of chromium on fuel structural evolution as well as the nucleation and growth of fission gas bubbles, which are all critical in affecting the doped-fuel performance during reactor operation. The basis of understanding these phenomena is the atomic scale structural development in the fuels. For this reason, a series of experiments based on micro-probe X-rays synchrotron light were performed, and modelling of the experimental data was carried out.

The main results and their interpretation are summarized as follows:

- The evolution of the UO_2 lattice parameter was observed in all irradiated fuel specimens. The measured lattice parameters were compared with theoretical predictions. In the data analysis, the role of Cr as a dopant and the impact of several fission product elements were considered. The trends observed are that in fresh UO_2 the lattice contracts as a result of Cr_2O_3 doping, but expands in irradiated materials. All irradiated samples behave in a similar manner (at the given burn-ups) with UO_2 lattice expansion occurring upon irradiation, where any Cr induced effect seems insignificant and irradiation induced defects prevail.

- Elastic strain energy densities in the irradiated fuels were evaluated based on the UO_2 crystal lattice strain and non-uniform strain. The main origin of the strain both for undoped and chromia-doped specimens is considered to be the same, i.e. irradiation induced defects in the UO_2 crystallites. The lattice strain for the chromia-doped UO_2 is about 0.4%, which is not remarkably different from the corresponding result of standard UO_2 specimens. This result confirms that there is no detrimental (like irradiation induced damage) effect of chromia doping. The structural behaviour of chromia-doped and standard UO_2 is rather similar at the average pellet burn of 40 MW d kg^{-1}.
- The magnitude of the measured strain in all irradiated fuel specimens is already in the polygonization regime of UO_2. As a consequence, subdivision of UO_2 grains occurs, and this has been clearly observed in the experiments and quantified. Fuel polygonization is dependent on local burn-up: in fresh fuels no polygonization is found, in the centre region of irradiated pellets some polygonization is detected. The effect is more pronounced in the outer or rim area of irradiated pellets. A quantitative determination of sub-grains per UO_2 grain has been possible through the thesis work.
- The presence of chromia precipitates, originated from excess out of solid solution of initially added chromia powder, was evidenced by EPMA in chromia-doped UO_2 fresh fuel pellet and easily detected by micro-focused synchrotron light. The composition of those particles was determined by EPMA to be very close to Cr_2O_3. Synchrotron XAS results showed Cr^{3+} as oxidation state in the precipitates. According to the XRD results, the chromia precipitates in UO_2 contain structural disorder and have a distorted lattice structure as compared to that of standard and crystalline α-Cr_2O_3 hexagonal crystal unit cell. EXAFS analysis has revealed that the first two Cr–O coordination shells are populated with about 4 oxygen neighbours at an averaged distance of 1.90±0.02 in chromia precipitates. This differs from Cr bonding configuration in standard and crystalline α-Cr_2O_3 (six oxygen atoms in octahedral symmetry at an average distance of 1.99 Å). Regarding the metal-metal correlation, the shortest Cr–Cr distance of 2.72 Å, measured from chromia particles is notably longer than the Cr–Cr separation of 2.64 Å evaluated for the standard α-Cr_2O_3. A possible explanation to account for all these observations is the apparent sizes of those Cr_2O_3 crystallites, grown on cooling to create

second phase inclusions and present as > 1 μm precipitates in the chromia doped UO_2 pellet.

- The local atomic structure of chromium in chromia-doped uranium dioxide grains has been assessed. For both fresh and spent fuels, chromium has a formal oxidation state of Cr^{3+} in the UO_2 grains. The EXAFS experiments have clearly demonstrated that the local structure around chromium is analogous in the fresh and irradiated chromia-doped UO_2 and no major changes take place on the state of Cr due to irradiation, at least up to an average burn up of ~ 40 $MWdkg^{-1}$ in the irradiated pellet. This is valuable information for the in-service performance and behaviour of chromia-doped fuel in the reactor. With a postulated chromium-uranium substitutional, the experimental XAS data was analyzed in details. There is a prominent reduction in the adjacent Cr–O bond length of about 0.3 Å in chromia-doped fresh UO_2 compared to the ideal U–O bond length in standard uranium dioxide that would be expected due to the change in effective Coulomb interactions resulting from replacing U^{4+} by Cr^{3+} and their ionic-size differences. The contraction of shortest Cr – U bond is ~ 0.1 Å relative to the U – U bond length in bulk UO_2. It is established in the present work that Cr incorporation in UO_2 disrupts both the cation-cation and cation-anion network in the UO_2 lattice and our results provide quantitative atomic scale information of these processes.
- The X-ray absorption data of krypton in irradiated standard uranium dioxide and chromia-doped fuel has been successfully achieved. Obtained by Fourier transformed EXAFS the nearest neighbour positions for both irradiated samples were used to calculate the atom per unit cell density and corresponding internal pressure. The results of pressure obtained for standard UO_2 and Cr_2O_3-doped fuel are compared and discussed. For the two investigated samples the obtained pressure is higher for the chromia-doped fuel.

6.1 Outlook

The use of synchrotron radiation to analyze doped and undoped fuel has revealed structural as well as chemical information about the doping element and fission products. Although there are new findings and may be valuable results, ideas persist to continue the work. In order to refine the results and the quality of the sample improvements are needed. The suggestions and recommendations to improve possible further experimental work as well as an opening of the scope are given below:

- **Sample preparation method**. Due to the activity limits at the synchrotron beamlines one of the most difficult part of the thesis was sample preparation. In order to obtain a better quality of spectra additional investigations in the sample preparation method are required. One of the possible ideas that could optimize the volume, shape as well as the quality (polishing) of obtained irradiated samples is the sample preparation performed by means of focused ion beam (FIB). This method combined with EPMA could also serve to procure samples consisting of material with purely dissolved Cr in the UO_2 matrix. FIB would also help to investigate the fission gas bubbles. Having the possibility to determine the cutting area of the pellet would allow collecting specimens with chosen fission bubbles. It would allow also collecting small samples with different sizes and to analyse the bubble gas pressure as a function of size of investigated volume. This could then give a hint about the nature of gas inclusions outside the bubbles.
- **Additional investigation**. The current investigations regarding the micro-structural modifications as a function of burn-up are based on results obtained from Cr_2O_3-doped UO_2 fuels irradiated up to ~40MWd kg^{-1}. A new research work could be done involving chromia-doped and standard fuel irradiated up to higher burn-up where the atomic scale modifications are more pronounced. Comparing the same type of doped fuel irradiated to a higher burn-up would also help to further clarify and confirm the postulates and discussions presented for lattice changes, polygonization and state of dopant as well as internal pressure of fission gas aggregates. A principal investigation of formation mechanism(s) of high burn-

up structure, in doped or undoped fuel, would also be possible. Another, complete new field would be the analysis of fuel under experimentally performed fast power ramp conditions. Collaboration with respective institutes would be of advantage.

Curriculum vitae

PERSONAL INFORMATION

- Nationality: Polish
- Date and place of birth: 26. 09. 1983, Końskie, Poland
- Current E-mail address: cyprian.mieszczynski@psi.ch

EDUCATION

2010 - present	Université Paris-Sud 11, France. Field of study: Nuclear fuels. Title of the doctoral thesis: Atomic Scale Structural Modifications in Irradiated Nuclear Fuels.
2005 - 2010	Jan Kochanowski University of Humanities and Sciences in Kielce, Poland. Field of study: Physics. Specialization: Physics and Computer Sciences. Title of the master thesis: Characterization of X-ray fluorescence detectors at ID21 x-ray microscopy beamline of European Synchrotron Radiation Facility (ESRF), France.

EXPERIENCES

2010 - present	Employed as a PhD student in the Nuclear Energy and Safety Department, Laboratory for Nuclear Materials at Paul Scherrer Institute (PSI), Switzerland under the supervision of Prof. Eric Simoni (Uni. Paris-Sud 11) and Dr. Goutam Kuri (PSI).
2010	Three months as a trainee in the team of ID21 X-ray microscopy beamline of European Synchrotron Radiation Facility, France under the supervision of Dr. Jakub Szlachetko.

.LANGUAGES

- Polish: native
- English: good
- French: basic
- German: basic

List of presentations

1. C. Mieszczynski, *Synchrotron-based μ-XRD investigation of irradiated uranium-plutonium mixed oxide fuel*, Les Journées des Doctorants JDD (28-29.03.2011, Paris-Orsay, France)-poster presentation.

2. C. Mieszczynski, C. Degueldre, G. Kuri, C. N. Borca, *Investigation of uranium-plutonium mixed oxide fuel by means of synchrotron based micro-beam X-ray diffraction*, E-MRS 11 conference (09-13.05.2011, Nice, France)-poster presentation.

3. C. Mieszczynski, *Investigation of irradiated MOX fuel by micro X-ray diffraction*, PSI NES PhD day, (08.06.2011, Villigen, Suisse) –poster presentation.

4. C. Mieszczynski, G. Kuri, C. Degueldre, J. Bertsch, M. Martin, C.N Borca, *Structural modifications in irradiated Cr_2O_3-doped UO_2 fuel investigated using μ-XRD and μ-XAFS spectroscopy*, SLS User Meeting 2011 JUM@P'11 (15-16.09.2011, Villigen, Switzerland)-poster presentation.

5. C. Mieszczynski, E. Simoni, G. Kuri, *Atomic scale structural modifications in irradiated nuclear fuels*, Les Journées des Doctorants JDD (05-06.04.2012, Paris-Orsay, France)-oral presentation.

6. C. Mieszczynski, G. Kuri, C. Degueldre, M. Martin, J. Bertsch, C.N Borca, D. Grolimund, Ch. Delafoy, E. Simoni, *Atomic scale structural changes in an irradiated nuclear fuel***,** SLS symposium, (08.05.2012, PSI, Villigen, Suisse) -oral presentation.

7. C. Mieszczynski, G. Kuri, C. Degueldre, M. Martin, J. Bertsch, C.N Borca, D. Grolimund, Ch. Delafoy, E. Simoni, *Irradiation effects on the lattice parameter of chromia-doped UO_2 investigated by micro-beam X-ray diffraction*, E-MRS 12 conference, (14-18.05.2012, Strasbourg, France) -oral presentation.

8. C. Mieszczynski, *Micro-XRD studies of irradiated chromia-doped UO_2 fuels*, PSI NES PhD day, (13.06.2012, Villigen, Suisse) -oral presentation.

9. C. Mieszczynski, E. Simoni, G. Kuri, *Atomic scale structural modifications in irradiated nuclear fuels analyzed with synchrotron radiation*, Les Journées des Doctorants JDD (27-28.03.2013, Paris-Orsay, France)-poster presentation.

10. C. Mieszczynski, *State of dopant in large grain chromia-doped UO_2 fuel*, PSI NES PhD day, (22.05.2013, Villigen, Suisse) -oral presentation.

11. C. Mieszczynski, G. Kuri, M. Martin, J. Bertsch, *State of chromium in chromia doped uranium dioxide fuels*, SLS User Meeting 2013 JUM@P'13 (18-20.09.2013, Villigen, Switzerland)-poster presentation.

List of publications

- **C. Mieszczynski**, C. Degueldre, G. Kuri, J. Bertsch, C.N. Borca, *Investigation of irradiated uranium-plutonium mixed oxide fuel by synchrotron based micro X-ray diffraction*, Prog. Nucl. Energ. 57 (2012) 130-137.
- C. Degueldre, C. Cozzo, M. Martin, D. Grolimund, **C. Mieszczynski,** *Americium characterization by X-ray fluorescence and absorption spectroscopy in plutonium uranium mixed oxide*, J. Solid State Chem. 202 (2013) 315-319.
- **C. Mieszczynski**, G. Kuri, C. Degueldre, M. Martin, J. Bertsch, C.N. Borca, D. Grolimund, Ch. Delafoy, E. Simoni, *Irradiation effects and micro-structural changes in large grain uranium dioxide fuel investigated by micro-beam X-ray diffraction*, J. Nucl. Mater. 444 (2014) 274-282.
- C. Degueldre, **C. Mieszczynski**, C.N. Borca, D. Grolimund, M. Martin, J. Bertsch, *X-ray fluorescence and absorption analysis of krypton in irradiated nuclear fuel: an analytical approach*, Nucl. Instr. Meth. B [2014 accepted].
- G. Kuri, **C. Mieszczynski**, M. Martin, J. Bertsch, Ch. Delafoy, *Local atomic structure of chromium bearing precipitates in chromia doped uranium dioxide investigated by combined micro-beam X-ray diffraction and absorption spectroscopy* J. Nucl. Mater. 449 (2014) 158-167.
- **C. Mieszczynski**, G. Kuri, J. Bertsch, M. Martin, C. N. Borca, Ch. Delafoy, E. Simoni, *Micro-beam X-rays absorption spectroscopy study of chromium in large grain uranium dioxide fuel* J. Phys. Condens. Matter. [2014 accepted].

Appendix: Résumé de thèse en français

La conjonction et l'analyse des résultats issus d'essais expérimentaux et de la modélisation des combustibles nucléaires irradiés sont nécessaires pour comprendre l'évolution de leur structure à l'échelle atomique. L'objectif principal de ce travail de thèse porte sur l'étude expérimentale à l'échelle atomique des changements micro-structurels qui surviennent dans les grains de combustibles de dioxyde d'uranium (UO_2) dopés au sesquioxyde de chrome et dans des grains relativement plus grands par rapport aux grains du combustible standard. Il est par conséquent important de déterminer l'impact du chrome sur le comportement sous irradiation de produits de fission spécifiques (gaz nobles à la fois solubles et insolubles) sur l'évolution structurale de la matrice du combustible irradié. Une partie du travail de thèse concerne aussi les modifications structurelles à l'échelle atomique d'un combustible MOX $(U,Pu)O_2$ irradié pour comprendre les changements structurels du combustible à très haut taux de combustion. L'irradiation neutronique et les produits de fission générés influencent conjointement la structure du réseau cristallographique du dioxyde d'uranium. Par conséquent, afin de pouvoir prédire le comportement du combustible au niveau macroscopique, il devient très important de connaître les variations structurelles et le comportement des produits de fission au niveau nanoscopique et atomique. Le point clé est que les techniques modernes issues des microsondes à rayonnement synchrotron (la spectroscopie d'absorption de rayons X et de diffraction de rayons X), appliquées dans ce travail de thèse, ont la capacité de sonder expérimentalement les structures physico-chimiques de l'échelle nanoscopique à l'environnement atomique.

Abréviations:

EPMA	Microsonde Electronique de Castaing	TF	Transformée de Fourier
EXAFS	Absorption de Rayons X Etendu aux Structures Fines	XANES	Absorption de Rayons X Etendu aux Structures Fines
FDR	Fonction de Distribution Radiale	XAS	Spectroscopie d'Absorption de Rayons X
MEB	Microscope Electronique à Balayage	XRD	Diffraction de Rayons X
MET	Microscope Electronique à Transmission	XRF	Fluorescence de Rayons X

1 Introduction

Le combustible nucléaire le plus couramment utilisé dans les réacteurs nucléaires commerciaux est constitué de dioxyde d'uranium faiblement enrichi (en ^{235}U fissile). La fission de l'^{235}U génère des fragments légers et lourds qui perturbent le réseau cristallin de la matrice du combustible. La performance globale du combustible est associée au rapport oxygène uranium (O/U) de la matrice avec un dioxyde d'uranium initial qui engendre la forme hyper-stœchiométrique UO_{2+x} avec x suivant l'oxydation associée au taux de combustion (également dénommé burn-up).

La performance du combustible standard UO_2 est essentiellement limitée par les phénomènes d'interaction pastille-gaine (IPG), de gonflement du combustible et par le relâchement des gaz de fission. Pour remédier à ces limitations, la tendance actuelle est de fabriquer des combustibles UO_2 avancés. Une stratégie appliquée en vue d'augmenter le taux de combustion consiste à diminuer la pression interne dans les crayons de combustible grâce à des pastilles d'UO_2 à gros grains. En effet dans ces combustibles, la cinétique de relâchement des gaz de fission (essentiellement Kr et Xe) diminue. Les études réalisées dans ce contexte montrent que l'une des options possibles pour augmenter la taille des grains des pastilles sans augmenter la température et le temps de frittage est l'addition de faibles quantités d'additifs. Par l'addition de certains dopants dans la poudre d'UO_2 (par exemple, TiO_2, Nb_2O_5, Cr_2O_3, V_2O_5) la taille des grains et le libre parcours moyen de diffusion sont augmentés, tandis que la surface totale de zone de joints de grains est réduite. En particulier, le dopage de l'UO_2 avec le Cr_2O_3 a été l'objet de nombreuses études depuis une vingtaine d'années; études qui se sont concrétisées par la commercialisation de produits combustibles.

D'autre part le combustible MOX contient des plutoniums fissiles (^{239}Pu et ^{241}Pu) issus du plutonium produit par l'irradiation de l'UO_2 faiblement enrichi en réacteur à eau légère (REL), retraité puis mélangé avec de l'UO_2 pour sa réutilisation en REL. Par conséquent, le combustible MOX est à base d'un mélange d'oxydes d'uranium et de plutonium. En effet, l'irradiation du plutonium comme constituant fissile dans le combustible MOX et l'immobilisation conjointe des produits de fission radioactifs se révèle être l'option actuelle de 'disposition' du plutonium excédentaire.

Alors qu'un travail expérimental important par analyse EPMA, MEB et/ou MET a été réalisé dans le passé en ce qui concerne l'étude des changements structurels dans les matrices de combustible UO_2 ou MOX, l'application de l'analyse de micro-faisceaux synchrotron (μ-XRD et μ-XAS) pour étudier l'UO_2 irradié a été très limitée. Un frein à l'utilisation de ces techniques est relatif aux réglementations dans l'usage de matériaux de haute activité dans la recherche utilisant les installations de rayons X synchrotron. En conséquence, des méthodes spécifiques ont été développées pour la préparation d'échantillons à partir de combustibles irradiés.

Cette thèse présente une analyse approfondie et comparative des résultats de mesures μ-XRD et μ-XAS de combustibles UO_2 standard, dopé au sesquioxyde de chrome (Cr_2O_3) et du MOX, irradiés ou non. Elle présente également l'interprétation des résultats en regard des effets induits par le chrome en tant que dopant ainsi que par la présence de plusieurs produits de fission.

Les paramètres de maille de l'UO_2 et les paramètres de densité d'énergie de déformation élastique dans les matériaux irradiés ou non ont été mesurés et quantifiés. Les données de μ-XRD ont en outre permis l'évaluation de la taille des domaines cristallins et la formation de sous-grains à différentes positions au sein des pastilles de combustibles irradiés. On a également cherché à déterminer le paramètre de maille et l'environnement atomique local du chrome dans des précipités d'oxyde de chrome présents dans les pastilles de combustible non-irradié. La structure locale du Cr dans la matrice du combustible dopé et l'influence de l'irradiation (pour le burnup considéré) sur l'état du chrome dans la matrice de combustible ont été étudiées. Enfin, pour une comparaison du comportement des gaz de fission et du phénomène de résolution induite par l'irradiation dans l'UO_2 standard ou dopé, la dernière partie de ce travail propose une tentative d'analyse de l'environnement atomique du Kr dans ces combustibles irradiés. Le travail effectué par micro-faisceau XAS sur ce gaz de fission concerne la détermination des distances du Kr avec ses proches voisins, une estimation des densités atomiques des gaz de fission dans les agrégats et des pressions internes apparentes dans ces nano-phases de gaz inertes.

2 Expérimental

Dans cette étude, les analyses des matériaux de combustibles ont été réalisées par microscopie électronique (MEB et EPMA) et différentes techniques de spectroscopie de rayons X (XRF, XRD et XAS) utilisant le rayonnement du synchrotron avec un faisceau focalisé au micromètre.

2.1 Matériaux

Les matériaux non-irradiés et irradiés de cette étude sont de l'UO_2 standard, de l'UO_2 dopé au sesquioxyde de chrome, tous deux de qualité commerciale, et du combustible MOX $(Pu,U)O_2$ à 4,7% en poids de PuO_2, D'autres détails sont présentés dans le Tableau 1.

Tableau 1: Caractéristiques des échantillons étudiés

Spécimen	Type de combustible	Taux de combustion (MW d kg^{-1})	Taille de grain (μm)	^{235}U (%)	Cr (μg g^{-1})
1	Standard non-irradié	0	10	4,9	< 5
2	Standard irradié	39.3	10	4,9[b]	< 5
3	Dopé non-irradié	0	48	4,8	1080
4	Dopé irradié	39.6	38[a]	4,8[b]	1080
5	MOX non-irradié	0	40	0,8	–
6	MOX irradié	60	30	0,8[b]	–

[a] Valeur indicative moyennée de la taille des grains mesurée au Laboratoire chaud du PSI selon la procédure ASTN-E-112, cette valeur ne représente pas la distribution de la taille des grains en fonction du rayon de la pastille.
[b] teneur initiale.

Le combustible dopé au sesquioxyde de chrome contient ~ 0,16 % en Cr_2O_3 (pour cent en poids) et a une taille de grains ~5 fois plus élevée que celle de l'UO_2 standard.
Le combustible $(U,Pu)O_2$ a été préparé par un procédé propre au Laboratoire chaud du PSI de gélification interne résultant en petites sphères de combustible. La taille de grain moyenne est de ~40 μm contrairement à celle du combustible commercial MOX MIMAS (mélange mère micronisé) irradié dans le monde entier (~10 μm).

Les matériaux combustibles ont été irradiés en centrales nucléaires suisses jusqu'au taux de combustion souhaité. Les mesures ont été effectuées sur des sous-échantillons préparés à partir de la région centrale (IC) et de la région de périphérie (IR) des pastilles irradiées.

2.2 Analyses par MEB et EPMA.

Les analyses MEB et EPMA ont été effectuées au moyen d'une unité blindée JEOL JXA-8500F à émission de champ et avec des spectromètres à longueur d'onde dispersive. L'analyse quantitative peut être faite avec un faisceau d'électrons à haute énergie de 0,1 µm de diamètre avec une résolution latérale de 1 µm.

Les mesures quantitatives par point ont été réalisées sur des particules et des précipités dans la matrice du combustible non-irradié ou irradié à plusieurs endroits. Les concentrations radiales qui ont été mesurées sont U, Cr, Al et O dans les combustibles non-irradiés et U, Cr, Al, Nd, Cs, Ba, Xe, Zr, Ru, Mo et O dans les spécimens irradiés.

2.3 Mesures par micro- XRF, XRD et XAS

Tous les travaux expérimentaux ont été effectués à la source de lumière suisse (SLS), l'installation du rayonnement synchrotron de l'Institut Paul Scherrer. La taille du faisceau de rayons X focalisé utilisé pour les mesures est comprise entre 1 et 4 μm^2. Les méthodes expérimentales utilisées sont la µ-XRF, la µ-XRD et la µ-XAS. Les éléments de la matrice analysés dans les combustibles étaient l'uranium, le chrome et le krypton.

3 Résultats et discussion

3.1 Etude du paramètre de maille des combustibles non-irradiés

La Figure 1 présente les résultats des paramètres de maille des deux combustibles d'UO_2 non-irradiés (échantillon 1 et 3).

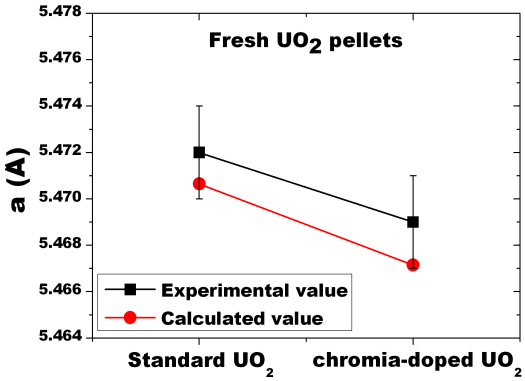

Figure 1: Comparaison des paramètres de maille expérimentaux des combustibles non-irradiés et de leurs valeurs calculées en utilisant l'équation empirique basée sur les rayons ioniques et la différence de charge entre le dopant (Cr^{3+}) et l'atome hôte (U^{4+}) dans la structure dans l'UO_2. Les données sont présentées en utilisant des symboles et les lignes continues sont ajoutées pour guider l'œil.

Les paramètres de maille sont respectivement de 5.472 et 5.469 Å pour le standard et le dopé. Ces résultats mettent en évidence une légère contraction du réseau fluorite cubique par ~ 3×10^{-3} Å dans le combustible dopé. Pour le combustible MOX vierge (échantillon 5) le paramètre de maille mesuré est 5.454 Å, valeur proche de celle attendue en raison de l'incorporation de Pu dans la maille d'UO_2.

3.2 Analyse de précipités d'oxyde de chrome dans UO_2 dopé non-irradié

Comme déjà mentionné dans le Tableau 1 la teneur en Cr dans le combustible dopé analysé était ~ 1080 µg/g (soit 0,160% en poids de Cr_2O_3). La formation de précipités de Cr_2O_3 n'a put être évitée en dépit de la température élevée et des conditions de frittage ajustées et appliquées dans le processus de production. Etant donné la relativement faible limite de solubilité de l'oxyde de chrome dans l'UO_2, il est reconnu que l'excès de Cr_2O_3 insoluble précipite toujours à partir de la solution solide pour créer des inclusions de phases secondaires dans la matrice d'UO_2. Une cartographie par EPMA est présentée sur la Figure 2. Caractérisé par imagerie aux rayons X le Cr, avec ses zones intenses (Fig. 2a), se révèle clairement être sous la forme de précipités. Nous avons analysé, en utilisant l'EPMA, dix gros précipités d'oxyde de chrome ($\geq$ 2 µm) répartis à différents endroits de l'échantillon. Dans tous les cas, la composition se révèle être proche de Cr_2O_3, avec une fraction d'Al_2O_3 provenant du lubrifiant utilisé lors de la fabrication.

Les particules d'oxyde de chrome dans l'échantillon de combustible dopé non-irradié ont également été mesurées par µ-XRD. La Figure 2b présente l'intégration 1-D de l'image de Laue (non représentée). A titre de comparaison, un spectre de diffraction des rayons X micro-faisceau d'un échantillon standard UO_2 est également inclus dans la Fig. 2b. L'encart dans la Figure 2b montre le profil de la ligne de Cr_2O_3 (110) du pic de diffraction. A partir du résidu, les signaux des échantillons standards et dopés en sesquioxyde de chrome sont extraits.

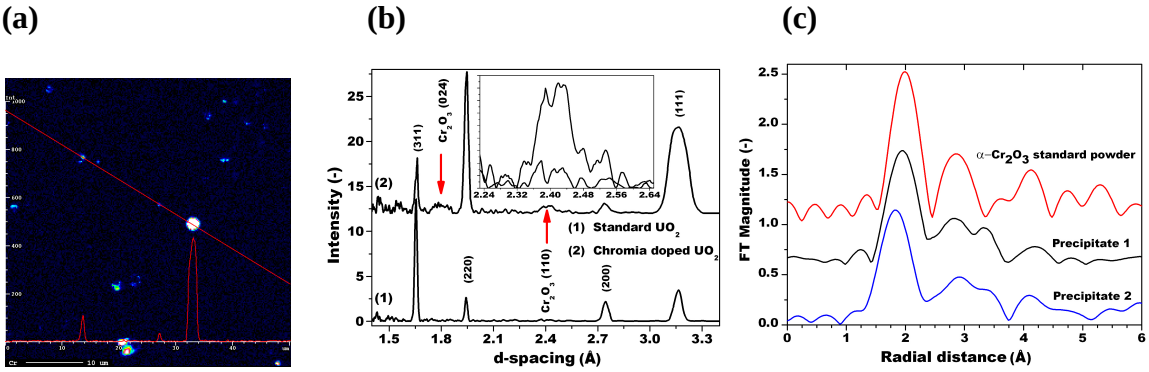

Figure 2: (a) Exemple d'une analyse du Cr d'un précipité par EPMA mesuré à partir de l'échantillon 3. (b) Intégration 1D de l'image diffraction (Laue) des rayons X montrant plusieurs lignes de diffraction pour l'UO_2 dopé. A titre de comparaison, un spectre µ-XRD de l'échantillon standard UO_2 est également inclus dans la figure. (c) Comparaison de la transformée de Fourier de l'EXAFS du seuil K du Cr pour la poudre de α-Cr_2O_3 (référence) et deux précipités de chrome analysés dans l'échantillon de combustible dopé.

Tous les pics intenses des échantillons d'UO_2 standard et dopé peuvent être attribués à une structure fluorite cubique (groupe spatial $Fm\bar{3}m$, no. 225) de dioxyde d'uranium. Cependant, deux pics faible intensité (repérés par des flèches à 1,8 et 2,4 Å le long de l'axe x sur la Figure 2b) sont observés pour l'échantillon dopé au sesquioxyde de chrome; ces pics ne sont pas détectés sur l'UO_2 standard. Ils ne correspondent pas à des pics mineurs d'UO_2; ils correspondent cependant à la phase de sesquioxyde de chrome. Cette supposition est tout à fait raisonnable puisque les précipités de Cr sont également observés par EPMA sur cet échantillon.

La structure cristalline de Cr_2O_3 est de type de corindon (groupe d'espace $R\bar{3}c$, no. 167) et la cellule unitaire hexagonale compacte à température ambiante est donnée par c_H/a_H = 2,740. Ici, c_H désigne la hauteur de la cellule et a_H représente la longueur des côtés de base. Les résultats montrent que ces pics sont en effet originaires de phases polycristallines de Cr_2O_3, présentant des lignes de diffraction bien résolues: (024) et (110) correspondant aux distances interplanaires (d) de 1,79 et 2,42 Å, respectivement, déterminées avec une précision de ±0,01 Å. En utilisant la relation pour la structure hexagonale, les paramètres de réseau des particules de sesquioxyde de chrome sont estimés à: a_H = 4,84 Å et c_H = 13,72 Å. Ces valeurs semblent être quelque peu différentes par rapport à celles reportées dans la littérature pour α-Cr_2O_3 qui sont de a_H = 4,95 Å et c_H = 13,58 Å pour la cellule standard. La légère différence entre les valeurs peut être

attribuée au niveau de cristallisation des précipités dans le cristal d'UO_2. Il convient également de mentionner que la largeur des deux lignes (024) et (110) des particules de Cr_2O_3 dans le combustible est supérieure à celles ayant été mesurées à partir de l'échantillon de haute pureté de la poudre Cr_2O_3 de référence. Puisque cette largeur élevée est la signature en μ-XRD de précipités fins de Cr_2O_3 dans un état imparfait, on peut conclure sur la présence de défauts dans les précipités de Cr_2O_3 dans l'échantillon étudié.
L'environnement atomique local du Cr a également été analysé dans ces particules de phases secondaires en utilisant la technique micro-XAS. Dans la Figure 2c, les transformées de Fourier (TF) de l'EXAFS au K-seuil du Cr enregistrée pour la poudre α-Cr_2O_3 de référence et de précipités d'oxyde de chrome analysés dans l'échantillon de combustible UO_2 dopé, sont présentées. En ce qui concerne l'environnement atomique du Cr, on observe que qualitativement il n'y a pas de différence majeure d'un précipité à l'autre, mais qu'ils diffèrent tous distinctement de la phase de α-Cr_2O_3 pure. Les TF des signaux EXAFS du Cr présentent clairement des différences à bien des égards, ce qui suggère qu'il a des changements structurels notables dans la sphère de coordination du Cr. Les précipités formés dans l'UO_2, présentent des différences quantifiables de longueur de liaison Cr-O et Cr—Cr, de nombre de coordination et de fonction de distribution radiale en comparaison des valeurs de l'α-Cr_2O_3. Dans les précipités de Cr_2O_3, l'analyse EXAFS a révélé que les deux premières couches de coordination Cr-O sont remplies avec environ 4 voisins d'oxygène à une distance moyenne de 1,90 ± 0,02 Å, ce qui correspond au sesquioxyde de chrome. Cela diffère de la configuration de la liaison Cr dans le Cr_2O_3 standard et cristallin (six atomes d'oxygène en symétrie octaédrique à une distance moyenne de 1,99 Å). En ce qui concerne la corrélation métal-métal, la plus courte distance Cr-Cr de 2,72 Å, mesurée à partir de particules de chrome, est notamment plus longue que la distance Cr-Cr de 2,64 Å déterminée pour le α-Cr_2O_3 standard. Une explication possible, pour tenir compte de toutes ces observations, est que la taille apparente de ces cristallites de Cr_2O_3, s'accroit lors du refroidissement pour créer des inclusions de phases secondaires et se présentent comme des précipités dans les pastilles d'UO_2 dopé au sesquioxyde de chrome. Les valeurs de σ^2 (facteur de Debye-Waller) de toutes les paires atomiques sont sensiblement plus élevées par rapport à celles de l'α-Cr_2O_3, ce qui implique un désordre structurel et des distorsions dans les précipités

d'oxyde de chrome, comme également suggéré par l'analyse μ-XRD. Ces résultats peuvent être expliqués comme étant en partie dus à l'effet de la taille des particules Cr_2O_3, probablement avec des tailles de cristallites nanoscopiques, nucléées par le refroidissement de la solution solide en excès et créant, par inclusion, des phases de sesquioxyde de chrome dans le combustible UO_2 dopé.

3.3 Etude des paramètres de réseau des combustibles irradiés

D'une manière similaire aux lignes de diffraction des pastilles de UO_2 non-irradiées, les lignes de diffraction mesurées pour les combustibles irradiés sont analysées en détail. Les échantillons examinés sont l'échantillon 2 (IC et IR), l'échantillon 4 (IC et IR) et l'échantillon 6 (IC et IR). Les valeurs expérimentales et calculées du paramètre de maille sont présentées dans le Tableau 2 et représentées graphiquement dans la Figure 3.

Tableau 2: Paramètres de réseau cristallin expérimentaux et calculés pour les échantillons de combustibles dopés ou non à l'oxyde de chrome (non-irradié et irradié) et MOX. Les valeurs de calcul pour le combustible irradié sont à considérer avec précaution compte tenu des effets du Cs, Xe, Rb et Kr.

Spécimens/région		**Paramètre cristallin**	
		Valeur expérimentale ($\pm 2.0\times10^{-3}$) (Å)	**Valeur calculée (Å)**
UOx standard	non- irradié	5,472	5,47065
	irradié centre	5,482	5.47449
	irradié rim	5,483	5.47567
UOx dopé	non-irradié	5,469	5,46715
	irradié centre	5,482	5,47099
	irradié rim	5,485	5,47217
MOX	non-irradié	5,454	5,468
	irradié centre	5,487	5,469
	irradié rim	5,456	5,468

Sous irradiation, la constante de réseau moyenne du combustible standard UO_2, augmente jusqu'à 5.483 Å ce qui est très proche de la constante de réseau de l'échantillon dopé irradié: 5.485 Å avec une précision de ~ 0,03%. Par rapport à la valeur de UO_2 non irradié, la différence des paramètres de réseau est significative et environ égale à 12×10^{-3} Å (~0,22% de la valeur moyenne) pour les deux combustibles dopé ou non-dopé irradiés. Les modifications structurelles du réseau et le changement de paramètre de maille dans ces deux matériaux (UO_2 dopé et non-dopé) sont similaires. Les différences observées

dans les paramètres de maille sont associées, à l'échelle atomique, aux modifications de structure d'UO_2 causées par les effets d'irradiation.

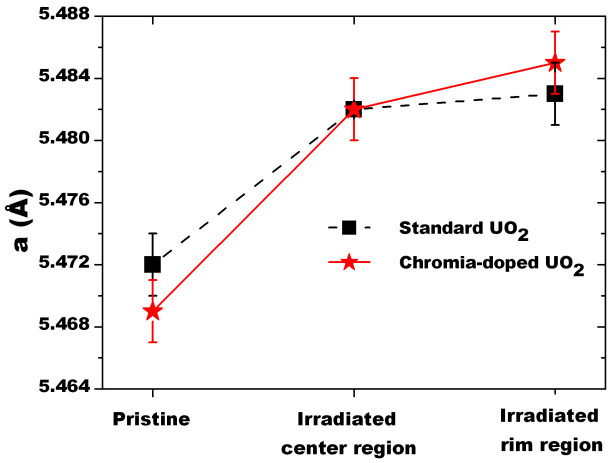

Figure 3: Paramètres de maille des combustibles non-irradiés et irradiés en fonction du taux de combustion qui augmente de gauche à droite; les lignes reliant les points de données sont ajoutées pour guider l'oeil.

Sous irradiation, ces combustibles ont subi un certain nombre de changements de micro-structure et de composition en fonction du taux de combustion local et de la température dans le combustible. Ici nous nous sommes intéressés principalement aux changements les plus susceptibles d'influencer les structures du réseau. Dans l'analyse, nous avons considéré principalement les substitutions de cations isovalents et aliovalents des produits de fission en solution solide avec les cations U^{4+} dans la matrice hôte d'UO_2.

L'analyse montre que les écarts maxima entre la constante de réseau de l'UO_2 non-irradié et irradié, respectivement, pour le centre et les régions de la périphérie de la pastille de combustible, sont seulement de $3,5 \times 10^{-3}$ Å et $4,7 \times 10^{-3}$ Å (sans Kr + Xe), et, de ~ $3,8 \times 10^{-3}$ Å et ~ 5.0×10^{-3} Å (avec Kr + Xe) pour le combustible dopé. Ces dernières valeurs sont estimées d'une manière conservative, compte tenu de petites quantités solubles de Xe (*r*: 2.2 Å) et de Kr (*r*: 2,0 Å), par exemple 0,01 % en poids. Tous ces résultats indiquent que des quantités importantes de produits de fission peuvent être accommodées sans modification importante du réseau. Cependant, le changement prévu de maille du réseau UO_2 dans les combustibles irradiés en raison de la présence successives de produits de fission solubles est faible (de l'ordre de $1\text{-}3x10^{-3}$ Å jusqu'à 5×10^{-3} Å d'une manière conservatrice), et ne peut être utilisé seule pour expliquer l'accroissement de la constante de réseau de 12×10^{-3} Å mesurée. En fait, de fortes concentrations de défauts ponctuels et

de défauts étendus dus aux gaz de fission coexistent dans UO_2 à haut taux de combustion, ce qui augmente ainsi le réseau cristallin comme observé.

Le paramètre de maille du combustible MOX non-irradié est sensiblement plus petit que celui calculé et mesuré pour le combustible UOx, ceci étant dû au rayon de Pu^{4+}, plus petit que U^{4+}. Les variations du paramètre avec la position dans le combustible irradié sont repris dans le Tableau 2.

3.4 Tension critique et polygonisation du combustible dans l'UO_2 irradié standard et dopé

Comme la μ-XRD permet d'examiner des zones de taille microscopique, elle est des plus appropriée pour l'analyse des tensions uniformes et non-uniformes de grains spécifiques dans le combustible irradié. La Figure 4 (a&b) montre les résultats de l'analyse de la tension des combustibles irradiés standard ou dopé au sesquioxyde de chrome.

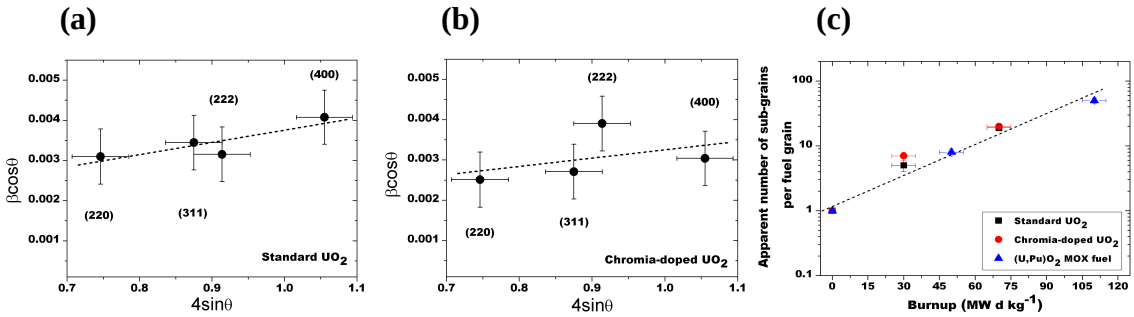

Figure 4: Graphique de Williamson-Hall pour déterminer la valeur ε_{nu} dans les grains de combustibles irradiés pour: (a) UO_2 standard, (b) UO_2 dopé. (c) nombre apparent de sous-grains par grains de combustible en fonction du taux de combustion pour les combustibles irradiés. La ligne en pointillé est ajoutée pour guider l'oeil.

La pente de la courbe dans la Fig. 4b donne la micro-dilatation $\varepsilon_{nu} = 2{,}1\times10^{-3}$ pour l'échantillon dopé. La dilatation uniforme du cristal ε_c se trouve être d'environ $3{,}0 \times 10^{-3}$. Celle-ci peut à son tour entraîner une énergie de déformation accumulée d'U = 6,4 MJ m^{-3} pour le combustible dopé. Suite à une analyse similaire pour UO_2 standard (échantillon 2, IC), on obtient environ une valeur de U = 7,1 MJ m^{-3}. Ces grandeurs de tension sont déjà au-delà de la limite de polygonisation du combustible et la formation de sous-grains dans les combustibles irradiés en est la conséquence. Ainsi, le nombre apparent moyen de sous-grains par grain de combustible a été évalué. Ces résultats sont représentés graphiquement dans la Figure 4c. Les résultats montrent une tendance générale: la

polygonisation augmente avec le taux de combustion local. Alors que la polygonisation n'est pas observée dans le combustible non-irradié, elle devient d'autant plus forte que le taux de combustion local augmente. Cependant, un autre facteur important est la température du combustible. Une température élevée, au centre du combustible, peut être responsable d'un effet de 'cicatrisation' qui répare la structure cristalline. Lorsque la tension est suffisamment grande, les grains font l'objet de polygonisation avec des dislocations aléatoires pour réorganiser le grain en réduisant l'énergie de déformation.

3.5 Environnement atomique du Cr en UOx dopé irradié et non-irradié.

Avant de discuter des résultats quantitatifs d'EXAFS, il est opportun de mentionner quelques points pertinents en vue de l'analyse des données. Comme la structure de l'UO_2 dopé au Cr ne peut être obtenue directement à partir d'un spectre XAS mesuré, des structures modèles doivent être présumées. La fonction de distribution radiale (FDR) simulée correspondant au spectre doit être calculée avec détermination des modèles qui s'adaptent pour le mieux aux données. Dans ce qui suit, nous décrivons d'abord les résultats EXAFS expérimentaux sur le seuil L_3 de l'uranium. Elle est suivie par une comparaison entre les échantillons non-irradiés et irradiés des résultats expérimentaux enregistrés pour le seuil K du Cr, et l'analyse FEFF considérant un comportement de substitution cationique de chrome dans l'UO_2. L'objectif était d'évaluer le nombre et la nature des voisins les plus proches du Cr nécessaires pour reproduire au moins la forme générale du spectre FDR expérimental au seuil K du Cr. Pour le modèle de substitution de l'uranium par le chrome, l'utilisation du seuil L_3 de l'U permet l'analyse FEFF plus simple pour le seuil K du Cr. Cette analyse a fourni la plupart des paramètres pour les cartes de contrôle nécessaires dans le fichier d'entrée de FEFF pour générer pour la structure cristalline du dioxyde d'uranium les estimations quantitatives du seuil K du Cr.

3.5.1 EXAFS de l'uranium au seuil L_3

La Figure 5 présente le spectre EXAFS du seuil L_3 de l'uranium mesuré à partir de l'UO_2 irradié et sa simulation en utilisant le programme FEFF. La première dérivé du spectre, utilisée pour évaluer la position de l'énergie du seuil, révèle une valeur E_0 de 17170±1 eV, elle est conforme aux données publiées pour l'état d'oxydation 4+ de l'U.

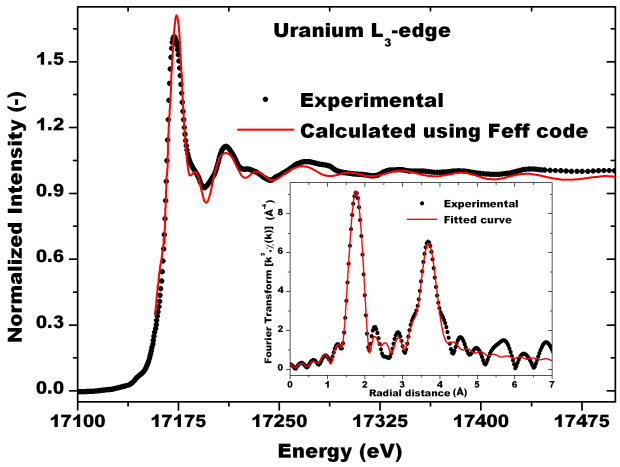

Figure 5: Spectre d'absorption du seuil L_3 de l'uranium mesuré à partir de l'UO_2 irradié corrigé du bruit de fond normalisée. Le spectre est calculé avec FEFF sur la base des paramètres structuraux dérivés de spectres EXAFS adaptés. Dans le médaillon, les modules des fonctions TF-EXAFS pondérées en k^3 sont présentés (non corrigées du déphasage). Les spectres tracés en pointillé et les courbes pleines sont respectivement expérimentaux et modélisés. La fenêtre de calcul est comprise entre 1,2 et 5,2 Å.

Pour une analyse quantitative de l'EXAFS expérimental, la procédure d'ajustement a été adoptée. Le FDR résultante est présentée en encart sur la Figure 5. Une bonne corrélation peut être observée entre les spectres expérimentaux et calculés. Les analyses FEFF s'adaptent aux TF- EXAFS. Elles révèlent la présence de rétrodiffusion pour des distances U-O de 2,36 ± 0,03 Å, U – U de 3,83 ± 0,02 Å et U – O de 4,41 ± 0,03 Å correspondant aux trois premiers trajets de diffusion simple. Les nombres de voisin de l'U absorbeur sont d'environ 8, 11 et 24 avec des facteurs de DW de $(4 \pm 1)\times10^{-3}$, $(6 \pm 2)\times10^{-3}$ et $(13 \pm 2)\times10^{-3}$ $Å^{-2}$ respectivement, pour ces couches. Il ressort de nos résultats que la faible teneur en chrome dans les grains d'UO_2 dopé ne produit pas de signal EXAFS pour les paires U – Cr, l'uranium étant l'atome absorbeur, en raison de très faibles activités de rétrodiffusion à partir d'atomes dopants. Au contraire, l'étude EXAFS au seuil du chrome de l'UO_2 dopé est en mesure de fournir la signature de la couche de la coordination Cr - U comme discuté dans la section suivante.

3.5.2 EXAFS du Cr au seuil K

Les données expérimentales des seuils d'absorption K du Cr, et les fonctions $\chi(k)$ et FDR extraites des oscillations EXAFS de combustibles non-irradiés et irradiés sont présentées sur la Figure 6. Le profil et la position des seuils, XANES, l'EXAFS et les courbes d'amplitude TF sont similaires pour les deux échantillons examinés. Ces résultats

démontrent que l'environnement du chrome est analogue dans les deux échantillons et qu'aucun changement majeur n'a lieu dans la structure locale du Cr lors de l'irradiation, du moins pour un taux de combustion moyen des pastilles de combustible de ~40 MW d kg^{-1}.

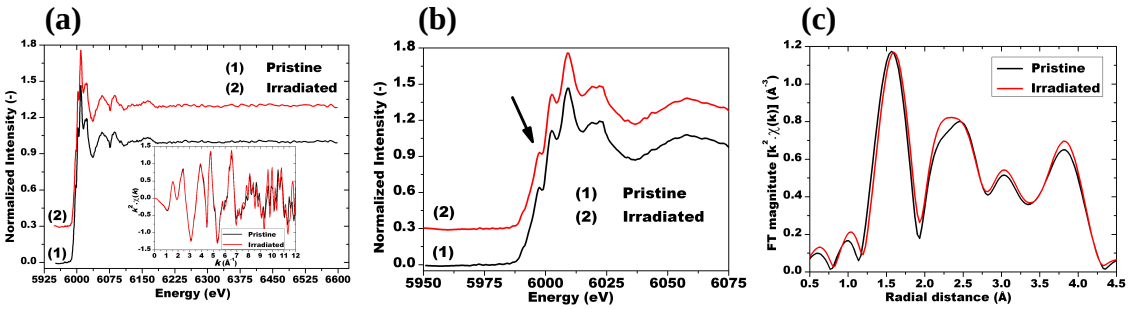

Figure 6: (a) Spectres d'absorption des rayons X, corrigés du bruit de fond et normalisés, enregistrés au seuil K du Cr pour des combustibles UO_2 dopé non-irradiés et irradiés. Les spectres sont décalés verticalement pour plus de clarté. L'encart montre les oscillations EXAFS pondérées en k^2 en chevauchement pour les deux échantillons. (b) Le zoom de la partie XANES est comparé pour les deux échantillons. Le pré-pic discuté dans le texte est marqué par une flèche. (c) Résultats de TF-EXAFS (sans correction de déphasage) effectués dans la région de vecteur d'onde 2,0 – 9,5 $Å^{-1}$.

L'énergie du seuil d'absorption du Cr est de E_0 = 6000,5 ± 1,0 eV dans les échantillons. Ce spectre indique que l'état apparent d'oxydation du Cr dans l'UO_2 dopé est 3+. Cependant, un épaulement à 5996 eV (maximum) est à noter dans la région XANES (Fig. 6b, marqué par une flèche). L'origine de cette structure supplémentaire est encore inconnue. Sur la base de la littérature elle pourrait être attribuée à du Cr^{2+}, cependant la transition de symétrie 1s → 4s est interdite. Dans la suite, une analyse EXAFS du seuil K de Cr pour les environnements locaux du chrome dans la matrice UO_2 est discutée.

Les courbes d'amplitude TF présentée sur la Figure 6c montrent qu'il existe plusieurs couches de coordination des voisins du chrome. Toutefois, les contributions des couches individuelles autour du Cr ne sont pas faciles à résoudre à l'exception de la première (Fig. 6c). Pour l'affectation des différents voisins du Cr, la fonction de distribution radiale pour l'échantillon d'UO_2 dopé non-irradié a été analysée. Les enveloppes d'amplitude théoriques et des fonctions de phase ont été obtenues par des simulations FEFF basées sur le modèle de structure de l'UO_2 de référence substitué au Cr, comme indiqué précédemment. L'affectation de caractères distincts sur la TF à 2,4 Å (voir Fig. 6c) exige une contribution Cr - Cr ce qui ne peut être négligée dans l'ajustement de la courbe a priori. Nous n'avons pas d'explication simple pour ce faible signal du Cr dans les données

de TF du Cr analysées. Nous émettons l'hypothèse qu'il reflète les contributions de quelques nanoparticules de Cr_2O_3 non dissoutes dans l'UO_2 dopé comme déjà confirmé par la cartographie EPMA du combustible non-irradié (voir les sections précédentes). Dans cette perspective, des combinaisons linéaires ont été testées sur les TF des spectres EXAFS du Cr, en utilisant les chemins de diffusion calculés par FEFF pour l'UO_2 substitué au Cr et pour la référence de α-Cr_2O_3. Les distances moyennes Cr–O et Cr – U déterminées dans UO_2 dopé sont 2,02 ± 0,03 Å et 3,75 ± 0,04 Å, respectivement, avec pour nombre de voisins 6,0 ± 0,5 et 11,0 ± 1,0. Ce résultat signifie que des distorsions locales de réseau s'installent autour du Cr dues aux grandes variations de longueur de la liaison allant de 0,1 à 0,3 Å en fonction de la proximité du Cr avec les atomes d'oxygène et d'uranium à des distances inférieures à celles prévues. Il faut noter que les valeurs idéales des plus proches distances cristallographiques U–O et U – U dans le dioxyde d'uranium sont respectivement de 2,36 et 3,86 Å. La diminution de la coordination ainsi que des distances Cr–O et Cr – U dans l'UO_2 dopé peuvent être expliquées par les effets de compensation de charge résultant de l'incorporation de Cr^{3+} sur les sites d'U^{4+} et par la différence de taille des cations.

Un procédé de filtrage de Fourier a également été appliqué pour analyser la première couche d'oxygène, le voisin le plus proche du Cr, dans la matrice d' UO_2 non irradiée et irradiée afin de déterminer la moyenne des longueurs de liaison et les nombres de coordination autour des atomes de chrome. Les résultats montrent que le Cr dissous dans UO_2 non-irradié est entouré par 6,2 ± 0,5 atomes d'oxygène à une distance moyenne de 2,02 ± 0,02 Å ce qui est proche du nombre de coordination du Cr: 6,0 ± 0,5 et de la longueur moyenne de liaison Cr–O : 2,05 ± 0,02 Å dans le UO_2 dopé irradié. Ces résultats sont la preuve expérimentale directe que l'incorporation du Cr^{3+} dans les sites d'U^{4+} perturbe à la fois les systèmes cation-anion et cation-cation dans le réseau d'UO_2 et que nos résultats fournissent des informations à l'échelle atomique quantitative de ces processus. Il semble que pour 0,160 % en poids d'oxyde de chrome dans UO_2, le désordre atomique autour du Cr généré par le dopage est important, comme en témoigne la réduction du nombre de coordination et la distance interatomique entre Cr et les atomes d'oxygène les plus proches. Ce désordre atomique n'est pas modifié par l'irradiation (pour le taux de combustion étudié ici).

3.6 Résultats d'analyse du krypton.

Les spectres d'absorption du krypton ont été enregistrés pour les deux échantillons irradiés: UO_2 et UO_2 dopé. Les transformées de Fourier des signaux EXAFS ont révélé les positions des atomes voisins les plus proches: ~3,66 Å (UO_2) et ~3,59 Å (UO_2 dopé). L'analyse de la densité de Kr pour la structure cubique à faces centrées est fondée sur la présence de Xe seulement autour du Kr. Le rapport atomique Xe/Kr, correspondant à celui déduit de la littérature pour le taux de combustion des combustibles étudiés, est de ~10. Pour cette structure et les distances Kr–Xe mesurées, les densités atomiques de ~28.8 and ~30.6 atomes nm^{-3} sont respectivement déduites.

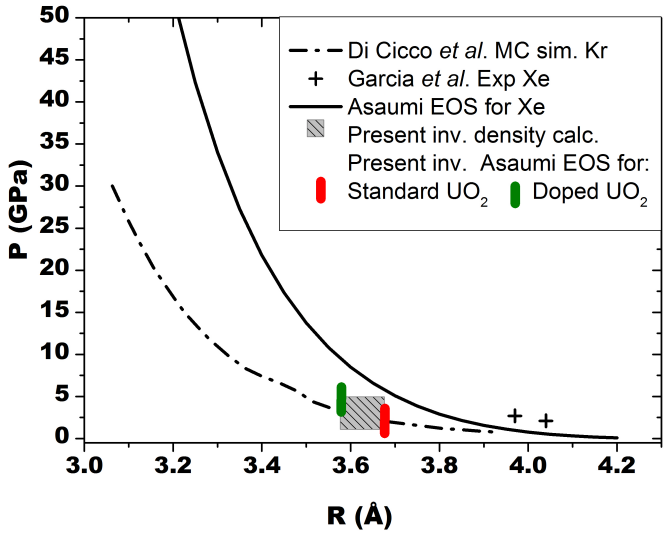

Figure 7: Pression apparente en fonction de la distance entre atomes de gaz inertes.

Sur la base d'études précédentes rapportées dans la littérature portant sur le Xe et le Kr, et les estimations des densités en nombre d'atomes par unité de volume des combustibles UO_2 et UO_2 dopé irradiés, les pressions internes des gaz peuvent être comparées avec les résultats des calculs de pression internes obtenus en utilisant l'équation d'état de type Birch-Murnaghan. Ce résultat peut être expliqué comme une conséquence de la plus grande quantité d'atomes de Xe et de Kr retenus dans le combustible dopé par rapport au combustible standard. Les résultats obtenus sont également présentés et comparés (sur la Figure 7) avec les calculs théoriques de la littérature pour des cristaux de Xe et de Kr purs et avec des données expérimentales d'échantillons UO_2 implantés au xénon. Les résultats

indiqueraient une densité de gaz rare légèrement plus élevée (ainsi que de la pression) dans le cas du combustible dopé.

Il ne serait pas exact de dire que la pression mesurée provient exclusivement de bulles de tailles micrométriques que l'on détecte par EPMA (limite de résolution). En raison de la préparation de l'échantillon et de la taille des particules analysées de l'ordre de 10 μm, une partie des gaz de fission a été libérée. Les phases analysées sont celles d'agrégats et de nano-bulles intactes restées dans les échantillons ultra-minces après préparation. Le signal XAFS mesuré implique la proximité des atomes de Kr et de Xe. S'ils ne sont pas dans des bulles de plusieurs μm de taille, ils doivent être soit quasi dissouts dans la masse (mais le voisin détecté est le Xe) soit en agrégats de taille nanoscopique à haute densité et pression.

4 Conclusions

Cette thèse se focalise sur l'étude des modifications structurelles à l'échelle nanoscopique et atomique de matériaux de combustible nucléaire avant et après irradiation. L'étude expérimentale a été réalisée pour un ensemble de combustibles UO_2 standard, UO_2 dopé au Cr_2O_3 et de combustible MOX $(U,Pu)O_2$ non irradiés et irradiés dans des réacteurs nucléaires en Suisse. L'un des principaux objectifs de ce travail était d'étudier l'environnement à l'échelle atomique du chrome comme dopant dans des pastilles de combustible UO_2 dopé au chrome non-irradié et l'influence de l'irradiation sur le chrome dans les combustibles irradiés. Sur la base de la bibliographie, il est apparu que le mécanisme de base de l'incorporation du chrome dans le réseau UO_2 reste encore difficile à cerner malgré les nombreux travaux déjà réalisés. D'autre part la structure à l'échelle atomique du chrome n'est pas connue dans les combustibles irradiés dopés au sesquioxyde de chrome. Beaucoup de questions demeurent quant à la nature et la configuration des défauts de structure formés lors de l'irradiation des combustibles dopés au chrome et le rôle du chrome sur l'évolution structurelle du combustible ainsi que sur la nucléation et la croissance des phases de gaz de fission ; questions qui sont essentielles vis à vis de l'évaluation des performances du combustible dopé en service. La compréhension de ces phénomènes passe par l'analyse du développement structurel à l'échelle atomique dans les combustibles sous irradiation. Pour cette raison, une série

d'analyses par micro-sonde à rayons X synchrotron et la modélisation des données expérimentales ont été effectuées. Les principaux résultats et leur interprétation sont résumés ci-dessous**:**

- L'évolution du paramètre de maille UO_2 a été analysée pour tous les échantillons de combustibles irradiés et non-irradiés. Les valeurs des paramètres de maille mesurées ont été comparées avec celles prédites par la théorie. Dans l'analyse des données, le rôle du Cr en tant que dopant et l'impact de plusieurs produits de fission résultant des effets d'irradiation ont été examinés. Les tendances observées sont que, dans l'UO_2 non-irradiée le paramètre de réseau diminue légèrement en raison du dopage au Cr_2O_3, il augmente cependant dans les matériaux irradiés. Tous les échantillons irradiés se comportent d'une manière similaire (pour les taux de combustion étudiés) avec l'expansion du réseau d'UO_2 survenant lors de l'irradiation, où aucun effet induit par le Cr ne semble significatif, alors que les défauts induits par irradiation prévalent.
- Les densités d'énergie de déformation élastiques dans les combustibles irradiés ont été évaluées sur la base de la déformation du réseau cristallin de UO_2 et de la tension non-uniforme. L'origine de la tension est considérée comme étant la même pour les échantillons non dopé et dopé, ainsi que les défauts des cristallites d'UO_2 irradiées, dont les plus importants sont les dislocations. La déformation du réseau pour l'UO_2 dopé au sesquioxyde de chrome est d'environ 0,4%, ce qui n'est pas très différent du résultat correspondant aux échantillons de UO_2 non-irradié. Ce résultat confirme que le dopage à l'oxyde de chrome n'a pas d'effet néfaste vis-à-vis de ce paramètre. Le comportement de la structure de l'UO_2 standard et de l'UO_2 dopé est assez similaire pour un taux de combustion moyen de 40 MW d kg^{-1}.
- L'amplitude des déformations mesurées dans tous les échantillons irradiés s'inscrit déjà dans un régime de polygonisation des combustibles. En conséquence, la subdivision des grains d'UO_2 a été clairement mise en évidence dans les expériences et quantifiée. La polygonisation du combustible a été observée et dépend du taux de combustion local. Pour les combustibles non-irradiés, la polygonisation n'a évidemment pas été détectée. Au centre des pastilles irradiées, une certaine polygonisation a été détectée localement. L'effet le plus prononcé se

situe à la périphérie des pastilles irradiées. Une détermination quantitative du nombre apparent de sous-grains par grain d'UO_2 a été possible durant le travail de thèse. Aucune différence significative n'a été trouvée entre le combustible dopé et non-dopé.

● La présence de précipités de chrome non solubilisé a été mise en évidence par EPMA dans les pastilles non irradiées et facilement détectés par micro-faisceau de lumière synchrotron. La composition de ces particules déterminée par EPMA s'avère être très proche de Cr_2O_3. Les résultats XAS ont montré que l'état d'oxydation du Cr dans les précipités est Cr^{3+}. D'après les résultats de la diffraction des rayons X, les précipités Cr_2O_3 dans l'UO_2 sont l'objet de désordres structurels et ont une structure en réseau déformée par rapport à celle du cristal hexagonal Cr_2O_3 de référence. Le détail des résultats d'analyse de micro-EXAFS montre que la longueur de la liaison des deux premières couches de Cr-O se trouvant sur le plan *a b* de sa cellule du cristal hexagonal est raccourcie pour l'oxyde de chrome précipité tandis que celle de la première paire Cr - Cr situé le long de l'axe *c* est légèrement allongée.

● La structure atomique locale du chrome dans les grains d'UO_2 dopé a également été analysée. Le chrome a un état d'oxydation Cr^{3+} dans les grains d'UO_2 à l'état irradié et non irradié. Les expériences EXAFS ont clairement démontré que la structure locale autour du chrome est analogue dans le UO_2 dopé non-irradié et irradié et qu'aucun changement majeur n'a lieu sur l'état du Cr durant l'irradiation, au moins jusqu'à un taux de combustion moyen de ~ 40 MW d kg^{-1}. Cette information s'avère de nature précieuse en ce qui concerne la performance du combustible pour des burn-up plus élevés qu'examinés ici et aussi pour le comportement du combustible dopé en service. Les données XAS expérimentales ont été analysées en détail en supposant une substitution uranium-chrome. Une réduction importante dans la longueur de liaison adjacente Cr-O d'environ 0,3 Å dans l'UO_2 dopé non-irradié par rapport à la longueur de liaison idéale U-O dans UO_2 serait attendue en raison de la variation des interactions coulombiennes effectives résultant du remplacement de U^{4+} par Cr^{3+} et de la différence de taille des cations. La contraction de la plus courte distance Cr - U est de ~0,1 Å par rapport à

la distance U-U dans le volume d'UO_2. Il est établi dans le présent travail que l'incorporation de Cr dans l'UO_2 perturbe à la fois les systèmes cation-anion et cation-cation dans le réseau d'UO_2. Ces résultats fournissent des informations quantitatives à l'échelle atomique de ces processus.

- Les données d'absorption de rayons X du krypton dans le dioxyde d'uranium des combustibles irradiés standard et dopé ont été enregistrées avec succès. Les distances des plus proches voisins du Kr obtenues par transformée de Fourier des spectres EXAFS aux seuils K du Kr des deux échantillons ont été utilisées pour calculer la densité d'atomes par unité de cellule et les pressions internes correspondantes. Les résultats obtenus pour le combustible dopé montrent que la densité et la pression interne correspondante sont plus importantes que celles du combustible standard, ce qui peut suggérer une rétention plus forte des gaz de fission dans le combustible dopé.

Afin d'affiner les résultats et la qualité des échantillons, des améliorations sont nécessaires. Les suggestions et recommandations dans ce cadre ainsi que pour la poursuite des travaux d'expérimentation sont: l'utilisation d'une unité de faisceau d'ion focalisé (FIB) pour la préparation de micro échantillons, l'optimisation de la géométrie et de la détection sur la ligne de micro-XAS et l'analyse d'échantillons pour des taux de combustion plus élevés pour élargir le champ d'étude de ce travail.